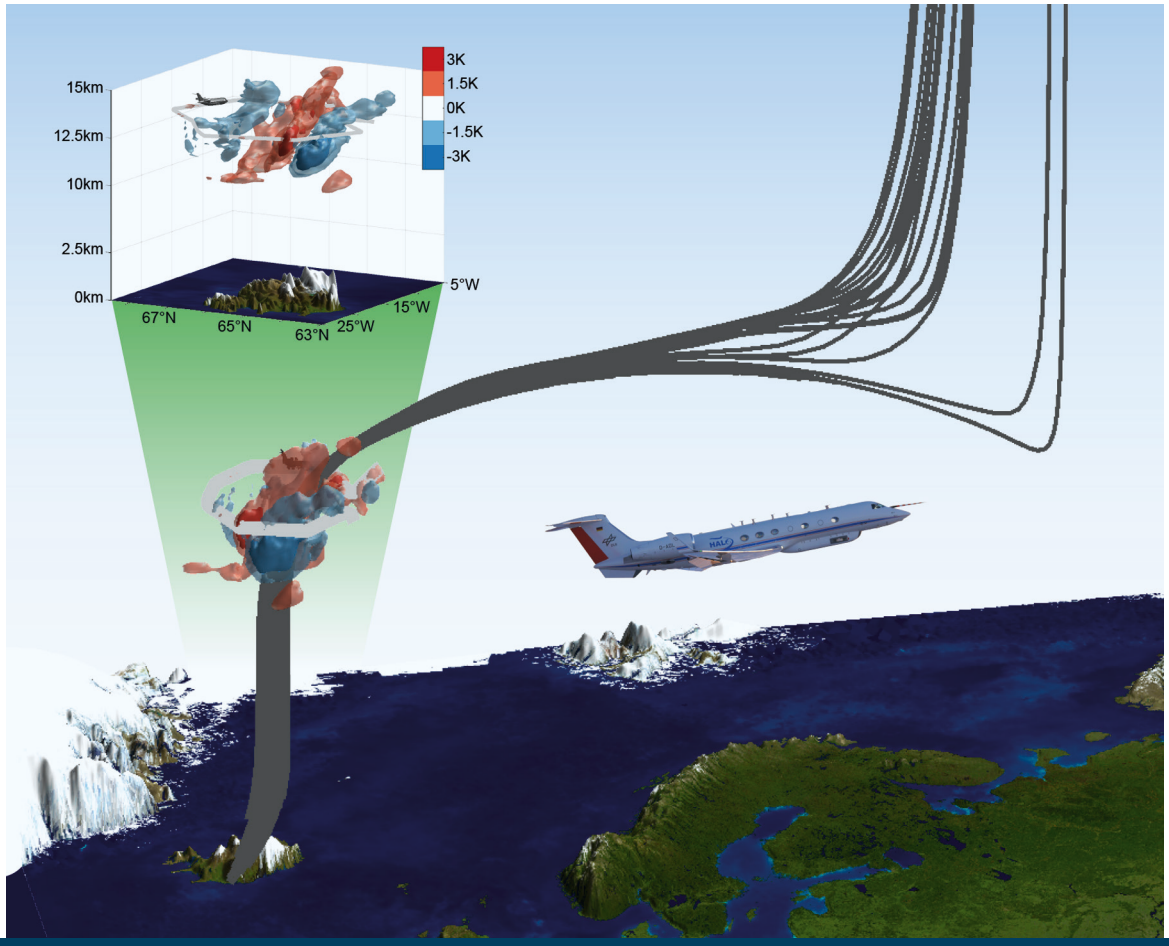

Tomographic observations of gravity waves with the infrared limb imager GLORIA

Isabell Krisch

Energie & Umwelt / Energy & Environment
Band / Volume 496
ISBN 978-3-95806-481-2

Mitglied der Helmholtz-Gemeinschaft

JÜLICH
Forschungszentrum

Schriften des Forschungszentrums Jülich
Reihe Energie & Umwelt / Energy & Environment Band / Volume 496

The PhD thesis can be quoted as follows:

urn:nbn:de:hbz:468-20200813-094534-0
[http://nbn-resolving.de/urn/resolver.pl?urn=urn%3Anbn%3Ade%3Ahbz%3A468-20200813-094534-0]

DOI: 10.25926/m5ht-7915
[https://doi.org/10.25926/m5ht-7915]

Forschungszentrum Jülich GmbH
Institut für Energie- und Klimaforschung
Stratosphäre (IEK-7)

Tomographic observations of gravity waves with the infrared limb imager GLORIA

Isabell Krisch

Schriften des Forschungszentrums Jülich
Reihe Energie & Umwelt / Energy & Environment Band / Volume 496

ISSN 1866-1793 ISBN 978-3-95806-481-2

Bibliografische Information der Deutschen Nationalbibliothek.
Die Deutsche Nationalbibliothek verzeichnet diese Publikation in der
Deutschen Nationalbibliografie; detaillierte Bibliografische Daten
sind im Internet über http://dnb.d-nb.de abrufbar.

Herausgeber und Vertrieb:	Forschungszentrum Jülich GmbH Zentralbibliothek, Verlag 52425 Jülich Tel.: +49 2461 61-5368 Fax: +49 2461 61-6103 zb-publikation@fz-juelich.de www.fz-juelich.de/zb
Umschlaggestaltung:	Grafische Medien, Forschungszentrum Jülich GmbH
Druck:	Grafische Medien, Forschungszentrum Jülich GmbH
Copyright:	Forschungszentrum Jülich 2020

Schriften des Forschungszentrums Jülich
Reihe Energie & Umwelt / Energy & Environment, Band / Volume 496

D468 (Diss., Wuppertal, Univ., 2018)

ISSN 1866-1793
ISBN 978-3-95806-481-2

Vollständig frei verfügbar über das Publikationsportal des Forschungszentrums Jülich (JuSER)
unter www.fz-juelich.de/zb/openaccess.

Abstract

Gravity waves drive global circulations in the mesosphere and stratosphere. Due to their small scales, they are usually not resolved in current global circulation models. Thus, their impact on the circulation is implemented in the form of simplified sub-models called parameterisation schemes. Several theoretical studies have highlighted that the assumptions on which these parameterisation schemes are based need to be reconsidered. However, the confirmation of these studies through measurements is still missing. A novel airborne remote sensing instrument, which can provide exactly such measurements, is the Gimballed Limb Observer for Radiance Imaging of the Atmosphere (GLORIA).

GLORIA has two different measurement modes suitable for gravity waves: full angle tomography and limited angle tomography. Full angle tomography allows for the reconstruction of the atmospheric temperature structure with a spatial resolution of 20 km in both horizontal directions and 200 m in the vertical at an accuracy of 0.5 K. This spatial resolution is very high for remote sensing instruments. Three-dimensional volumes reconstructed with limited angle tomography have a resolution of 30 km in flight direction, 70 km across flight track, and 400 m in the vertical at an accuracy of 0.7 K. Full angle tomography is better suitable for small-scale gravity waves with unknown orientation and limited angle tomography for non-stationary waves.

The first gravity wave field investigated in this thesis was measured above Iceland on 25 January 2016. Driven by the full wave characterisation achieved from the GLORIA measurements, the Gravity wave Regional Or Global RAy Tracer (GROGRAT) reveals a strong oblique propagation of this wave covering more than 2000 km horizontal distance. This strong oblique propagation happens mainly in a narrow altitude band between 15 km and 20 km. Even though many studies predicted oblique gravity wave propagation, it still surprises that it take place in such a narrow altitude band. Further, GROGRAT shows that in the case of solely vertical propagation, which is a common assumption used for gravity wave parameterisation schemes, the wave momentum is deposited not only at a completely wrong geographical location but

also at a wrong altitude.

The importance of non-linear processes for gravity wave propagation is investigated on a second case study using GLORIA measurements taken above southern Scandinavia on 28 January 2016. The results of the linear propagation model GROGRAT with satellite measurements from the Atmospheric Infrared Sounder (AIRS) agree very well if a detailed observational filter is considered for the satellite measurements. Thus, non-linear processes seem to be negligible for the propagation of the investigated gravity waves. A further result of this study is, that one needs to consider the detailed observational filter of a measurement technique to draw meaningful conclusions from comparisons between observations and models.

Zusammenfassung

Schwerewellen treiben globale Zirkulationen in der Strato- und Mesosphäre an. Aufgrund ihrer kleinen Skalen werden Schwerewellen in der Regel in heutigen globalen Zirkulationsmodellen nicht aufgelöst. Daher wird ihr Einfluss auf die Zirkulation durch sehr vereinfachte Teilmodelle, genannt Schwerewellenparameterisierungen, angenähert. Mehrere theoretische Studien haben gezeigt, dass die diesen zugrunde liegenden Annahmen, dringend überdacht werden müssen. Allerdings fehlt diesen Studien bis heute die Bestätigung durch Messungen. Der flugzeuggetragene Infrarot-Horizontsondierer GLORIA (Gimballed Limb Observer for Radiance Imaging of the Atmosphere) kann eben solche Messungen bereitstellen.

GLORIA hat zwei für Schwerewellen geeignete Messmodi: Vollwinkeltomographie und Teilwinkeltomographie. Diese Arbeit zeigt, dass beide Methoden geeignet sind mesoskalige Schwerewellen vollständig zu charakterisieren. Durch Vollwinkeltomographie lassen sich für die Fernerkundung sehr hohe räumliche Auflösungen von 20 km in beiden horizontalen Richtungen und 200 m in der Vertikalen bei einer Messgenauigkeit von 0.5 K erreichen. Mit Teilwinkeltomographie rekonstruierte Temperaturstrukturen haben horizontale Auflösungen in Flugrichtung von 30 km und quer zur Flugrichtung von 70 km. Die vertikale Auflösung liegt bei 400 m, die Messgenauigkeit bei 0.7 K. Vollwinkeltomographie eignet sich besser für kleinskalige Schwerewellen mit unbekannter Orientierung und Teilwinkeltomographie für zeitlich veränderliche Wellen.

Das erste im Rahmen dieser Arbeit untersuchte Schwerewellenfeld wurde am 25. Januar 2016 über Island gemessen. Angetrieben durch die vollständige Wellencharakterisierung von GLORIA, zeigt das Schwerewellenausbreitungsmodell GROGRAT (Gravity wave Regional Or Global Ray Tracer) eine sehr stark horizontale Ausbreitung der Welle über eine Distanz von mehr als 2000 km. Diese stark horizontale Ausbreitung findet hauptsächlich in einem sehr schmalen Höhenband zwischen 15 km und 20 km statt. Obwohl mehrere Studien horizontale Ausbreitung von Schwerewellen vorhergesagt haben, ist die Ausbreitung in einem so schmalen Höhenband überraschend. GROGRAT zeigt auch, dass

im Falle einer rein vertikalen Ausbreitung dieser Schwerewelle, wie sie in Schwerewellenparameterisierungen angenommen wird, der Schwerewellenimpuls nicht nur an der komplett falschen geographischen Position sondern auch auf der falschen Höhe abgelagert würde.

Die Bedeutung von nicht-linearen Prozessen bei der Ausbreitung von Schwerewellen wird an einer zweiten Fallstudie mit GLORIA Messungen vom 28. Januar 2016 über Südskandinavien näher betrachtet. Vergleiche zwischen Ergebnissen des linearen Ausbreitungsmodells GROGRAT mit Satellitenmessungen des Atmospheric Infrared Sounder (AIRS), zeigen, unter Einbeziehung des vollständigen Beobachtungsfilters des Satelliteninstruments, eine gute Übereinstimmung. Dies lässt darauf schließen, dass nicht-lineare Prozesse bei der Ausbreitung dieser Schwerewelle keine Rolle gespielt haben. Als Nebenergebnis zeigt diese Studie auch, dass die Anwendung des vollständigen Beobachtungsfilters zwingend erforderlich ist, um sinnvolle Schlüsse aus dem Vergleich zwischen Messung und Modell ziehen zu können.

Contents

1 Introduction

Gravity waves are waves in a fluid medium with buoyancy and gravity as restoring forces. The most familiar example of gravity waves are ocean waves at the interface between water and air. In addition to these surface waves, gravity waves can also exist inside one single medium, where they are sustained by density gradients. These waves are called internal gravity waves. In the atmosphere internal gravity waves are defined via temperature, wind and pressure fluctuations. The temperature fluctuations caused by gravity waves can lead to the condensation of water and the formation of clouds. Figure 1.1 shows such gravity wave-generated clouds above the Alps. They are generally aligned with the main mountain ridge. The occurrence of two or more of these elongated, parallel cloud patterns is characteristic of gravity wave-generated clouds.

In the atmosphere, gravity waves are, for example, generated by flow over orography. Blocked by the orographic elevation, the air mass is forced to rise. Due to the decreasing atmospheric pressure, it expands and cools adiabatically during the upwards motion. The density gradient in a stable atmosphere is in general lower than the adiabatic density gradient. When the air arrives at the mountain top, it is denser and, therefore, heavier than the surrounding air. Gravity then accelerates the air downwards. When the air reaches its level of neutral buoyancy (the level where, the density of the air mass matches the surrounding density), the downwards movement slows down. The density of the air parcel is now smaller than the surrounding and it gets accelerated back upwards by buoyancy. A harmonic oscillation around the level of neutral buoyancy is generated. Every oscillating air parcel is coupled to the air parcels above and below and a vertically propagating wave is created. Any process that can force air upwards or downwards, can gen-

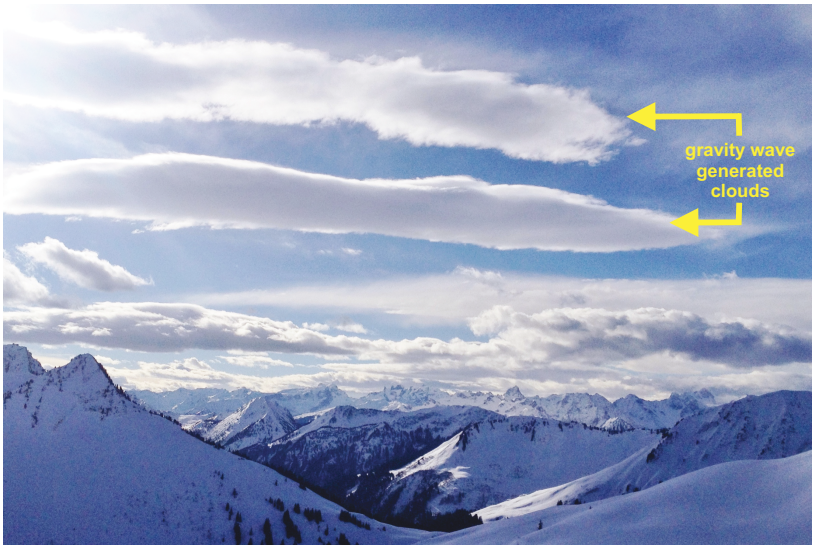

Figure 1.1: Clouds induced by a gravity wave above the Austrian Alps near Mellau. Picture by Jörn Ungermann.

erate a gravity wave. Besides the flow over orography, convection, jets, and fronts are the most important atmospheric gravity wave sources. These main gravity wave sources are located in the troposphere, that is between the Earth surface and altitudes of 10 km to 15 km.

Gravity waves can propagate in all spatial dimensions transporting energy over large distances. They break when the perturbation caused by the gravity wave becomes sufficiently large to locally overcome the stable stratification of the air. One possibility, how this can happen, is that due to the decreasing atmospheric pressure, which leads to an exponential growth of the gravity wave amplitude, the gravity wave becomes unstable and breaks. In these breaking processes, the momentum of the gravity wave is completely or partially transferred to the background either in form of turbulences and/or in form of a flow acceleration. The flow acceleration always happens in the direction in which the gravity wave was intrinsically propagating. Turbulence caused by gravity waves is a major safety issue for aviation and a better understanding of the underlying processes could drastically enhance the accuracy of its

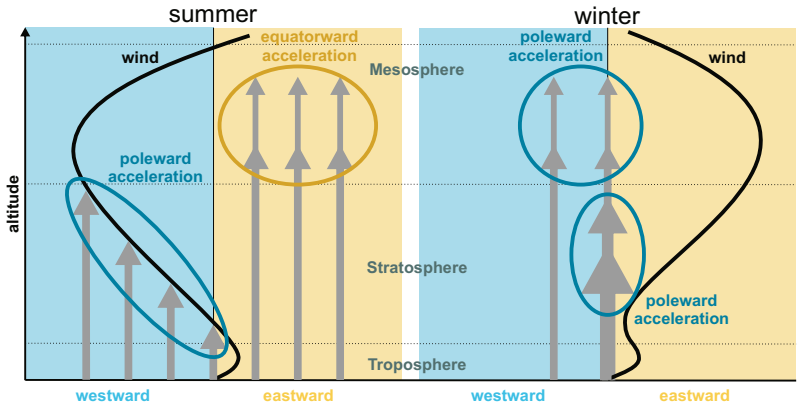

Figure 1.2: Wind filtering of gravity waves. The dissipation altitude of atmospheric gravity waves (grey arrows) strongly depend on their phase velocity with respect to the background wind (black line) and their amplitude (thickness of the grey arrow). The direction in which the background flow is accelerated by a breaking or dissipating gravity wave is determined by the propagation direction of the gravity wave. The Coriolis force, further introduces a poleward (equatorward) acceleration for westward (eastward) gravity wave drag.

prediction (Sharman et al., 2012).

Another gravity wave dissipation process is wind filtering (Figure 1.2). It happens when the phase velocity of a gravity wave equals the horizontal background wind speed. The altitude at which this happens is called a critical layer. The effect of wind filtering is different in summer and winter due to the climatological differences in the horizontal wind profiles and the importance of different gravity wave sources which lead to gravity waves of different spatial and temporal scales.

In summer, the background wind in the stratosphere and lower mesosphere is directed westward and increasing with altitude. The main excitation mechanism of gravity waves in summer is convection. Convective gravity waves can have all kinds of phase speeds and propagation directions. Gravity waves with westward phase velocities meet critical levels at different altitudes. When dissipating, they exert a westward acceleration onto the background wind. Due to the Coriolis force and

the conservation of angular momentum, westward accelerated air will also move polewards. Contrary, gravity waves with eastward phase velocities can propagate up to higher altitudes without being filtered by the background wind. Once their amplitude becomes too large, they become unstable and break. This happens often in the mesosphere, where they then decelerate the westward background flow. The deceleration leads to the summer time wind reversal in the mesosphere–lower thermosphere region (Holton, 1982, 1983). The conservation of angular momentum induces an equatorward residual circulation.

In winter, the background wind in the upper stratosphere and lower mesosphere is blowing eastward. Consequently, the filtering would appear reversed. However, in winter the main sources of gravity waves are flow over orography, jets, and fronts. These processes generate gravity waves usually propagating against the tropospheric background flow, thus westward, with phase speeds close to zero. These gravity waves can have very high amplitudes and, thus, break often at comparably low altitudes in the stratosphere, where they accelerate the background flow westward.

Another aspect which differs from summer to winter is the occurrence of planetary waves. These larger-scale atmospheric waves, which are driven by the conservation of potential vorticity, appear more frequently in winter and propagate intrinsically westward. Especially the planetary waves with low phase velocities mainly break in the stratosphere. There, they lead to a westward and poleward acceleration of the background flow. In the winter stratosphere, this acceleration of the flow by planetary waves is in general stronger than the acceleration through gravity waves. A detailed discussion of planetary waves is beyond the scope of this work, but can be found, for example, in Holton (1992).

Figure 1.3 summarises global wind circulations resulting from the dissipation (breaking and filtering) of gravity waves and planetary waves. According to the concept of mass conservation, the poleward movement on both hemispheres in the stratosphere forces air to ascend over the equator and descend over the poles. This stratospheric circulation is known as Brewer–Dobson circulation (BDC). It is mainly driven by planetary waves, but gravity waves have been shown to strongly influence

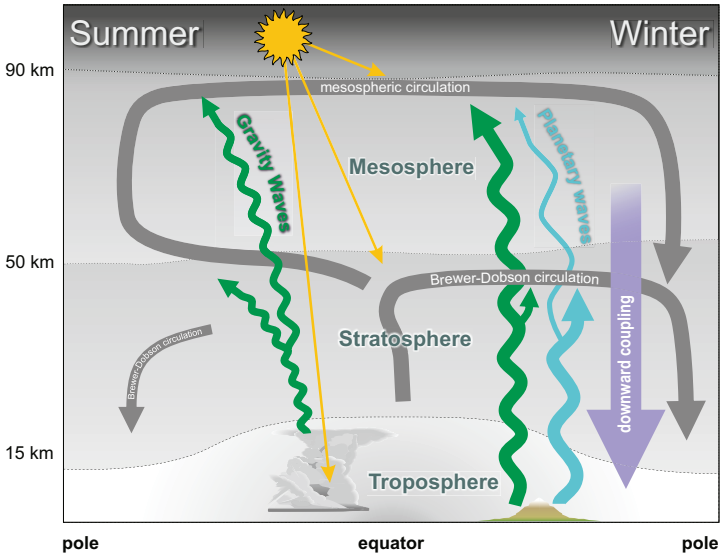

Figure 1.3: Global atmospheric circulations driven by gravity waves and planetary waves.

its variability. Moreover, the decreased activity of planetary waves in summer, cause the summer branch of the BDC to be mainly driven by gravity waves (Alexander and Rosenlof, 2003; Butchart, 2014).

The meridional circulation in the mesosphere forces air to ascend over the summer pole and descend over the winter pole. While ascending (respectively descending) the air cools down (respectively heats up) according to adiabatic expansion (respectively shrinking). The upwelling leads to a cold summer mesopause (Holton, 1982, 1983) and the downwelling to a warm winter stratopause (McLandress, 1998; Siskind, 2014). Downward coupling processes link all these middle atmospheric circulations with near-surface seasonal weather and regional climate (Scaife et al., 2016; Kidston et al., 2015).

Gravity waves have horizontal scales ranging from couple kilometres to several thousand kilometres. Vertical scales vary from hundreds of metres to approximately 50 km. Due to computational constraints, only the large-scale part of the gravity wave spectrum can be resolved in cur-

rent general circulation models. Small-scale gravity waves are simplified in form of parameterisation schemes. Several studies show that approximations and inaccuracies of parameterisation schemes of sub-grid-scale processes can cause large uncertainties in climate change projections (Shepherd, 2014). For example, climate change projections differ by up to 2 K surface temperature (Sigmond and Scinocca, 2010) and several hPa surface pressure at polar latitudes (Sandu et al., 2016) depending on the set-up of the gravity wave parameterisation scheme. Improved climate change projections and mid-term weather forecasts therefore require more advanced parameterisation schemes as proposed by various studies (e.g. Bushell et al., 2015; de la Camara and Lott, 2015; Amemiya and Sato, 2016).

One of the largest simplifications, used nowadays for gravity wave parameterisation schemes, is to assume solely vertical propagation. Several modelling studies have highlighted the importance of 3-D propagation to precisely reproduce middle atmospheric circulation patterns (Sato et al., 2009; Kalisch et al., 2014; Ribstein and Achatz, 2016). Furthermore, gravity wave source distributions and launch parameters, such as propagation direction and wavelength spectrum, are often oversimplified in parameterisation schemes (Alexander and Dunkerton, 1999; Richter et al., 2010; Garcia et al., 2017) and need validation by observations (Geller et al., 2013). Another simplification of parameterisation schemes lies in the assumption that momentum transfer between gravity wave and background flow only happens during dissipation, saturation or breaking processes. However, several theoretical studies show that momentum deposition of gravity waves on the background flow also takes place in absence of dissipation, saturation, and breaking (Buehler and McIntyre, 2003; Eberly and Sutherland, 2014; Boeloeni et al., 2016). These studies predict, that in certain cases transient direct interactions of gravity waves with the background flow can even be responsible for the major part of gravity wave momentum deposition. To figure out, how severely these simplifications impact seasonal weather prediction and climate projections, a proper understanding of the involved processes is required. Therefore, measurements are needed which allow detailed gravity wave propagation studies. To derive the propagation direction

of a gravity wave, a full wave characterisation is necessary (Alexander et al., 2010).

Such a full wave characterisation is, in principle, possible from various measurement techniques. Several methods have been developed to evaluate in situ data from close-to-vertical profiles taken by radiosondes, dropsondes, or falling spheres. These methods include hodograph analysis (Guest et al., 2000), the Stokes method (Eckermann and Vincent, 1989), or a combination of wind and temperature measurements in a common approach (Wang and Geller, 2003; Zhang et al., 2014). Furthermore, there are multiple techniques based on horizontal 1-D measurements for example from airplane instrumentation (Alexander and Pfister, 1995; Fritts et al., 2016; Smith et al., 2016; Wagner et al., 2017) and observations by super-pressure balloons (Boccara et al., 2008; Hertzog et al., 2008). All these methods infer the wave direction via polarization and dispersion relations, as they do not reveal the 3-D wave structure directly.

In the last years, new remote measurement concepts evolved, which facilitate measurements of 3-D gravity wave structures directly. In the mesosphere, a full wave characterisation of small-scale gravity waves has been achieved with the Middle Atmosphere Alomar Radar System (MAARSY; Stober et al., 2013). For medium-scale gravity waves in the mesosphere, a full characterisation has been derived by combining lidar and airglow imager measurements (Bossert et al., 2015; Lu et al., 2015; Cao et al., 2016). However, all these observations are limited to a few ground-based stations. Further, it is difficult to link observations at altitudes as high as the mesopause region to specific gravity wave sources, which are usually located at much lower altitudes in the troposphere and lower stratosphere. First measurements of 3-D gravity wave structures in the stratosphere using satellite instruments are presented by Ern et al. (2017) and Wright et al. (2017). These studies are based on nadir observations of the Atmospheric Infrared Sounder (AIRS) satellite instrument and are limited by the coarse vertical resolution of the instrument. This implies that gravity waves with vertical wavelengths below 15 km are invisible. Some of the limitations originating from this coarse vertical resolution of AIRS will be discussed in this thesis. So far no measure-

ment technique exists to measure the 3-D structure of mesoscale gravity waves in the lower stratosphere with high spatial resolution.

A novel technique to measure gravity waves in the upper troposphere–lower stratosphere, i.e., close to the gravity wave sources, is airborne limb imaging. Limb imaging allows for a 3-D reconstruction of the atmospheric temperature and consequently a full characterisation of mesoscale gravity waves. The development of the Gimballed Limb Observer for Radiance Imaging of the Atmosphere (GLORIA) is the first implementation of such an airborne infrared limb imager (Friedl-Vallon et al., 2014; Riese et al., 2014). The GLORIA instrument is a Fourier transform spectrometer with a 2-D detector array measuring spectrally resolved infrared radiation between 780 cm^{-1} and 1400 cm^{-1} (7 µm to 13 µm). Like an infrared camera, GLORIA measures the characteristic thermal emissions of trace gases and particles in the atmosphere. The emitted radiation depends on the amount and temperature of these trace gases and particles. Thus, GLORIA enables the retrieval of atmospheric temperature and trace gas distributions.

The GLORIA instrument is mounted in the belly pod of the German High Altitude and Long Range Research Aircraft (HALO; DLR, 2018) and looks towards the horizon - also called limb of the Earth - on the right side of the aircraft (Figure 1.4). It can change its horizontal viewing direction from 45° (right forward) to 135° (right backward) with respect to the aircraft's heading. If a volume of air is such observed under different angles, it may be reconstructed using tomographic methods (e.g. Natterer, 2001). Measuring emitted radiation from all 360° around a volume, for example, by flying a circle, is called full angle tomography (FAT). Former studies of FAT for trace gas retrievals showed, that this technique improves the horizontal resolution of limb sounders by an order of magnitude down to 20 km while retaining the high vertical resolution of approximately 200 m in the vertical (Ungermann et al., 2010b). Since flying in a circular pattern of sufficient size can take more than two hours, FAT is only suitable for measurements in steady atmospheric states, where the conditions do not change significantly during the acquisition time. Accounting for the change of the atmosphere during acquisition is possible for trace gas retrievals by including advection

Figure 1.4: The German high altitude and long range research aircraft (HALO) at the airport in Kiruna, Sweden. Picture by Peter Preusse.

(Ungermann et al., 2011). The temperature structure in the presence of gravity wave events, however, is in general governed by a multitude of waves with different spatial and temporal scales. The a priori knowledge of the temporal development of these waves is not sufficient to retrieve a fast changing temperature structure using FAT. Furthermore, air traffic control restrictions and the requirements imposed by other instruments may prevent complicated closed flight patterns. Due to the horizontal scanning capabilities of the GLORIA instrument, the same volume of air is measured from multiple angles already during simple straight flights. The technique of reconstructing a 3-D volume using measurements from a limited set of angles is called limited angle tomography (LAT). However, LAT inversion problems are notoriously difficult to solve as they are in general seriously ill-posed (Natterer, 2001). Thus, the first question investigated in this thesis will be: **Can LAT be used to study mesoscale gravity waves?**

In winter 2015/2016 an aircraft campaign with the HALO aircraft took place to study different gravity wave aspects as well as chemical processes in the Arctic polar winter. The campaign base was chosen to be located in Kiruna, Sweden, as the Scandinavian mountains are one of the major orographic gravity wave sources on the northern hemisphere.

Furthermore, the location of Kiruna close to the polar circle made it a perfect choice for flights into the polar vortex. During the campaign six flights dedicated to gravity waves were performed. To achieve the best possible measurement results, scientific research flights are planned using different forecasts and a tailor-made flight planning tool. The flight patterns can be adjusted to the atmospheric situation and special instrument requirements. This raises the questions: **What is the optimal flight strategy to observe mesoscale gravity waves with GLORIA? Are the achieved 3-D volumes of atmospheric temperature sufficient in size and spatial resolution to fully characterise these waves? How does the measurement set-up (LAT vs FAT) influence the quality of retrieved wave parameters?**

As mentioned earlier, nowadays general circulation models use simplified gravity wave parameterisation schemes, which assume solely vertical propagation. Comparisons between measurements and general circulation models using these simplified gravity wave parameterisation schemes showed that the models predict too low temperatures for the southern winter stratosphere (McLandress et al., 2012; Garcia et al., 2017). This cold-pole bias likely arises from too weak downwelling in this region. McLandress et al. (2012) show that missing orographic gravity wave drag around 60° S might be the cause of this cold-pole bias. Due to the lack of orography at 60° S, McLandress et al. (2012) assume that oblique propagation of gravity waves could be responsible for this. However, the closest mountains are located around 55° S and 65° S, thus, more than 500 km away. Till today there exist no measurements, showing that oblique propagation can happen over such large distances. During the aircraft campaign mentioned above, an orographically excited gravity wave above Iceland with strong oblique propagation was predicted for the 25 January 2016. This thesis will examine the following scientific questions: **Can GLORIA measurements confirm that oblique propagation can happen over large distances? How large are the discrepancies between reality and simplified gravity wave parameterisation schemes?**

Linear ray-tracing models are often used to approximate the propagation of gravity waves. They can help to identify sources (Gerrard et al.,

2004; Preusse et al., 2009a; Pramitha et al., 2015) or study oblique propagation (Kalisch et al., 2014; Ribstein and Achatz, 2016). However, similar to gravity wave parameterisations in general circulation models, these ray-tracing models do only account for momentum transfer between gravity waves and background flow during dissipation, saturation and breaking processes. By combining gravity wave observations from GLORIA with satellite measurements, this thesis will investigate: **How meaningful are the results of linear ray-tracing models? How well do they agree with observations?**

The organisation of this work is as follows: First, a short overview about important points of gravity wave theory is given in Chapter 2. Chapter 3 describes the data acquisition, including the aircraft campaign, important instruments on board of HALO with an emphasis on the GLORIA instrument, and the AIRS satellite instrument. Further, Chapter 3 includes a short description of the analysis and reanalysis general circulation model data from the European Centre for Medium-Range Weather Forecasts, which is used to support the scientific analysis of the GLORIA measurements. To analyse the acquired measurement and model data with respect to gravity waves, the atmospheric variables first have to be separated into large-scale background and small-scale gravity wave perturbation. Afterwards the gravity wave structures have to be fully characterised and their wave parameters have to be derived. The details of these analysis techniques are presented in Chapter 4. Chapter 5 investigates the sensitivity of GLORIA to gravity waves for the measurement concepts of LAT and FAT. The scientific questions regarding the ability to fully characterise gravity waves from GLORIA measurements will be investigated in this Chapter. The GLORIA measurement results from 25 January 2016 are analysed with respect to gravity wave sources and propagation in Chapter 6. A special focus will be given to the study of oblique gravity wave propagation and the errors introduced by simplified parameterisations. Further measurements on 28 January 2016 above Scandinavia, show another interesting gravity wave case (Chapter 7). The GLORIA measurements of this day are used to question the validity of linear wave theory.

2 Gravity wave theory

Gravity waves in the atmosphere are excited by the vertical displacement of air parcels. The original equilibrium of forces is disturbed and the air parcel starts to oscillate around its level of neutral buoyancy. This chapter gives an overview over important processes involved in the excitation and propagation of gravity waves. First, it will be described how a displacement of an air parcel leads to a wave motion and which dispersion relation the created wave follows (Section 2.1). The relationship of wave equations for different atmospheric quantities like wind and temperature are derived in Section 2.2. Afterwards, the propagation and energy transport of gravity waves through the atmosphere is discussed (Section 2.3). Finally, different sources of gravity waves are presented (Section 2.4).

2.1 Dispersion relation

Due to the stable stratification of the atmosphere, i.e. to the fact that pressure and density decrease with altitude, an upward displaced air parcel will expand. During a fast upward displacement, the air parcel cannot exchange heat with the surrounding air and, thus, will cool in dry air according to the adiabatic temperature gradient

$$\Gamma = \left(\frac{dT}{dz}\right)_{\text{adiab.}} = -\frac{g}{c_p} \approx -9.76\frac{K}{km}, \tag{2.1}$$

with temperature T, altitude z, standard gravity g and specific heat capacity of air c_p. If the real atmospheric temperature gradient $\gamma = \frac{dT}{dz}$

is larger[1] than the adiabatic gradient Γ, an adiabatically upward displaced air parcel will be colder than the surrounding air. The difference between the temperature T_p of the displaced air parcel and the temperature T of the surrounding air is given by

$$T_p - T = (\Gamma - \gamma)\xi', \tag{2.2}$$

where ξ' indicates how far the air parcel is displaced from its original position of neutral buoyancy and is called vertical displacement.

During the adiabatic upwards or downwards movements, the air parcel stays in pressure balance with the surrounding:

$$R_s \rho_p T_p = p = R_s \rho T, \tag{2.3}$$

where R_s is the specific gas constant of air, T the temperature and ρ the density of the surrounding air, and T_p and ρ_p are the new temperature and density of the displaced air parcel, respectively. If the air parcel is colder than the surrounding air, it has to be denser and thus heavier. The force accelerating the air parcel downward is given by the difference in gravity between the displaced air parcel of mass m_p and an air parcel of the surrounding air with the same volume V, which has the mass m:

$$F_g = -g m_p + g m = -g V(\rho_p - \rho) = -m_p \frac{g}{T}(\gamma - \Gamma)\xi'. \tag{2.4}$$

This force is proportional to the vertical displacement ξ'. Thus, a harmonic oscillation around the position of neutral buoyancy with Buoyancy frequency $N = \sqrt{\frac{g}{T}(\gamma - \Gamma)}$, also called Brunt-Väisälä frequency, is excited.

In reality, the air parcel does not move solely vertically, but on a slanted line at an angle φ to the vertical (Figure 2.1 a). The force accelerating or decelerating the air parcel along this slanted line is

$$F = F_g \cos\varphi = -m_p N^2 \cos\varphi \left(\xi' \cos\varphi\right) = -m_p N^2 \cos^2\varphi \, \xi'. \tag{2.5}$$

[1] less negative or positive

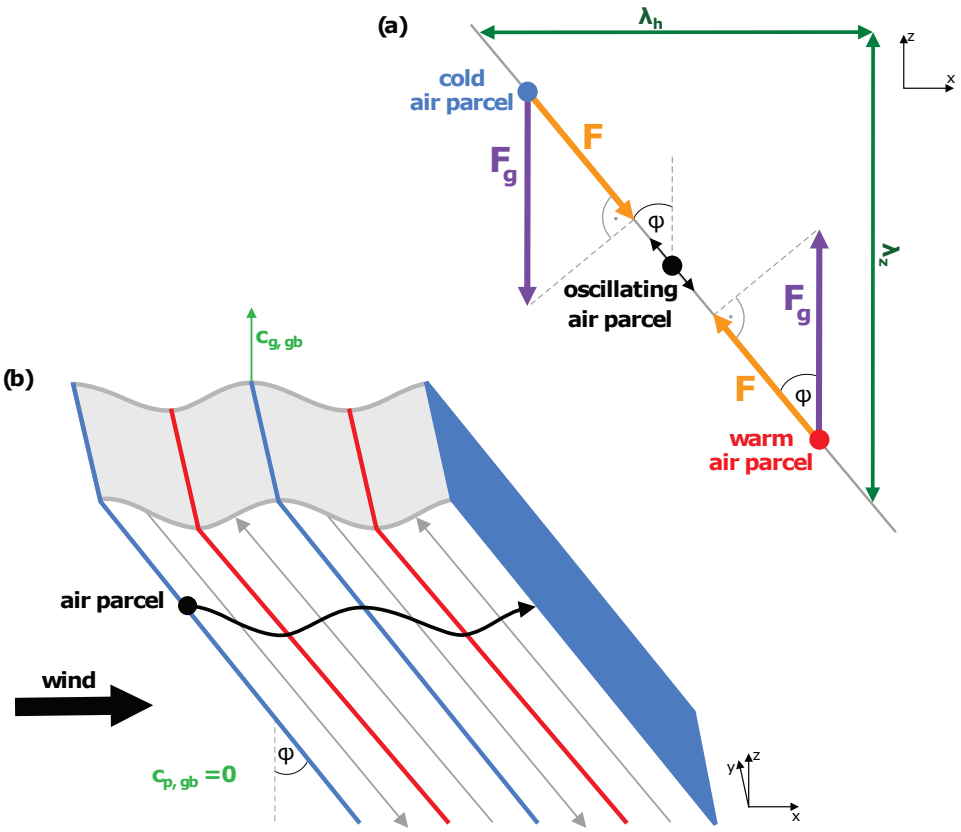

Figure 2.1: Sketch of the oscillations induced by a gravity wave. Panel (a) shows the harmonic oscillation of an air parcel influenced by a gravity wave in a stationary ambient. An air parcel which is lifted by an arbitrary source process expands and cools down according to the adiabatic temperature gradient. If the adiabatic temperature gradient is smaller than the temperature gradient of the surrounding air, the air parcel will be colder and denser than the surrounding air. The higher density and, thus, higher gravity, will force the air parcel downwards. Due to the adiabatic heating and shrinking it will then be warmer, but less dense than the surrounding. Now buoyancy will accelerate the air parcel upwards. Panel (b) depicts the phase fronts of a stationary gravity wave in a horizontal background wind. The movement of an air parcel in the background wind gets disturbed by the gravity wave and the air parcel continues on a wave trajectory (black line). The thin grey lines stand for the gravity wave phase lines with maximal wind perturbation. Red and blue lines indicate warm and cold phase fronts, respectively.

The air parcel oscillates with intrinsic frequency

$$\omega^2 = N\cos\varphi = N\frac{\lambda_z}{\sqrt{\lambda_h^2+\lambda_z^2}} = N\frac{k_h}{\sqrt{k_h^2+k_z^2}} \leq N, \tag{2.6}$$

with horizontal wavelength $\lambda_h = \frac{2\pi}{k_h}$, horizontal wave number k_h, vertical wavelength $\lambda_z = \frac{2\pi}{m}$, and vertical wave number m. In a 3-D coordinate system with horizontal axes x and y, and vertical axis z, the wave vector $\boldsymbol{k} = (k,l,m)$ is defined by the three wave numbers k, l, and m in x, y, and z direction, respectively. In this case, the horizontal wave number is given by $k_h = \sqrt{k^2+l^2}$ and the intrinsic frequency becomes

$$\omega^2 = N\frac{\sqrt{k^2+l^2}}{\sqrt{k^2+l^2+m^2}}. \tag{2.7}$$

This equation relating temporal and spatial characteristics of a wave with each other is called dispersion relation. Including effects due to Earth's rotation and the compressibility of air, leads to the full dispersion relation for atmospheric gravity waves (Fritts and Alexander, 2003):

$$\omega^2 = \frac{(k^2+l^2)N^2 + f^2\left(m^2+\frac{1}{4H^2}\right)}{k^2+l^2+m^2+\frac{1}{4H^2}} \tag{2.8}$$

where $f = \frac{4\pi}{24\,\mathrm{h}}\sin(\theta)$ denotes the Coriolis frequency, θ the latitude, and H the density scale height in which the density decreases by a factor of Euler's number e.

In the atmosphere, H is on the order of 7.5 km. For waves with vertical wavelengths below 20 km the density scale height term $\frac{1}{4H^2}$ is much smaller than m^2 and, thus, can be neglected. This approximation is called Boussinesq approximation and neglects all effects caused by fast changes in density, e.g. sound waves. For waves with horizontal wavelength $\lambda_h = \frac{2\pi}{\sqrt{k^2+l^2}}$ much larger than vertical wavelength $\lambda_z = \frac{2\pi}{m}$ (which is the case for all waves measured by GLORIA), the dispersion relation

can be further simplified to

$$\omega^2 = \frac{(k^2 + l^2)N^2}{m^2} + f^2. \tag{2.9}$$

Unless stated otherwise, this simplified dispersion relation is used in this work. If the x-axis is chosen to be oriented along the horizontal wave vector the wave motion becomes two-dimensional and the dispersion relation can be written as

$$\omega^2 = \frac{k^2 N^2}{m^2} + f^2. \tag{2.10}$$

Solving the three-dimensional dispersion relation (Equation 2.9) for the vertical wave number

$$|m| = \sqrt{\frac{(k^2 + l^2)N^2}{\omega^2 - f^2}}, \tag{2.11}$$

directly shows, that to keep m physically meaningful and, thus, real valued, ω has to be larger than f. Hence, the intrinsic frequency ω of atmospheric gravity waves is confined to the range $f < \omega \leq N$.

The group velocity $\boldsymbol{c}_g$ of a wave is the velocity at which a wave packet propagates through the atmosphere and transports energy and momentum. It is defined as the wave number derivative of the intrinsic frequency:

$$\boldsymbol{c}_g \equiv \boldsymbol{\nabla}_k \omega = \frac{N^2\sqrt{k^2 + l^2}}{\omega m^3} \begin{pmatrix} \frac{mk}{\sqrt{k^2+l^2}} \\ \frac{ml}{\sqrt{k^2+l^2}} \\ -\sqrt{k^2 + l^2} \end{pmatrix}. \tag{2.12}$$

Without Earth's rotation the intrinsic frequency becomes $\omega \approx \frac{N\sqrt{k^2+l^2}}{|m|}$

and the group velocity simplifies to

$$\boldsymbol{c}_g = \frac{N}{m^2} \begin{pmatrix} |m| \frac{k}{\sqrt{k^2+l^2}} \\ |m| \frac{l}{\sqrt{k^2+l^2}} \\ -\mathrm{sgn}(m)\sqrt{k^2+l^2} \end{pmatrix}. \tag{2.13}$$

This equation directly reveals, that the group velocity $\boldsymbol{c}_g$ of gravity waves is perpendicular to the wave vector $\boldsymbol{k}$ and, thus, parallel to the phase lines. Further, the vertical group velocity is opposite to the vertical wave number meaning that a downward pointing wave vector indicates upward energy transport. The horizontal group velocity points in the same direction as the horizontal wave vector $\boldsymbol{k}_h = (k, l)$.

The phase velocity $\boldsymbol{c}_p$ of a wave determines how fast and in which direction the wave crests and troughs of a wave move. It is defined as $\boldsymbol{c}_p \equiv \frac{\omega \boldsymbol{k}}{|\boldsymbol{k}|^2}$ and is parallel to the wave vector $\boldsymbol{k}$.

Until now, a stationary ambient was assumed. If the air is moving, the frequency of the gravity wave is Doppler shifted. From the point of view of a stationary observer the gravity wave has the ground-based frequency

$$\Omega = \left(1 + \bar{\boldsymbol{u}} \cdot \frac{\boldsymbol{c}_p}{|\boldsymbol{c}_p|^2}\right) \omega = \omega + \bar{\boldsymbol{u}} \cdot \boldsymbol{k}, \tag{2.14}$$

with background wind speed $\bar{\boldsymbol{u}}$ and gravity wave phase speed $\boldsymbol{c}_p = \frac{\omega \boldsymbol{k}}{|\boldsymbol{k}|^2}$. It is important to note, that the dispersion relation (Equations 2.7 – 2.10) links the intrinsic frequency ω with the wave vector $\boldsymbol{k}$, not the ground-based frequency Ω.

Due to the Doppler shift, also the group velocity and the phase velocity of the wave change:

$$\boldsymbol{c}_{g,\,gb} \equiv \boldsymbol{\nabla}_k \Omega = \boldsymbol{c}_g + \bar{\boldsymbol{u}}, \tag{2.15}$$

and

$$\boldsymbol{c}_{p,\,gb} \equiv \frac{\Omega \boldsymbol{k}}{|\boldsymbol{k}|^2} = \boldsymbol{c}_p + (\boldsymbol{k} \cdot \bar{\boldsymbol{u}})\,\frac{\boldsymbol{k}}{|\boldsymbol{k}|^2}, \tag{2.16}$$

where $\boldsymbol{c}_{g,\,gb}$ stands for the ground-based group velocity, $\boldsymbol{c}_{p,\,gb}$ for the ground-based phase velocity, and $\boldsymbol{c}_g$ and $\boldsymbol{c}_p$ represent the intrinsic group and phase velocities of the wave in a stationary ambient.

Figure 2.1 b shows a gravity wave in a one-dimensional background wind $\bar{\boldsymbol{u}} = (U_0, 0, 0)$, $U_0 > 0$, with intrinsic frequency $\omega = -\boldsymbol{k} \cdot \bar{\boldsymbol{u}} = -kU_0$ as seen from a stationary observer on the ground. The coordinate system is chosen in a way, that the x-axis is oriented along the horizontal wave vector ($\boldsymbol{k} = (k, 0, m)$, $k < 0$ and $m < 0$). In this special case, the ground-based phase velocity $\boldsymbol{c}_{p,\,gb} = \boldsymbol{c}_p + (\boldsymbol{k} \cdot \bar{\boldsymbol{u}})\,\frac{\boldsymbol{k}}{|\boldsymbol{k}|^2}$ becomes zero. The wave phases do not move and the wave pattern is stationary in time. The air parcels, in contrast, move from left to right with the background wind on horizontal trajectories. These trajectories get distorted by the gravity wave and follow now a wave-like pattern (black line). The ground-based group velocity reduces to solely vertical:

$$\boldsymbol{c}_{g,\,gb} = \boldsymbol{c}_g + \bar{\boldsymbol{u}} = \frac{N}{m^2} \begin{pmatrix} |m|\,\mathrm{sgn}(k) \\ 0 \\ -\mathrm{sgn}(m)|k| \end{pmatrix} + \begin{pmatrix} U_0 \\ 0 \\ 0 \end{pmatrix} = \begin{pmatrix} 0 \\ 0 \\ |k| \end{pmatrix}. \tag{2.17}$$

The wave transports energy upwards. It will be shown later (Section 2.4), that a gravity wave excited by a wind flow over a mountain ridge has exactly such characteristics.

2.2 Polarisation relations

The development in space and time of the vertical displacement ξ' caused by a gravity wave can be described by a sinusoid

$$\xi'(x, y, z, t) = \hat{\xi} \sin(kx + ly + mz - \omega t + \phi), \tag{2.18}$$

with $\hat{\xi}$ the vertical displacement amplitude and ϕ the phase of the wave.

A positive (upward) displacement leads to a cooling and thus a negative temperature perturbation:

$$T'(x,y,z,t) = -(\gamma - \Gamma)\xi'(x,y,z,t) = -\frac{TN^2}{g}\,\xi'(x,y,z,t). \tag{2.19}$$

The amplitudes of vertical displacement $\hat{\xi}$ and temperature $\hat{T}$ are related by

$$\hat{T} = -\frac{TN^2}{g}\,\hat{\xi}. \tag{2.20}$$

The vertical wind perturbation is the temporal derivative of the vertical displacement:

$$w'(x,y,z,t) = \frac{\partial \xi'}{\partial t} = -\omega\hat{\xi}\cos(kx + ly + mz - \omega t + \phi). \tag{2.21}$$

Without Earth rotation, the relation of vertical wind and horizontal wind is given by the ratio of the respective wavelengths. Thus, the horizontal wind perturbation u_h' can be written as

$$u_h'(x,y,z,t) = \frac{m}{\sqrt{k^2+l^2}}\,w'(x,y,z,t) = \sqrt{\frac{N^2}{\omega^2} - 1}\,w'(x,y,z,t). \tag{2.22}$$

One finds for typical stratospheric values, that the horizontal wind amplitude $\hat{u}_h$ in units of $[\mathrm{m\,s^{-1}}]$ is about twice the temperature amplitude in units of [K]:

$$\hat{u}_h = -\frac{m}{\sqrt{k^2+l^2}}\omega\hat{\xi} = \frac{g}{\bar{T}N}\hat{T} \approx \frac{10}{250\cdot 0.02}\hat{T}\left(\frac{m}{sK}\right) = 2\hat{T}\left(\frac{m}{sK}\right). \tag{2.23}$$

The Earth rotation induces an additional rotational component of the wind, which is significant for waves with ω close to the Coriolis parameter f. In this case, the horizontal wind is divided into components

parallel and perpendicular to the wave vector:

$$\hat{u}_{||} = \frac{\hat{u}_h}{\sqrt{1 - \frac{f^2}{\omega^2}}}, \tag{2.24}$$

$$\hat{u}_{\perp} = \frac{\hat{u}_h}{\sqrt{\frac{\omega^2}{f^2} - 1}}. \tag{2.25}$$

The wind component perpendicular to the wave vector is 90° out of phase with the parallel wind component. The ratio of the two wind components is:

$$\frac{\hat{u}_{\perp}}{\hat{u}_{||}} = \frac{f}{\omega}. \tag{2.26}$$

These equations relating perturbation amplitudes of different variables with each other are called polarisation relations.

2.3 Wave propagation

The propagation of a gravity wave can be approximated with ray theory, also called WKB theory (after Wentzel, Kramers and Brillouin who developed this method for quantum mechanics). In this theory, wave packets are treated as particles moving along rays. The main assumption is, that the background state varies slowly in time and space, compared to the faster movements of the wave, described by the wave vector $\boldsymbol{k}$ and the wave frequency ω. Thus, changes in wave vector and wave frequency also occur slowly and the path of a wave can be approximated by propagating a wave packet in small steps according to the ground-based group-velocity $\boldsymbol{c}_{g,\,gb}$:

$$\frac{d\boldsymbol{x}}{dt} = \boldsymbol{c}_{g,\,gb} = \boldsymbol{c}_g + \bar{\boldsymbol{u}} = \frac{N^2\sqrt{k^2+l^2}}{\omega m^3} \begin{pmatrix} \frac{mk}{\sqrt{k^2+l^2}} \\ \frac{ml}{\sqrt{k^2+l^2}} \\ -\sqrt{k^2+l^2} \end{pmatrix} + \bar{\boldsymbol{u}}. \tag{2.27}$$

Waves with long vertical and short horizontal wavelengths (small m and large $\sqrt{k^2+l^2}$) in general propagate faster than waves with short vertical and long horizontal wavelengths. Further, waves with large vertical wavelength (small m) have a much larger vertical than horizontal group velocity.

The energy which is transported through space is given by the energy of the harmonic oscillator. The kinetic energy is defined as

$$E_k = \frac{1}{2}\rho|\boldsymbol{u}'|^2 = \frac{1}{2}\rho(u_{||}'^2 + u_{\perp}'^2 + w'^2), \tag{2.28}$$

the potential energy as

$$E_p = \frac{1}{2}\rho N^2 \xi'^2. \tag{2.29}$$

The total energy, which is transported by the wave, is given by the sum of the time and space averaged potential and kinetic energy[2]. Thus, a wave packet transports the total energy of

$$\overline{E} = \frac{1}{2}\rho\overline{(u_{||}'^2 + u_{\perp}'^2 + w'^2 + N^2\xi^2)} = \frac{1}{4}\rho(\hat{u}_{||}^2 + \hat{u}_{\perp}^2 + \hat{w}^2 + N^2\hat{\xi}^2). \tag{2.30}$$

Applying the polarisation relations (Section 2.2) leads to

$$\overline{E} = \frac{1}{2}\rho\left(\frac{\hat{T}}{T}\right)^2\left(\frac{g}{N}\right)^2\frac{\omega^2}{\omega^2 - f^2}. \tag{2.31}$$

In sheared flows, the wave energy may change due to a change in the intrinsic wave parameters. The wave action density $A \equiv \frac{\overline{E}}{\omega}$, in contrast, is conserved along the wave path (Bretherton, 1969):

$$\frac{\partial}{\partial t}A + \boldsymbol{\nabla}\boldsymbol{c}_{g,gb}A = \frac{\partial}{\partial t}A + \boldsymbol{\nabla}\bar{\boldsymbol{u}}A + \boldsymbol{\nabla}\boldsymbol{c}_g A = 0. \tag{2.32}$$

[2] The average over one wavelength and wave period of a sine or cosine function is given by $\overline{\cos(\boldsymbol{kx}-\omega t)} = \overline{\sin(\boldsymbol{kx}-\omega t)} = \frac{1}{2}$.

Alternatively, one can also define the invariant pseudo-momentum $\boldsymbol{M} \equiv \frac{\overline{E}\boldsymbol{k}}{\omega}$, which is proportional to the wave action density A (Scinocca and Shepherd, 1992). Gradients of its flux indicate where a gravity wave exchanges drag with the background flow. Especially, the vertical flux of horizontal pseudo-momentum (GWMF)

$$\boldsymbol{F}_{M,z} = c_{g,z}\frac{\overline{E}}{\omega}\boldsymbol{k}_h = \frac{1}{2}\rho\left(\frac{g}{N}\right)^2\frac{(k,l)}{m}\left(\frac{\hat{T}}{\bar{T}}\right)^2 \tag{2.33}$$

is used as a diagnostic for the sources and sinks of gravity waves (Fritts and Alexander, 2003; Ern et al., 2004).

In the following, the simple case of a time invariant atmosphere with a one-dimensional background wind in x-direction $\bar{\boldsymbol{u}} = (U_0, 0, 0)$ is used to discuss how a change in the atmospheric state (N^2 or ρ) influences the wave amplitude. Without loss of generality, the coordinate system is chosen in a way that the horizontal wave vector is oriented along the x-axis ($\boldsymbol{k} = (k, 0, m)$). In this case the wave action conservation (Equation 2.32) simplifies to

$$\frac{\partial}{\partial x}(U_0 + c_{g,x})A + \frac{\partial}{\partial z}c_{g,z}A = 0. \tag{2.34}$$

Assuming that the wave packet does not substantially spread in the horizontal direction during its vertical propagation through the atmosphere leads to

$$\frac{\partial}{\partial z}c_{g,z}A = 0 \quad \Longleftrightarrow \quad c_{g,z}A = \frac{1}{2}\rho\left(\frac{g}{N}\right)^2\frac{1}{m}\left(\frac{\hat{T}}{\bar{T}}\right)^2 = \frac{1}{2}\rho N^2\frac{1}{m}\hat{\xi}^2 = \text{constant}. \tag{2.35}$$

Due to the vertically decreasing density ρ in the atmosphere, the gravity wave amplitudes $\hat{T}$ and $\hat{\xi}$ increase with altitude. Furthermore, if the vertical wavelength stays constant, the gravity wave temperature amplitude $\hat{T}$ increases with increasing N, the vertical displacement amplitude $\hat{\xi}$ decreases.

This thesis uses the Gravity wave Regional Or Global RAy Tracer (GROGRAT; Marks and Eckermann, 1995; Eckermann and Marks, 1997), which is a numerical implementation of ray theory written. GROGRAT implemented as first gravity-wave ray tracer the full dispersion relation (Equation 2.8). Thus, gravity waves of all frequencies, including non-hydrostatic gravity waves as well as gravity waves with frequencies close to the Coriolis frequency f, can be propagated through a spatially slowly varying background atmosphere (Marks and Eckermann, 1995). A second version of GROGRAT (Eckermann and Marks, 1997), further implemented a not only spatially but also temporally varying background.

The differential equations

$$\frac{dx_i}{dt} = \frac{\partial \omega}{\partial k_i} \quad \text{and} \quad \frac{dk_i}{dt} = \frac{\partial \omega}{\partial x_i} \quad x_i \in (x, y, z), \quad k_i \in (k, l, m) \tag{2.36}$$

are solved for multiple time steps using Runge-Kutta methods. For each time step, the wave action conservation law (Equation 2.32) and the full dispersion relation (Equation 2.8) are applied to calculated changes in the wave amplitude. Wave dissipation and damping ($\frac{\partial}{\partial t} A \neq 0$) are accounted for in GROGRAT by including turbulent (Pitteway and Hines, 1963) and radiative (Zhu, 1994) damping schemes and saturation (Fritts and Rastogi, 1985).

GROGRAT requires as input a 4-D atmospheric background field and a gravity wave launch distribution including starting location (longitude, latitude, altitude), horizontal wave numbers, wave amplitude and ground-based frequency. The 4-D atmospheric background fields used for the calculations in this thesis are constructed from 6-hourly ECMWF analysis fields (Chapter 3.5) using a scale separation method (Chapter 4.1). To get gravity wave launch parameters, the results of sinusoidal fits (Chapter 4.2) of the 3-D GLORIA measurements (wave amplitude and wave vector) are converted to the requested input parameters (horizontal wave numbers, wave amplitude and ground-based frequency) using the full dispersion relation (Equation 2.8) and the 4-D atmospheric background fields.

2.4 Sources

2.4.1 Orography

Orography is one of the major sources of gravity waves. The mechanism by which orography excites gravity waves is discussed here using a simple 2-D case taken from Sutherland (2010). A uniformly stratified fluid is moving with a constant horizontal background wind speed $\bar{\boldsymbol{u}}(x,z) = (U_0, 0)$ over periodic low-amplitude sinusoidal mountains (Figure 2.2). The height of the mountains is given by

$$h(x) = \hat{h}\cos(k_0 x). \tag{2.37}$$

For an observer moving with the background flow, for example an air parcel or a balloon, the mountains seem to move at speed $-\bar{\boldsymbol{u}} = -(U_0, 0)$. An air parcel at the surface is forced upward and downward following the terrain height. Thus, its vertical displacement $\xi'(\boldsymbol{x}, t)$ at place $\boldsymbol{x} = (x, 0)$ and time t can be inferred from the terrain height $h(x)$:

$$\begin{aligned}\xi'(\boldsymbol{x}, t) &= h(x + U_0 t) = \hat{h}\cos(k_0(x + U_0 t)) \\ &= \hat{\xi}\cos(-\mathrm{sgn}(U_0)k_0 x - |U_0|k_0 t) = \hat{\xi}\cos(kx - \omega t),\end{aligned} \tag{2.38}$$

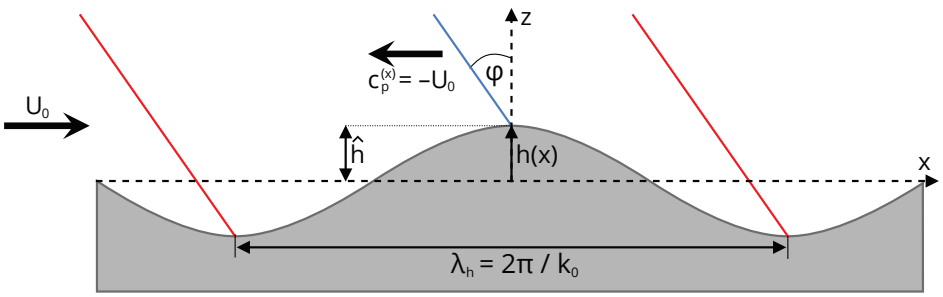

Figure 2.2: Sketch of a gravity wave excited at a sinusoidal mountain (shaded area). A detailed description can be found in the text. Adapted from Figure 5.12 of Sutherland (2010).

with displacement amplitude $\hat{\xi}$, horizontal wave number k, and intrinsic frequency ω. Requesting ω to be positive and using the axis symmetry of the cosine function leads to $\omega = k_0|U_0|$ and $k = -\mathrm{sgn}(U_0)k_0$. It was discussed before (Section 2.1), that the intrinsic frequency of gravity waves is limited to the range $f < \omega \leq N$. Thus, the required wind speed for the excitation of gravity waves at a certain wave number k_0 (determined by the orography) is limited by the Coriolis frequency $f > 0$ and the buoyancy frequency N:

$$\frac{f}{k_0} < |U_0| \leq \frac{N}{k_0}. \tag{2.39}$$

Assuming that the wave motion continues to upper layers $\boldsymbol{x} = (x, z)$, the wave equation can be extended to

$$\xi'(\boldsymbol{x}, t) = \hat{\xi}\cos(kx + mz - \omega t) = \hat{\xi}\cos(\boldsymbol{x}\boldsymbol{k} - \omega t), \tag{2.40}$$

with wave vector $\boldsymbol{k} = (k, m)$. The intrinsic frequency ω of a plane wave in a uniformly-stratified fluid is related to the wave vector $\boldsymbol{k} = (k, m)$ via the dispersion relation (Section 2.1):

$$\omega^2 = \frac{k^2N^2}{m^2} + f^2. \tag{2.41}$$

Solving the dispersion relation (Equation 2.41) for the vertical wave number m gives:

$$m^2 = \frac{k^2N^2}{\omega^2 - f^2} = \frac{k_0^2N^2}{U_0^2k_0^2 - f^2} = \frac{N^2k_0^2}{f^2}\left(\frac{1}{\frac{U_0^2k_0^2}{f^2} - 1}\right) = \frac{N^2k_0^2}{f^2}\left(\frac{1}{R_0^2 - 1}\right). \tag{2.42}$$

If the Rossby number $R_0 = \frac{k_0|U_0|}{f}$ is larger than 1, the vertical wave number m is a real number and vertically propagating gravity waves are excited. A small Rossby number ($R_0 \ll 1$) indicates a flow in geostrophic balance. In this case no gravity waves are excited.

Wave crest and troughs with constant phase move at intrinsic phase velocity

$$\boldsymbol{c}_p \equiv \frac{\omega \boldsymbol{k}}{|\boldsymbol{k}|^2} = \frac{\omega}{k^2+m^2}\begin{pmatrix} k \\ m \end{pmatrix}. \tag{2.43}$$

Wave energy is transported with the intrinsic group velocity

$$\boldsymbol{c}_g \equiv \boldsymbol{\nabla}_k \omega = \frac{N^2 k}{\omega m^3}\begin{pmatrix} m \\ -k \end{pmatrix}. \tag{2.44}$$

To transport the energy away from the mountains, the vertical component of the group velocity $c_{g,z} = -\frac{N^2k^2}{\omega m^3}$ has to be positive and, hence, m has to be negative.

When observing this wave from the stationary reference frame of the mountains, the wave crest move with ground-based phase velocity

$$\boldsymbol{c}_{p,\,gb} \equiv \frac{\Omega \boldsymbol{k}}{|\boldsymbol{k}|^2} = (\omega + \boldsymbol{u}\cdot\boldsymbol{k})\frac{\boldsymbol{k}}{|\boldsymbol{k}|^2} = (k|U_0| - \mathrm{sgn}(U_0)k_0U_0)\frac{\boldsymbol{k}}{|\boldsymbol{k}|^2} = 0. \tag{2.45}$$

Thus, the ground-based frequency $\Omega = \omega + \boldsymbol{u}\cdot\boldsymbol{k} = 0$ and the wave is stationary in time. An observer on the ground, would see the stationary vertical displacement field

$$\xi'(x,z) = h_0 \cos\left(-\mathrm{sgn}(U_0)k_0\, x - \sqrt{\frac{k_0^2N^2}{U_0^2k_0^2 - f^2}}\, z\right). \tag{2.46}$$

The ground-based group velocity of such a stationary wave is

$$\boldsymbol{c}_{g,\,gb} = \boldsymbol{c}_g + \bar{\boldsymbol{u}} = \frac{N^2k}{\omega m^3}\begin{pmatrix} m \\ -k \end{pmatrix} + \begin{pmatrix} U_0 \\ 0 \end{pmatrix} = \frac{U_0^2k_0^2 - f^2}{k_0^2U_0^2}\begin{pmatrix} -U_0 \\ \frac{|U_0|}{N}\sqrt{U_0^2k_0^2 - f^2} \end{pmatrix} + \begin{pmatrix} U_0 \\ 0 \end{pmatrix}. \tag{2.47}$$

For waves with intrinsic frequency $\omega = k_0|U_0| \gg f$, the ground-based

group velocity is vertical:

$$\boldsymbol{c}_{g,gb} = \boldsymbol{c}_g + \bar{\boldsymbol{u}} \approx \begin{pmatrix} -U_0 \\ \frac{U_0^2 k_0}{N} \end{pmatrix} + \begin{pmatrix} U_0 \\ 0 \end{pmatrix} = \begin{pmatrix} 0 \\ \frac{U_0^2 k_0}{N} \end{pmatrix}. \tag{2.48}$$

This theory can straightforwardly be expanded to localized mountains by approximating the shape of the mountains through

$$h(x) = \int_{-\infty}^{\infty} \hat{h}(k) e^{ikx} dk \tag{2.49}$$

where

$$\hat{h}(k) = \frac{1}{2\pi} \int_{-\infty}^{\infty} h(x) e^{ikx} dx, \tag{2.50}$$

is the Fourier transform of the mountain. The generated disturbance is then a superposition of waves with respective horizontal wave number and amplitude, k and $\hat{h}(k)$:

$$\xi(x,z) = \int_{-\infty}^{\infty} \hat{h}(k) e^{ikx + im(U_0,k)z} dk. \tag{2.51}$$

Using a double Fourier transform, this can even be expanded to mountains varying in both horizontal directions:

$$h(x,y) = \int_{-\infty}^{\infty} \int_{-\infty}^{\infty} \hat{h}(k,l) e^{ikx+ily} dk dl. \tag{2.52}$$

The corresponding vertical displacement field above these three dimensional mountains is then

$$\xi(x,y,z) = \int_{-\infty}^{\infty} \int_{-\infty}^{\infty} \hat{h}(k,l) e^{ikx+ily+im(U_0,k,l)z} dk dl. \tag{2.53}$$

In the following, two cases of 3-D mountains, a mountain ridge and a

single mountain peak, are discussed in more detail. The orientation of the phase fronts of a gravity wave generated by a 3-D mountain ridge is independent of the wind direction: The phase fronts are always parallel to the mountain ridge, meaning that the horizontal wave vector is always perpendicular to the ridge. This originates in the fact, that only the part of the wind perpendicular to the mountain ridge $U_{0,\perp}$ is responsible for generating gravity waves (e.g. Bacmeister et al., 1994). The horizontal wavelength $\lambda_h = \frac{2\pi}{k_0}$ of such gravity waves is given by double the width of the mountain ridge at half its height (Jiang et al., 2002). If the mountains consist of multiple ridges with different half-height widths, multiple gravity waves with different horizontal wavelengths are generated. The vertical wave numbers $m = \frac{2\pi}{\lambda_z}$ of the generated gravity waves can be calculated following Equation 2.42:

$$m = \frac{k_0 N}{\sqrt{U_{0,\perp}^2 k_0^2 - f^2}}. \tag{2.54}$$

The intrinsic phase speed and intrinsic group velocity are pointing against the exciting wind $U_{0,\perp}$. Due to the additional wind component parallel to the mountain ridge ($U_{0,||}$), the ground-based phase and group velocities in horizontal direction are not zero any more. Instead they have an additional component in the direction of $U_{0,||}$. The propagation of the wave can be imagined like the movement of a swimmer in an ocean current: The swimmer moves at a constant speed in one direction (intrinsic group velocity). A background current with exactly the same velocity as the swimmer, but oriented in the opposite direction, ($U_{0,\perp}$) keeps the swimmer at the same place. If a second current ($U_{0,||}$) is additionally involved in the situation, the swimmer will drift away with exactly the speed of this second current. Thus, in the case of $\omega \gg f$, the ground-based group velocity can be given by $\boldsymbol{c}_{g,\,gb} = (0, U_{0,||}, \frac{k_0 U_{0,\perp}^2}{N})$, if the x-axis is chosen to be oriented perpendicular to the mountain ridge.

Mountains do not always form mountain ridges. Instead, they also appear as single mountains, for example in the form of small islands. In this case, the generated gravity waves have more complex structure.

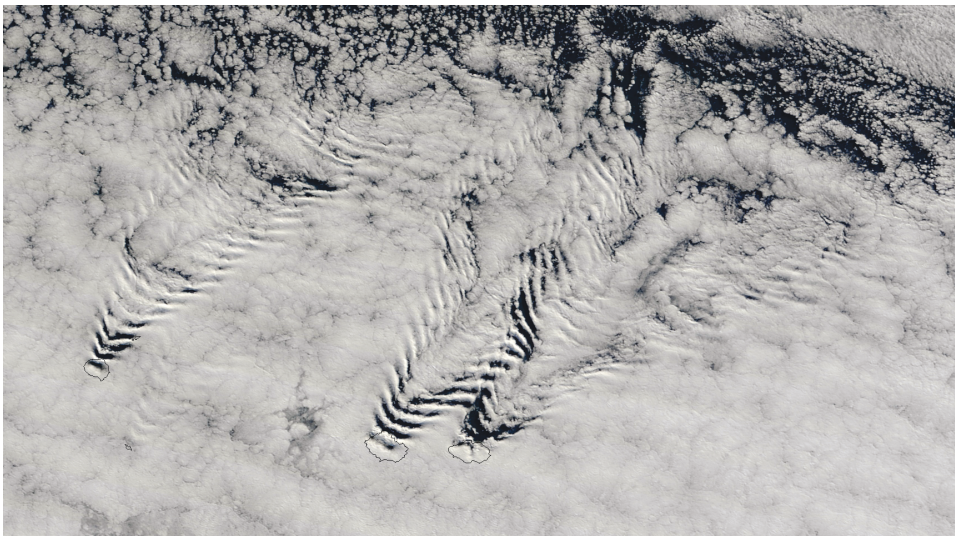

Figure 2.3: Satellite image of cloud patterns generated by gravity waves behind the Crozet Islands on 9 April 2014. Picture courtesy by Jeff Schmaltz, LANCE/EOSDOS MODIS Rapid Response Team at NASA GSFC.

Figure 2.3 shows a cloud pattern generated by gravity waves stemming from small islands. The phase fronts form a diverging wake of waves, meaning the waves are propagating away from the source on the flanks of a v-shape on the leeward[3] side of the mountain. A detailed discussion of the theory of gravity waves generated by single mountains would exceed the scope of this thesis. Details can be found for example in the textbooks by Sutherland (2010) or Nappo (2012).

Islands, like for example Iceland, which have both a main mountain ridge but also many single mountain peaks (volcanoes), will generate very complex wave patterns including both, the phase fronts parallel to the main mountain ridge, as well as the v-shaped phase structures in the downwind direction.

[3] Leeward is the downwind direction.

2.4.2 Non-orographic sources

Even though single gravity wave events excited by orography often have higher energies than those excited by other sources, the globally integrated contribution of non-orographic sources can have a comparable magnitude (Fritts and Nastrom, 1992; Hertzog et al., 2008). In the tropics, convection is the most important non-orographic gravity wave source, while in the mid-latitudes, jets and fronts become more important (Fritts and Alexander, 2003).

2.4.2.1 Convection

Due to the high intermittency of convection and the oblique propagation of the convectively generated waves, it is often difficult to directly link observed convective gravity waves to their source (Preusse et al., 2001; Fritts and Alexander, 2003; Kalisch et al., 2016; Trinh et al., 2016). Nevertheless, there are multiple observations which show a close correspondence between gravity waves and deep convective clouds (Sato et al., 1995; Dewan et al., 1998; McLandress et al., 2000; Alexander et al., 2000). In contrast to mountain waves, convective gravity waves are not characterized by a single characteristic phase speed or frequency. Instead, they are generated throughout the full spectrum of phase speeds, wave frequencies, and horizontal and vertical scales. The exact generation of gravity waves by convection is not yet fully understood. However, three simplified generation mechanisms have been proposed so far: (1) pure thermal forcing, (2) a mechanical oscillator effect, and (3) a transient mountain effect.

Pure thermal forcing: Within convective cells, updrafts and downdrafts form periodically and force air parcels to oscillate. At the top of the convective cell, these oscillations interfere with the stable stratification above and create vertically propagating gravity waves. The strength-/extent of these updrafts and downdrafts is related to the latent heat and, thus, the heating depth. Salby and Garcia (1987) showed that the vertical wavelength of the generated gravity waves is twice the heating

depth. Due to the doubling of the buoyancy frequency at the tropopause, the waves get refracted and a decrease of the vertical wavelength by a factor of 2 is observed. Thus, the gravity waves excited by pure thermal forcing have a vertical wavelength of one tropospheric heating depth in the stratosphere. The intrinsic frequencies of these gravity waves are determined by the time scales of the heating processes.

Mechanical oscillator effect: Within the updraft, an air parcel at some point encounters its level of neutral buoyancy, above which it gets decelerated. The air parcel starts to oscillate vertically ($m = 0$) around this level, which is usually located in the upper troposphere (Fovell et al., 1992). The oscillation frequency is given by the tropospheric buoyancy frequency N_t. The horizontal scales of these gravity waves are determined by the width of the convective updraft (Lane et al., 2001). The doubling of the buoyancy frequency at the tropopause leads to wave refraction and introduces a tilt of the phase fronts in the stratosphere:

$$\frac{k^2}{m^2 + k^2} = \frac{\omega^2}{N^2} = \frac{N_t^2}{N^2} \approx \frac{1}{4}. \tag{2.55}$$

In the horizontal, the phase fronts of waves generated by the mechanical oscillator effect are in general concentric rings around the convection cell propagating away. If the convection cell is moving with a horizontal background wind $\bar{\boldsymbol{u}}$, only gravity waves propagating against this background wind remain. Lane et al. (2001) found, that the gravity waves generated by the mechanical oscillator effect have 10-times higher momentum fluxes than those generated by pure thermal forcing.

Transient mountain effect: Another possible generation mechanism of convective gravity waves is called transient mountain effect. For the background wind flow, the convective updrafts appear as obstacles (mountains) and gravity waves are generated by the same mechanisms and follow the same equations as the waves described in Section 2.4.1. The only difference to the simple mountain wave theory is, that these convective obstacles are not stationary in time. Hence, the ground-based phase speed of the generated gravity waves is not zero, but equal to the speed at which the convective towers move horizontally.

Simulation studies show that the importance of these generation mechanisms strongly depends on the background conditions: In conditions with very weak flow relative to the storm, gravity waves of significant strength are excited. This has to be attributed to the pure thermal forcing or mechanical oscillator effect (Fovell et al., 1992; Lane et al., 2001). However, in strong wind shear, the generated gravity waves have higher amplitudes than expected for pure thermal forcing or mechanical oscillation. These waves are most likely generated by the transient mountain effect (Clark et al., 1986).

2.4.2.2 Jets and fronts

The excitation of gravity waves in the vicinity of jets can often be described by geostrophic adjustment also called spontaneous adjustment emission (Fritts and Alexander, 2003; Plougonven et al., 2013). In this theory, the unbalanced flow tries to restore balance through radiating away energy in form of gravity waves. The causes for these imbalances are various and include, for example, the acceleration or deceleration of the flow by cross-stream pressure gradients (Fritts and Luo, 1992; Luo and Fritts, 1993; Guest et al., 2000), the evolution of fronts (frontogenesis) and baroclinic instabilities (O'Sullivan and Dunkerton, 1995; Griffiths and Reeder, 1996; Reeder and Griffiths, 1996), local body forces due to gravity wave dissipation (Zhu and Holton, 1987; Vadas and Fritts, 2001), and the break down of a mixing layer due to shear instabilities (e.g. Medvedev and Gavrilov, 1995; Bühler, 1999).

Even though the cause of imbalance is not very important, for the gravity waves emitted while restoring balance, the spatial and temporal characteristics of the imbalance have a direct effect on the emitted gravity wave spectrum. The longer the forcing on the flow persists, the smaller is the frequency of the waves. Typical periods of jet generated gravity waves are between 1 h and the inertial period $1/f$. The wavelengths of these gravity waves are in general about twice the extent of the imbalance and on the order of a few kilometres in the vertical and 10-100 times larger in the horizontal. gravity waves excited by spon-

taneous adjustment propagate in general both upward and downward away from the source. Thus, the sources can often be found in measurements where fish-bone patterns are present in vertical cross sections (Vadas et al., 2018).

Gravity waves are also frequently observed in jet exit regions. These regions are characterized by a widening of the stream lines of a jet. A simple model of such a jet exit region is a dipole consisting of a cyclone and an anticyclone travelling together at slow speed (Cunningham and Keyser, 2000; Snyder et al., 2007). These dipoles can be persistent over many days and emit gravity waves at the front of the dipole throughout the whole period. These gravity waves in general originate from spontaneous adjustment emission within the core of the jet (Snyder et al., 2007; Wang and Zhang, 2010). However, they get trapped by the jet and transported to the jet exit region (Buehler et al., 2005; Viudez, 2008; Wang et al., 2010). The propagation of these waves inside the jet strongly influences the wave structure. Thus, the spatial and temporal properties of the escaping gravity waves are mainly determined by the background flow and not by the original source of the waves (Snyder et al., 2009; Wang and Zhang, 2010; Wang et al., 2010). In contrast, the amplitudes of these gravity waves are mainly determined by the original sources (Wang and Zhang, 2007; Lin and Zhang, 2008; Wang and Zhang, 2010).

3 Data acquisition

This thesis uses measurement and model data from various sources. The methods used for data acquisition are described in this chapter. Most measurement data originate from an aircraft measurement campaign called PGGS (Section 3.1), which took place from December 2015 to March 2016. The main scientific goals of this campaign and the scientific payload on board of the German High Altitude and Long Range Research Aircraft (HALO) are summarized. Section 3.2 follows with a detailed description of the measurement principle of the Gimballed Limb Observer for Radiance Imaging of the Atmosphere (GLORIA). Flight planning methods needed to achieve the best measurement results with GLORIA are presented in Section 3.3. Additional to the airborne measurements, data from the spaceborne Atmospheric Infrared Sounder (AIRS; Section 3.4) along with model data from the European Centre for Medium-Range Weather Forecasts (ECMWF; Section 3.5) are used to accomplish the scientific findings derived in the following chapters.

3.1 Aircraft measurement campaign

From December 2015 to March 2016 an extensive aircraft measurement campaign called PGGS took place with ground bases in Oberpfaffenhofen, Germany, and Kiruna, Sweden. PGGS actually was a conglomerate of several campaigns with different scientific targets:

- **P**OLSTRACC: observe the polar stratosphere in a changing climate,
- **G**W-LCYCLE: study the full life cycle of gravity waves,

- **G**WEX: demonstrate the use of infrared limb imaging for gravity wave studies,
- **S**ALSA: investigate the seasonality of air mass transport and origin in the lowermost stratosphere.

During the campaign, 21 research flights were performed covering 20° N to 90° N and 80° W to 30° E (Figure 3.1), out of which seven contained measurements of gravity waves. On 12 January 2016, a gravity wave field was sampled above the Italian Apennine Mountains. On 25 January 2016, a gravity wave field above Iceland was probed with a hexagonal flight pattern dedicated to full angle tomography with GLORIA. On 28 January and 29 February, gravity waves above southern and northern Scandinavia were investigated with linear flight patterns. On 2 February 2016, a mountain wave above Svalbard was chosen as one of the scientific goals and encircled with a hexagon. On 6 March and 10 March 2016, gravity waves above the southern tip of Greenland and

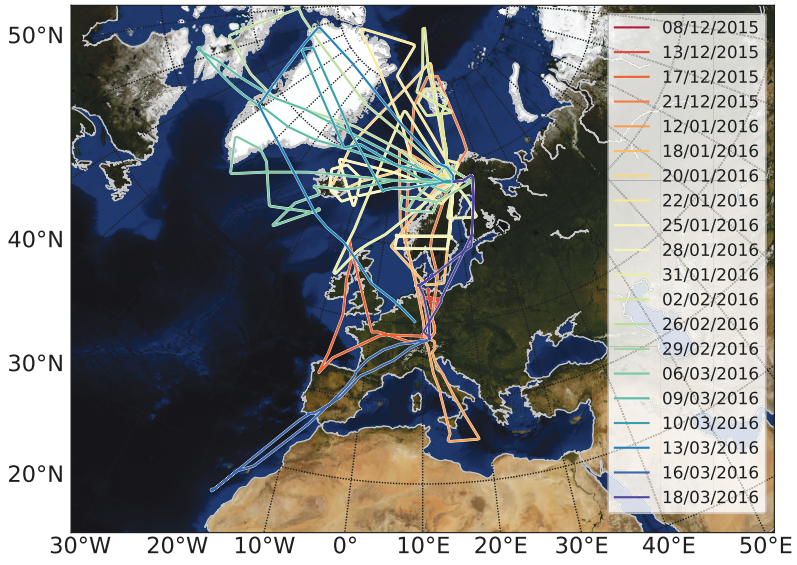

Figure 3.1: All measurement flights performed during PGGS.

above the Greenland plateau were addressed by scientific flights. This thesis will present and analyse GLORIA measurement results from the flights on 25 January 2016 above Iceland (Chapter 6) and on 28 January 2016 above southern Scandinavia (Chapter 7). The scientific targets of all other PGGS flights are listed in Table 3.1. Scientific topics including gravity waves are highlighted in bold.

The carrier used for this campaign was the German High Altitude and Long Range Research Aircraft (HALO; see Figure 1.4). This plane is based on the business jet Gulfstream G550 with modifications that allow the mounting of a wide variety of scientific equipment. The maximum speed of HALO is 940 km h^{-1}, the maximum cruise altitude is 15.5 km, and the maximal flight distance is 12 500 km (DLR, 2018). Due to the weight of the scientific payload, the maximum flight altitude is in general not reached during scientific measurement campaigns. The highest flight altitude during PGGS was 14.9 km. Due to the maximal allowed take-off weight, every scientific instrument decreases the maximum amount of fuel, which HALO can take on a flight. Thus, the maximal flight distance is determined by the weight of the scientific payload and is typically around 9000 km.

The scientific payload of HALO during PGGS encompassed three remote sensing instruments: GLORIA in the belly-pod, the upward looking water vapor, cloud and ozone lidar WALES, and the differential optical absorption spectrometer miniDOAS. In addition, the Basic HALO Measurement and Sensor System (BAHAMAS) measuring temperature, pressure and winds at high precision and high temporal resolution as well as a number of in-situ instruments were part of the payload. The full list of instruments can be found in Table 3.2. This thesis uses data from GLORIA, the BAHAMAS system and the dropsondes. BAHAMAS and the dropsondes are descibed shortly in the following. Section 3.2 gives a detailed description of the GLORIA instrument and the used retrieval methods.

BAHAMAS is part of the extended standard instrumentation on HALO. The main sensors are mounted inside a nose boom which allows for more accurate temperature and wind measurements than possible on standard airplane instrumentation. After post-flight processing, data are

Table 3.1: Scientific targets of the HALO research flights during PGGS.

#	Date	Scientific targets
1	08/12/2015	Operational test flight
2	10/12/2015	Operational test flight
3	13/12/2015	Scientific instrumentation test flight
4	17/12/2015	SALSA: early winter survey
5	21/12/2015	POLSTRACC: early winter survey into polar vortex
6	12/01/2016	Ferry flight to Kiruna: long transect from subtropical air masses to polar vortex core,**tropopause fold above Italy interacting with gravity waves**
7	18/01/2016	POLSTRACC: renitrification and enhanced ClO_x in the polar vortex
8	20/01/2016	POLSTRACC: renitrification, enhanced ClO_x, and very cold temperatures in the polar vortex, polar stratospheric clouds
9	22/01/2016	POLSTRACC: polar stratospheric clouds east of Greenland
10	25/01/2016	GW-LCYCLE/GWEX: **Gravity waves above Iceland**, hexagonal flight pattern
11	28/01/2016	GW-LCYCLE/GWEX: **Transient gravity waves above southern Scandinavia**, coordinated flight with the Falcon research aircraft
12	31/01/2016	POLSTRACC: late January survey into the polar vortex
13	02/02/2016	GW-LCYCLE/GWEX: **Gravity waves above Svalbard**, hexagonal flight pattern POLSTRACC: high latitude survey
14	26/02/2016	POLSTRACC: late February survey at different theta levels to study the chlorine and bromine chemistry inside the polar vortex
15	29/02/2016	POLSCTRACC: the development of a polar low off the Norwegian coast, GW-LCYCLE/GWEX: **gravity waves above northern Scandinavia**
16	06/03/2016	GW-LCYCLE/GWEX: **gravity waves at the south tip of Greenland**, POLSTRACC: high ozone loss and cirrus clouds
17	09/03/2016	POLSTRACC: ozone loss and depleted NO_y
18	10/03/2016	GW-LCYCLE/GWEX: **gravity waves above the Greenland plateau**, SALSA: air masses with high N_2O
19	13/03/2016	Ferry flight to Oberpfaffenhofen: low N_2O over Greenland, high tropopause and high N_2O between Greenland and Great Britain
20	16/03/2016	SALSA: late spring survey
21	18/03/2016	POLSTRACC: evolution of air masses already probed on 13/03/2016, cirrus clouds

provided shortly after flight (1–2 days). The resolution of nominal data is ≈1 Hz, for turbulence studies experimentally higher temporal resolutions are recorded. The temperature measurements of BAHAMAS have an accuracy of 0.5 K and a precision below 0.1 K (Giez, 2012).

Dropsondes are sensors on parachutes released from the aircraft, which send meteorological information to a receiver in the aircraft by telemetry. They register temperature, GPS position information from which horizontal winds are derived, and pressure. A sonde takes approximately 15 min from 14 km to the ground. A temporal sampling of 2 Hz corresponds to a vertical resolution of approximately 20 m (Kaufmann, 2018).

Table 3.2: List of scientific instruments for the aircraft measurement campaign PGGS on board of HALO.

Acronym	Explanation
AENEAS	NO_y measurement
AIMS	Atmospheric Chemical Ionization Mass Spectrometer
BAHAMAS	Basic Halo Measurement and Sensor System
Dropsonde System	Meteorologic data set below HALO
FAIRO	Fast ozone measurement
FISH	Fast In-situ Stratospheric Hygrometer
GhOST	Gaschromatograph for Observation of Startopsheric Tracers
GLORIA	Gimballed Limb Observer for Radiance Imaging of the Atmosphere
HAGAR-V	High Altitude Gas AnalyzeR
HAI	Hygrometer for Atmospheric Investigation
TRIHOP	Three-channel tunable diode laser instrument for atmospheric research
miniDOAS	Differential Optical Absorption Spectroscopy
WALES	Water Vapour Lidar Experment in Space

3.2 Gimballed Limb Observer for Radiance Imaging of the Atmosphere (GLORIA)

3.2.1 Measurement concept

The Gimballed Limb Observer for Radiance Imaging of the Atmosphere (GLORIA) is an infrared limb sounder with a Fourier Transform Spectrometer (FTS) developed for deployment on an aircraft (Friedl-Vallon et al., 2014; Riese et al., 2014). GLORIA combines a classical Michelson interferometer with a 2-D detector array. It measures the infrared radiation in the spectral range from 780 cm^{-1} to 1400 cm^{-1} (Figure 3.2), which is emitted by particles and trace species in the atmosphere. The interferometer spectrally resolves this radiation to reveal characteristic molecular emission bands. The 2-D detector array consists of 256×256 pixels, out of which 48 horizontal $\times$ 128 vertical pixels are used to decrease the read-out time. GLORIA provides more than 6 000 simultaneous limb-views with elevation angles ranging from $-3.3°$ to slightly upwards. Thereby, an altitude range from 4 km up to flight altitude around 15 km is covered. To increase the signal-to-noise ratio, all pixels of one detector-row are co-added to superpixels. Even though this co-adding reduces the horizontal resolution of trace gas and temperature retrievals in flight direction slightly, it improves the measurement quality drastically. Further, one has to keep in mind, that the horizontal resolution across flight direction is much worse than in flight direction, which means the slight reduction in flight direction does not change the information content gained from these measurements. The horizontal point spread function (PSF) of these superpixels is 1.5°, which corresponds to 6.7 km at an altitude of 10 km.

GLORIA's line of sight (LOS) aims towards the horizon - also called limb of the Earth - on the right side of the aircraft. These straight LOSs get a parabolic shape when plotted in a cartesian coordinate system with x-axis following the Earth's surface (Figure 3.3 a). The point of the LOS which is closest to the earth surface is called tangent point. Due to the exponentially declining density of the atmosphere with altitude, most

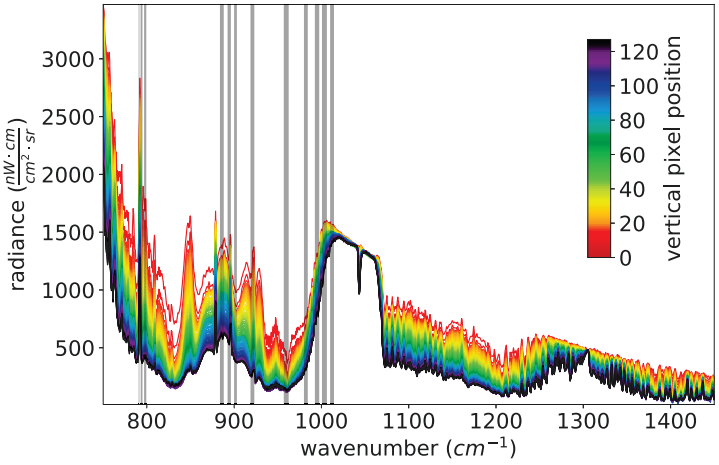

Figure 3.2: Infrared spectra measured by GLORIA on 25 January 2016 at 10:14 UTC. Shown are co-added spectra of the 128 superpixels. The spectral ranges used for the retrievals in this thesis (see Table 3.4) are highlighted in grey.

radiation along the LOS is emitted at lower altitudes and, thus, around this tangent point. Moreover, for geometrical reasons, a comparatively long part of the LOS samples altitudes close to the tangent point, while higher atmospheric layers are passed only briefly. As a consequence, limb sounders are in general more sensitive to changes in the atmosphere around the tangent point. The temperature weighting function in Figure 3.3 b, which is a measure for the amount of measured radiation originating from a certain point in space, demonstrates this nicely. The horizontal resolution of limb sounders along LOS can be calculated from the full width at half maximum (FWHM) of this temperature weighting function. For conventional limb sounders this resolution along LOS is on the order of 200 km to 300 km (Riese, 1994; von Clarmann et al., 2009; Ungermann et al., 2012).

GLORIA is operated in two different modes: The chemistry mode, which has a high spectral sampling of 0.0625 cm^{-1}, and the dynamics mode with a coarser spectral sampling of only 0.625 cm^{-1}. The coarser

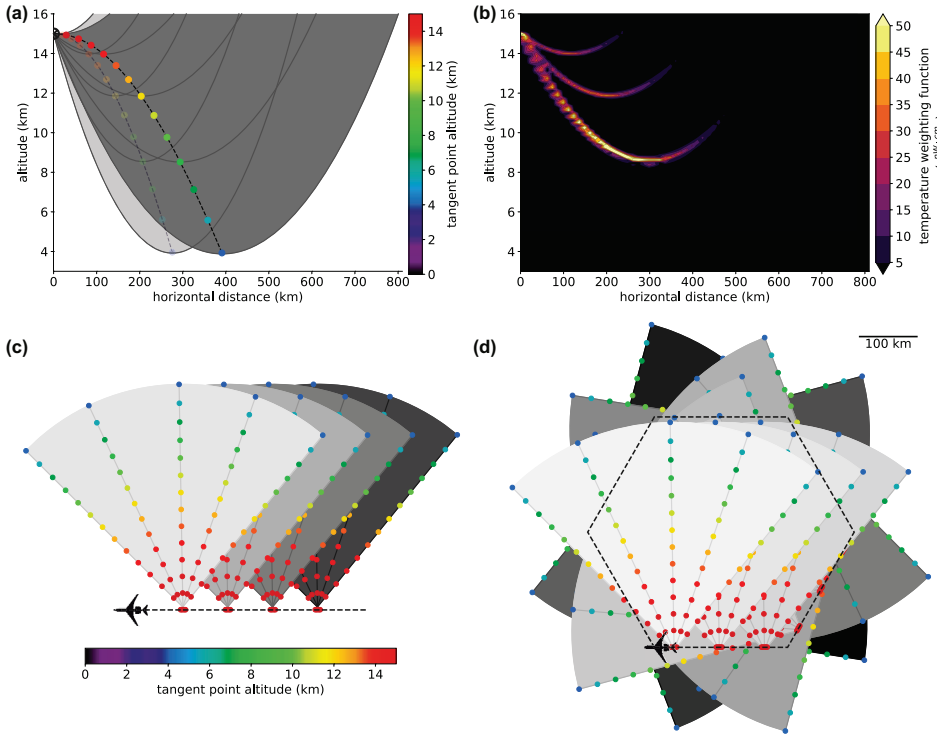

Figure 3.3: In Panel (a) a simple schematic of the limb sounding geometry is given. The airplane is flying orthogonally into the paper plane. Images taken under 90° azimuth cover the dark grey area with LOSs. The respective tangent points (bright coloured dots) increase in distance with decreasing altitude. The tangent points of forward and rearward looking images (light grey and pale coloured dots) are closer to the flight path. The LOS, which are straight lines in reality, have a parabolic shape in this plot due to the transformation into a cartesian coordinate system with x-axis following the earth surface. Panel (b) shows the weighting function along three different LOSs indicating the contribution of the respective part of the atmosphere to the observed signal. In panels (c) and (d) the principles of LAT and FAT with the GLORIA instrument are depicted, respectively. Shown are top views in bird perspective onto the flight path. The dots again indicate the tangent points and are coloured according to their altitude. Each grey sector indicates one horizontal scan from 45° (right forward) to 135° (right backward). The lighter the grey, the later in time are these measurements taken. Figure from Krisch et al. (2018).

spectral sampling leads to a faster interferogram acquisition and accordingly an improved spatial sampling in flight direction (at 10 km altitude 0.45 km instead of 2.25 km). The horizontal resolution in flight direction, is not dominated by the spatial sampling but by the point spread function (PSF) of the detector and is on the order of several kilometres for both measurement modes depending on the tangent-point altitude.

The improved spatial sampling of the dynamics mode is used to scan the atmosphere horizontally in steps of 4° from 45° (right forward) to 135° (right backward) with respect to the aircraft's heading (Figure 3.3 c). In this way, the same volume of air is measured under different angles, which allows for tomographic retrievals (Natterer, 2001). With this concept the horizontal resolution can be improved by up to an order of magnitude. The exact values of the spatial resolutions in all directions, depend on the specific measurement pattern and retrieval set-up and are discussed separately for each presented retrieval in the respective chapters.

Measuring emitted radiation from all 360° around the volume, for instance, by flying a hexagon, is called full angle tomography (FAT, Figure 3.3 d). In contrast to FAT, limited angle tomography (LAT, Figure 3.3 c) does not measure the volume from all sides but only from a limited set of angles. Due to the horizontal scanning capabilities of the GLORIA instrument, this is already possible on a linear flight path. However, LAT inversion problems are in general seriously ill-posed (Natterer, 2001). Well-posed problems in the mathematical term are defined to have a unique and continuous solution (Hadamard, 1902). If a problem does not have a solution or the solution is not unique or not a continuous function of the input parameters, the problem is called ill-posed. Problems with multiple solutions can often be converted to well-posed problems through adding a priori knowledge in form of regularisation terms.

Using FAT allows for the 3-D reconstruction of a cylindrical volume. The diameter of this volume depends on the flight path and is usually on the order of 400 km. The volume which can be reconstructed with LAT is given by the tangent point distribution. Tangent points of forward or backward looking measurements are closer to the flight path then those

with an azimuth angle of 90° (see Figure 3.3 a). At higher altitudes, the tangent points are closer together and thus the horizontal resolution across flight track is higher. At the same time the horizontal extent of the tangent point covered area is smaller at higher altitudes. In the vertical, the volume covered by tangent points has a banana-like shape with increasing distance to the flight path and increasing horizontal extent with decreasing altitude. At 10 km altitude, the horizontal extent of the measurement volume across flight track is on the order of 150 km.

Using LAT, all overlapping measurements of an air parcel are taken less than 15 min apart. In contrast, the acquisition time of the full angle tomogram acquired on the 25 January 2016 above Iceland was 125 min. Thus, LAT is more suitable for measurements of transient gravity waves and gravity waves in a fast changing background wind, whereas for FAT steady gravity waves with a ground-based phase speed of approximately 0 are needed. Further advantages and disadvantages of FAT and LAT for gravity wave measurements are discussed in Chapter 5, where the sensitivity of both measurement methods to gravity waves is studied in detail.

3.2.2 Level 2 processing

In remote sensing, the process of converting raw detector measurements to equitemporally sampled interferograms is called level 0 processing. Level 1 processing transforms these interferograms to calibrated spectra. The derivation of geophysical quantities from these calibrated spectra is called level 2 processing. Level 2 processing is an inverse problem, meaning there is no function directly relating the atmospheric radiation at the place of the instrument with the geophysical quantities. However, a forward model describes which radiation is expected to be measured by the instrument if the atmosphere has a certain temperature and trace gas distribution (Section 3.2.2.1). By iteratively adapting these temperature and trace gas distributions, the simulated measurements can be adjusted until they agree with the real measurements within a certain range of expectation. This process is called inversion or retrieval (Section 3.2.2.2). The retrieval diagnostics describe the influence of dif-

ferent error sources and the retrieval set-up on the retrieved geophysical quantities (Section 3.2.2.3).

3.2.2.1 Forward model and GLORIA measurement simulator (GLSIM)

The forward model $\boldsymbol{F} : \mathbb{R}^n \rightarrow \mathbb{R}^l$ maps a certain atmospheric state $\boldsymbol{a} \in \mathbb{R}^n$ onto a set of radiances $\boldsymbol{F}(\boldsymbol{a}) \in \mathbb{R}^l$ as could be measured by GLORIA. It describes the radiative transfer in the atmosphere, which is determined by emission, absorption and scattering processes. The change of radiation in space at a certain wave number ν can be described by the equation of radiative transfer (e.g. Chandrasekhar, 1960):

$$I(\nu, s) = I(\nu, 0)e^{-\tau(\nu,0,s)} + \int_0^s \mathfrak{J}(\nu, s')e^{-\tau(\nu,s',s)}\kappa(\nu, s')\rho(s')ds', \quad (3.1)$$

where $\mathfrak{J} = \frac{j}{\kappa}$ is the so-called source function, j the emission coefficient, and κ the absorption coefficient. The optical thickness $\tau(\nu, s', s)$ between point s' and s is defined by

$$\tau(\nu, s', s) = \int_{s'}^s \kappa(\nu, s'')\rho(s'')ds''. \quad (3.2)$$

The absorption coefficient κ is a function of trace species, wave number ν, temperature T and pressure p. It can be calculated using characteristic absorption lines tabulated in databases like for example HITRAN (high-resolution transmission molecular absorption database; Rothman et al. (2013)). The optical thickness τ in Equation 3.1 is used to define the transmittance $\mathrm{tr}(\nu, s', s) = e^{-\tau(\nu,s',s)}$.

In local thermodynamic equilibrium and in the absence of scattering, the source function $\mathfrak{J}(\nu, s')$ becomes the Planck function

$$\mathscr{B}(\nu, T(s')) = \frac{2h_p\nu^3}{c^2}\frac{1}{\exp(\frac{h_p\nu}{k_B T(s')}) - 1}, \quad (3.3)$$

with Planck constant h_p, speed of light c, and Boltzmann constant k_B.

To adjust the general equation of radiative transfer (Equation 3.1) to the GLORIA measurement geometry, one has to integrate along LOS from space ($s = \infty$) to the instrument location ($s = 0$). The infrared radiation in space is negligible ($I(s \to \infty) \approx 0$), thus the radiation arriving at the instrument can be calculated as follows:

$$I(\nu) = -\int_0^{\infty} \mathscr{B}(\nu, T(s')) \frac{d\mathrm{tr}(\nu, 0, s')}{ds'} ds'. \tag{3.4}$$

The forward model $\boldsymbol{F}$ does this calculation for a certain set of spectral ranges defined by the retrieval set-up. It takes as input the atmospheric pressure, temperature and trace gas distribution, which determines the Planck function and the transmittance at every point s' in the atmosphere.

The forward model $\boldsymbol{F}$ also includes the spectral resolution of the detector, called instrument line shape (ILS), and the spatial resolution of the detector, called PSF. The PSF is convolved with the radiation coming from all azimuth angles Θ and all elevation angles Φ:

$$\boldsymbol{F}(\boldsymbol{a}) = \int_{-\pi/2}^{\pi/2} \int_0^{2\pi} \mathrm{PSF}(\Theta, \Phi) \sum_{\nu} \mathrm{ILS}(\nu) I(\nu) d\Theta d\Phi \tag{3.5}$$

As GLORIA can measure radiances only with finite precision and accuracy, a measurement error $\boldsymbol{\epsilon} \in \mathbb{R}^l$ is added to get the simulated radiances $\boldsymbol{y} \in \mathbb{R}^l$:

$$\boldsymbol{y} = \boldsymbol{F}(\boldsymbol{a}) + \boldsymbol{\epsilon} \tag{3.6}$$

The radiative transfer modelling for GLORIA is done using the Jülich Rapid Spectral Simulation Code V2 (JURASSIC2) which efficiently handles the large data amounts of imager instruments and tomographic retrievals. It is based on JURASSIC (Hoffmann, 2006), which was previously used as forward model for the evaluation of several satellite- and air-borne remote sensing experiments (e.g. Hoffmann et al., 2008;

Weigel et al., 2010; Ern et al., 2017). It contains several approaches of varying computational complexity and accuracy for computing radiances, but we employ in this work the fast table based approach using the emissivity growth approximation (EGA; e.g. Weinreb and Neuendorffer, 1973; Gordley and Russell, 1981; Riese et al., 1999).

The forward calculation can also be used to generate simulated measurements. This is implemented in the GLORIA measurement simulator (GLSIM), which combines the forward model with the facility to simulate a range of potential flight patterns. Thus, the effectiveness of different measurement geometries can be explored without using costly flight hours and real measurement time.

3.2.2.2 Retrieval

The Jülich Tomographic Library (JUTIL) software package is used for mapping infrared spectra back to geophysical quantities, in our case the retrieved atmospheric state $\boldsymbol{a}_r \in \mathbb{R}^n$. The ill-posed retrieval problem is approximating by a well-posed one using a temperature regularisation. This temperature regularisation is implemented following the scheme introduced by Tikhonov and Arsenin (1977):

$$\begin{aligned} J(\boldsymbol{a}) = &\left(\boldsymbol{F}(\boldsymbol{a}) - \boldsymbol{y}\right)^T \mathbf{S}_\epsilon^{-1} \left(\boldsymbol{F}(\boldsymbol{a}) - \boldsymbol{y}\right) \\ &+ (\boldsymbol{a} - \boldsymbol{a}_a)^T \mathbf{S}_a^{-1} (\boldsymbol{a} - \boldsymbol{a}_a) \rightarrow \min \end{aligned} \tag{3.7}$$

with $\mathbf{S}_\epsilon \in \mathbb{R}^{l \times l}$ the measurement error covariance matrix and $\mathbf{S}_a \in \mathbb{R}^{n \times n}$ the covariance matrix of the atmospheric state vector. The first term of the cost function J is a measure for the agreement between simulated and real measurements. The regularisation term (second part of Equation 3.7) converts the ill-posed problem into a well-posed one and ascertains a physically meaningful solution. The regularisation is based on an a priori covariance matrix $\mathbf{S}_a$:

$$\mathbf{S}_a^{-1} = \frac{w_0}{\sigma^2} |\boldsymbol{a}|^2 + \frac{w_1}{\sigma^2} \left(\left| c_z \frac{\partial}{\partial z} \boldsymbol{a} \right|^2 + \left| c_h \frac{\partial}{\partial x} \boldsymbol{a} \right|^2 + \left| c_h \frac{\partial}{\partial y} \boldsymbol{a} \right|^2 \right). \tag{3.8}$$

Table 3.3: Standard deviations, weighting factors, vertical (c_z), and horizontal (c_h) correlation lengths used for the construction of the covariance matrix $\mathbf{S}_a$ (Equation 3.8).

atmospheric quantity	σ	w_0	w_1	c_z	c_h
temperature	1 K	10^{-3}	10^{-2}	1.0 km	100 km
O_3	141 ppbV	10^{-6}	10^{-5}	8.0 km	6400 km
CCl_4	13 pptV	10^{-5}	10^{-4}	2.0 km	800 km
HNO_3	987 pptV	10^{-7}	10^{-4}	3.2 km	1280 km

The standard deviations σ, weighting factors w_1 and w_2, and the correlations lengths c_z and c_h used for the retrieval are given in Table 3.3. These factors are chosen after several sensitivity test. In the current retrieval version, they cannot be interpreted directly as physically meaningful correlation lengths. A more physical regularisation scheme, which will use correlation lengths estimated from climatological measurements, is currently under development (Krasauskas et al., 2018).

The minimization problem is solved with a truncated conjugate gradient based trust region scheme. More details on the retrieval algorithms used for GLORIA Level 2 processing are described by Ungermann et al. (2015). To decrease the computational effort, only a limited number of spectral lines is used for the retrievals. Conventional infrared temperature retrievals for limb sounding instruments use spectral ranges in the CO_2 Q-branch region at 790.75 cm^{-1} (12.6 µm) (Riese et al., 1997; Ungermann et al., 2010a). The resolution along LOS can be increased by including additional spectral ranges with different emission and absorption characteristics (Ungermann et al., 2011). The retrievals presented in this thesis use the spectral ranges in Table 3.4. The retrievals of the gravity wave sensitivity study (Chapter 5) use only the spectral ranges 1 to 7 in Table 3.4. The retrievals involving actual measurements (Chapter 6 and 7) include the spectral ranges 8 and 9 in Table 3.4 to improve the knowledge about the CCl_4 background radiation in the CO_2 Q-branch region. Furthermore, the spectral ranges 10 to 13 are used additionally to retrieve the trace gas HNO_3, which is mostly used to get

Table 3.4: Spectral ranges used for the GLORIA retrievals presented in this thesis. The last column indicates the retrieved quantity for each spectral range. For the simulation study (Chapter 5.2 and 5.3), the spectral ranges 1 to 7 are used. For the real measurement retrievals (Chapter 5.4), the spectral ranges 8 to 13 are added. The spectral ranges are highlighted in grey in Figure 3.2.

	Spectral range in cm^{-1}			Used for
1	790.625	–	791.250	temperature
2	791.875	–	792.500	temperature
3	956.875	–	962.500	temperature
4	980.000	–	984.375	temperature, O_3
5	992.500	–	997.500	temperature, O_3
6	1000.625	–	1006.250	temperature, O_3
7	1010.000	–	1014.375	temperature, O_3
8	793.125	–	795.000	CCl_4
9	796.875	–	799.375	CCl_4
10	883.750	–	888.125	HNO_3
11	892.500	–	896.250	HNO_3
12	900.000	–	903.125	HNO_3
13	918.750	–	923.125	HNO_3

an accompanying picture of a second stratospheric tracer besides ozone.

To improve the convergence speed and the quality of retrievals, a priori fields are taken from different models. The temperature a priori was constructed from ECMWF operational analyses by applying the scale separation described in Chapter 4.1 and using the background field as a priori. This ensures that any gravity wave signature in the retrieval result does not originate from the a priori field. The pressure field was taken directly from the ECMWF analysis. The a priori fields of several trace gases (CH_4, CO_2, H_2O, O_3, ...) are taken from the Whole Atmosphere Community Climate Model version 4 (WACCM4; Marsh et al., 2013). For the study based on synthetic data in Chapter 5, a climatological field $\boldsymbol{a}_c$ from Remedios et al. (2007) is used as a priori field.

For small perturbations, the forward model can be linearised using a

Taylor expansion (Rodgers, 2000; Ungermann et al., 2010a):

$$\boldsymbol{y} - \boldsymbol{y}_a = \mathbf{F}'(\boldsymbol{a}_a)(\boldsymbol{a} - \boldsymbol{a}_a) + \boldsymbol{\epsilon}. \tag{3.9}$$

$\mathbf{F}'(\boldsymbol{a}_a) = \frac{\partial \boldsymbol{F}}{\partial \boldsymbol{a}}\Big|_{\boldsymbol{a}_a}$ is the Jacobian matrix of the forward model evaluated at $\boldsymbol{a}_a$ and $\boldsymbol{y}_a = \mathbf{F}(\boldsymbol{a}_a)$ are the simulated radiances of the a priori state.

With the retrieval gain matrix $\mathbf{G}(\boldsymbol{a}_a) = (\mathbf{F}'(\boldsymbol{a}_a)^T \mathbf{S}_\epsilon^{-1} \mathbf{F}'(\boldsymbol{a}_a) + \mathbf{S}_a^{-1})^{-1} \mathbf{F}'(\boldsymbol{a}_a)^T \mathbf{S}_\epsilon^{-1}$ and the Jacobian matrix $\mathbf{F}'(\boldsymbol{a}_a)$, the averaging kernel matrix $\mathbf{A}(\boldsymbol{a}_a) = \mathbf{G}(\boldsymbol{a}_a)\mathbf{F}'(\boldsymbol{a}_a)$ can be calculated. Using the averaging kernel and the gain matrix, synthetic perturbations of the atmospheric state $\Delta\boldsymbol{a}_s$, such as gravity waves, as well as synthetic measurement errors $\boldsymbol{\epsilon}_s$ can directly be transferred into retrieved atmospheric perturbations $\Delta\boldsymbol{a}_r$:

$$\mathbf{G}(\boldsymbol{a}_a)(\boldsymbol{y} - \boldsymbol{y}_a) = \mathbf{G}(\boldsymbol{a}_a)(\mathbf{F}'(\boldsymbol{a}_a)(\boldsymbol{a} - \boldsymbol{a}_a) + \boldsymbol{\epsilon}_s) \tag{3.10}$$

$$\Delta\boldsymbol{a}_r = \mathbf{A}(\boldsymbol{a}_a)\Delta\boldsymbol{a}_s + \mathbf{G}(\boldsymbol{a}_a)\boldsymbol{\epsilon}_s. \tag{3.11}$$

This linearisation is used for the synthetic sensitivity study presented in Chapter 5 and for the error analysis (detailed description in Chapter 3.2.2.3)). For the wave amplitudes used for the sensitivity study, the noise term $\mathbf{G}(\boldsymbol{a}_a)\boldsymbol{\epsilon}$ is negligible with respect to the other terms and, thus, is disregarded. For selected cases, the linear approximation has been validated by a comparison of linear and non-linear retrieval results.

3.2.2.3 Diagnostics

As described in Chapter 3.2.2.2, a linearisation of the retrieval can be used to calculate the influence of arbitrary error sources. Covariance matrices describing different systematic error sources are assembled using an auto-regressive approach with reasonable standard deviations and correlation lengths (Tarantola, 2004). The standard deviations and correlation lengths used for the different systematic errors are summarized in Table 3.5. All these systematic errors are combined under the label accuracy. It is assumed that gain and offset errors are spatially uncorrelated, but spectrally fully correlated (in the absence of a better characterization, this provides a worse error estimate than assuming no spectral

Table 3.5: Systematic error sources included in the retrieval diagnostics with respective standard deviations and correlation lengths.

Error source	standard deviation	correlation lengths
pointing errors	0.05°	vertical: ∞, temporal: 0
misrepresented background gases	from Remedios et al. (2007)	
uncertainties in spectral line characterization	5 %	temporal: ∞
calibration errors gain	1 %	temporal: ∞
calibration errors offset	5 nW	temporal: 0

correlation). The effects of calibration errors on the GLORIA retrieval are discussed in detail in Appendix B.

The covariance matrix for measurement noise is taken from theoretical estimates given by Friedl-Vallon et al. (2014) that agree well with estimates derived from real measurements (Kleinert et al., 2014). Error estimates calculated from this measurement noise will be named precision error in the following. The resolution describes which area around a measurement point influences its value. However, from a numerical perspective, the influence as determined by the averaging kernel matrix becomes never exactly zero simply due to numerical inaccuracies in determining the matrix. Atmospheric values closer to a measurement point in general have higher influence than values far away. One way to determine the influence of the atmosphere around a measurement point is to look at the averaging kernel matrix **A**. The resolution of 1-D remote sensing retrievals at a certain point in the atmosphere can be defined as the full-width-at-half-maximum (FWHM) of the respective averaging kernel (Rodgers, 2000; von Clarmann et al., 2009). In previous work (Ungermann et al., 2011), the vertical resolution of tomographic GLORIA measurements was determined from the FWHM of the centre row of the averaging kernel. The horizontal resolution was derived from a sphere containing all points of the averaging kernel **A** larger than half the maximum. The averaging kernels of LAT retrievals have a very complex shape and are in general not symmetric in the horizontal. Thus,

the resolutions of the 3-D retrievals presented in this thesis are defined by the lengths of the main axes of a 3-D ellipsoid containing all points of the averaging kernel **A** larger than half the maximum. This is especially useful for determining the spatial resolutions of more ill-posed LAT retrievals than the previously used circular spheres.

3.3 Scientific flight planning

To gain the best possible scientific results, the measurement flights have to be specifically tailored to the respective atmospheric situations. This is done with the help of the Python-based Mission Support System (MSS). MSS is a web-service based tool for scientific flight planning initially developed by Rautenhaus et al. (2012). In preparation for the measurement campaign in Winter 2015/2016, this tool entered the public domain and became an open source program. It consists of two major components: First, a web server providing an Open Geospatial Consortium Web Map Service (WMS) with some additional proprietary features enabling, for example, also vertical cross-sections needed for scientific flight planning; Second, a cross-platform Python client for actual flight planning, which may access any WMS server. The WMS server is able to provide horizontal and vertical cuts through any regularly gridded model data following the NetCDF Climate and Forecast metadata standards. To support the scientific study of gravity waves, plots of new data products such as gravity wave perturbations and momentum flux data were included.

The front end was drastically enhanced in a joint effort before and during the PGGS campaign by implementing several features required especially for the planning of tomographic flights with GLORIA (Figure 3.4). For example, hexagonal flight patterns can now easily be added through providing a centre point, a radius, and a rotation angle. After creation, single points of the hexagon can be shifted separately or deleted to precisely adjust the flight path to the requirements. Another option implemented to adapt the flight path accurately to the GLORIA viewing geometry is the display of GLORIA tangent points at different altitudes.

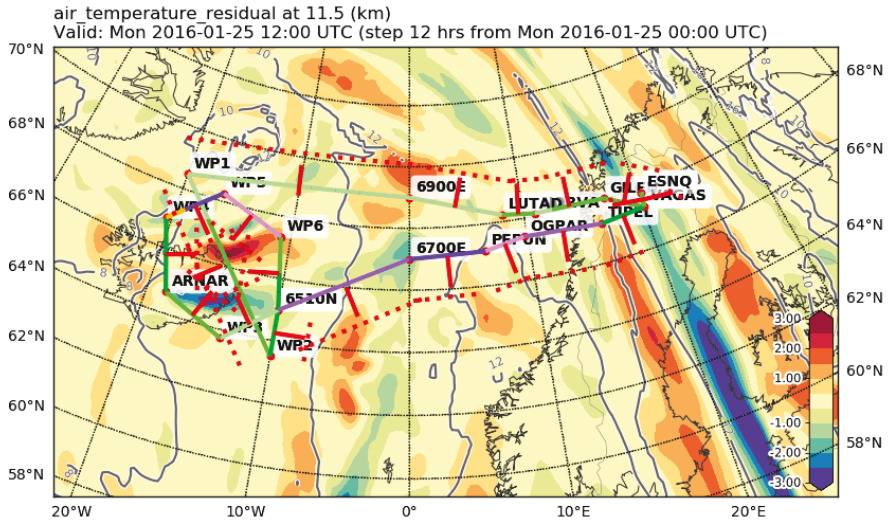

Figure 3.4: Top view of a gravity wave forecast for the flight on 25 January 2016 in the MSS flight planning tool including the GLORIA specific novel developments of the front end. The filled contours show the temperature perturbation field. The flight path is coloured with respect to the angle between a GLORIA 90° azimuth LOS and the sun. The angle becomes larger, thus less critical, from red over orange, dark violet, light violet, dark green, to light green. The red dots mark the tangent points at 12 km altitude, the red lines mark the viewing direction of 90° azimuth.

This feature simplifies the location of self-match flight patterns, where the GLORIA measurements from one leg cover the flight path of another leg at a lower altitude. The exact altitude difference and horizontal distance between the two legs can now be determined directly in the flight planning tool. During calibration sequences, GLORIA takes deep space measurements, meaning its LOS is pointed slightly upwards. If the LOS is points into the sun, the measurement quality is strongly decreased and not sufficient for calibration any more. Direct sunlight on the entrance window of GLORIA, which does not directly enter the optics, will heat the window, increase its emissions, and reduce the measurement quality.

Thus, I included the display of solar azimuth and elevation angles along the flight track. This new feature, was then used to adjust the horizontal viewing direction of the instrument to improve the measurement quality and to plan the calibration sequences.

To get from a scientifically optimal flight plan to a real flight plan submitted to air traffic control, several iterations between scientist and pilots are necessary. Originally, the exchange of flight plans took place through simple text files or even on paper and the coordinates of the flight path had to be entered by hand in the respective flight planning tool of the other party. To simplify this data exchange, I implemented in MSS new reading and writing routines for several data formats, like csv[1] or FliteStar[2]. Further, air traffic control regions and restricted areas were added to MSS to reduce the number of iteration loops between pilots and scientists.

3.4 The Atmospheric Infrared Sounder (AIRS)

The Atmospheric Infrared Sounder (AIRS) is one of the instruments onboard NASA's Earth Observing System (EOS) Aqua satellite (see also Aumann et al., 2003; Chahine et al., 2006). AIRS is a nadir-scanning instrument that performs scans across the satellite track. Each scan consists of 90 footprints across track, and the width of the swath is about 1800 km. At nadir, the footprint diameter is 13.5 km, and the across-track sampling step is 13 km. The along-track sampling distance is 18 km. The EOS Aqua satellite is in a sun-synchronous orbit with fixed equator crossing times of 13:30 LT for the ascending orbit (flying northward) and 01:30 LT for the descending orbit (flying southward).

AIRS is a hyperspectral radiometer that measures atmospheric emissions of CO_2 with high spectral resolution. In contrast to limb geometry,

[1] comma-separated values file format

[2] FliteStar is a commercial flight planning tool from Jeppesen Sanderson, Inc. used by the HALO operating crew.

nadir sounding depends on the saturation of the radiance along the ray-path to gain vertical information. Depending on the wavelength, the sensitivity function along LOS peaks at different altitudes (Hoffmann and Alexander, 2009). By combining multiple spectral lines, a temperature profile can be retrieved. In contrast to limb sounders, the vertical resolutions of these nadir profiles are usually on the order of 10 km to 20 km.

For retrievals of night time data, emissions of the 4.3 µm and the 15 µm spectral bands can be combined. For day time retrievals only the 15 µm band is used due to non-local thermodynamic equilibrium effects which influence the 4.3 µm band. Correspondingly, AIRS night time data have a better vertical resolution and lower noise. Except for polar latitudes, day time data correspond to ascending orbits, and night time data to descending orbits, respectively. The AIRS temperature retrievals presented in this thesis follow the retrieval set-up presented by Hoffmann and Alexander (2009).

The vertical resolution of these temperature retrievals varies from 6.6 km to 14.7 km depending on altitude. The total accuracy is between 2.1 K and 0.6 K, the precision between 1.5 K and 2.1 K (Hoffmann and Alexander, 2009).

No observation technique can resolve all scales of gravity waves. In order to allow quantitative assessments of gravity wave parameters derived from measurements, the sensitivity function of the observation technique with respect to gravity waves with different spatial scales, also called observational filter, has to be considered (Ern et al., 2005; Alexander et al., 2010; Trinh et al., 2016). The observational filter maps the true gravity wave amplitude or momentum flux onto the amplitude or momentum flux observed by the given measurement technique. The AIRS observational filter for the middle stratosphere (36 km) is shown in Figure 3.5. For vertical wavelengths below 25 km the temperature amplitude of the gravity wave is underestimated. In addition to previous studies, this thesis also uses an observational filter for the vertical wavelength. The importance of this additional observational filter for the vertical wavelength will be shown in Chapter 7. While the temperature amplitude is underestimated for waves with short vertical wavelengths,

the vertical wavelength is overestimated by up to 50 %. As such, the gravity wave spectrum is shifted towards higher vertical wavelengths and AIRS gravity wave observations of waves with vertical wavelengths below 30 km have to be treated carefully.

These values do not include effects caused by the scale separation of the measured temperature into background temperature and gravity wave perturbations. Sensitivity functions including the effect of scale separation by an across-track 4th-order polynomial (a standard procedure for nadir sounders) are given, for example, by Meyer et al. (2018) or the supporting information of Ern et al. (2017). Further, gravity waves with horizontal wavelengths of less than 100 km that may be affected by the limited AIRS footprint size are not described by the observational filter in Figure 3.5.

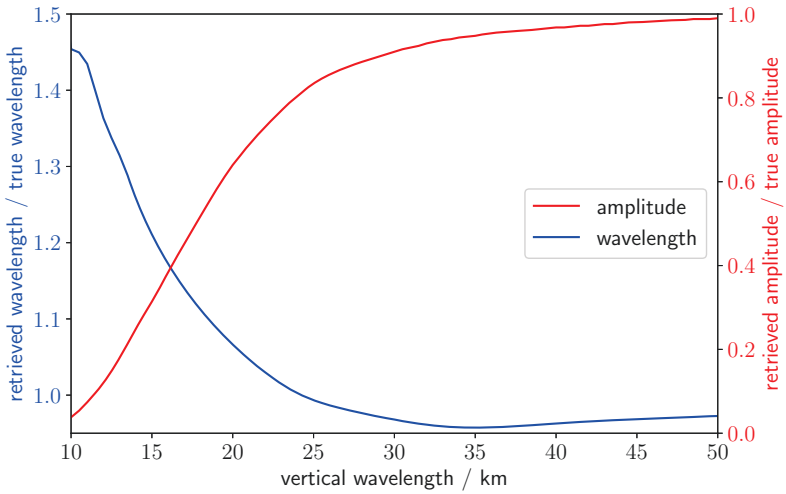

Figure 3.5: Sensitivity function of AIRS for gravity wave amplitude (red) and vertical wavelength (blue) at given vertical wavelengths. Figure from Krisch et al. (2020).

3.5 Analysis and reanalysis model data from the European Centre for Medium-Range Weather Forecasts (ECMWF)

Modern numerical weather prediction (NWP) relies on two fundamental components, first, a high-resolution general circulation model (GCM) which includes all processes relevant for weather forecast and, second, the assimilation of a multitude of different types of measurements in order to constrain the model state as accurately as possible to the real atmospheric state. The European Centre for Medium-Range Weather Forecasts (ECMWF) integrated forecast system assimilates measurement data by a method called 4-D var. The model is constrained by measurements clustered in 12 hour windows from 9 UTC to 21 UTC and from 21 UTC to 9 UTC the next morning. Measurements up to an altitude of approximately 40 km are used in the assimilation. A model state is saved every 3 hours for the analysis runs and hourly for the ERA5 reanalysis runs. These model fields provide a close to reality background for the propagation of gravity waves with the GROGRAT model (Chapter 2.3). Further, realistic excitation of gravity waves is triggered by processes resolved by the model, i.e. mesoscale orography and spontaneous adjustment. Other gravity wave source processes such as convection are parametrized in the GCM and the emitted gravity waves are less realistic (Preusse et al., 2014). It has to be noted, that the assimilation does not constrain gravity waves themselves, thus, they can develop freely from the model physics.

The dynamical core of the ECMWF GCM is based on a spectral representation of the atmosphere. The spatial resolution was enhanced several times in the recent decade. The ERA5 reanalysis has a horizontal resolution of 31 km at the equator on 137 levels from the surface up to 80 km. The current ECMWF analysis used in this thesis has a horizontal resolution of 16 km at the equator with the same amount of vertical levels as ERA5. Though the dynamical core would in principal allow to resolve waves with horizontal wavelength double the horizontal resolution, hyperdiffusion, which was introduced to provide numerical

stability, limits well-resolved waves to about 10 spatial grid points (Skamarock, 2004; Preusse et al., 2014). Thus, waves of horizontal wavelengths longer than approximately 300 km are fully resolved in the ERA5 reanalysis data and waves of horizontal wavelengths longer than approximately 150 km in the analysis fields. Shorter waves, if excited e.g. by topography, may still be present but are suppressed in amplitude.

In summary, the ERA5 reanalysis has a higher temporal, but lower horizontal resolution than the ECMWF analysis. Accordingly, for small-scale waves the ECMWF analysis is more accurate, for fast changing situations, ERA5 might be preferable.

4 Wave characterisation

To scientifically analyse the measurement and model data described in Chapter 3 with respect to gravity waves, the perturbations caused by gravity waves have to be identified and the waves fully characterised. This process happens in two steps. First, the synoptic scale background is identified by performing a scale separation and then subtracted from the measurements to isolate the gravity wave structure (Section 4.1 and Krisch et al. (2020, Appendix)). Second, the gravity wave structure is characterised using a spectral analysis, which allows to determine characteristic wave vectors and amplitudes (Section 4.2).

4.1 Scale separation of atmospheric variables

The atmospheric temperature structure in the mid-latitude stratosphere and troposphere is shaped by dynamical features of different spatial and temporal scales. The most important features are the mean atmospheric temperature, synoptic planetary waves and multiple small scale processes including gravity waves. The mean atmospheric temperature is governed by slow radiative processes and large scale meridional circulations. These vary slowly in altitude and latitude, but are assumed to remain constant in zonal direction. Synoptic scale planetary waves surround the Earth on latitude circles. Thus, they have integer zonal wave numbers[1]. In the mid stratosphere, the main planetary wave modes have zonal wave numbers of 1−6. In the lower stratosphere and troposphere,

[1] A wave with zonal wave number 1 has one crest and one trough on a zonal path around the Earth. This corresponds to a zonal wavelength of ≈40 000 km at the equator and ≈20 000 km at 60° latitude. A wave with zonal wave number of 20 has 20 crests and troughs and, thus, a zonal wavelength of ≈2000 km at the equator.

also planetary waves with higher zonal wave numbers become important. gravity waves have horizontal wavelengths of a few kilometres to several thousand kilometres. However, due to the GLORIA measurement resolution and extent, this chapter will concentrate on the identification of mesoscale gravity waves with horizontal wavelengths between 100 km and 1000 km.

For global data sets, background and gravity wave fluctuations are traditionally separated using zonal low pass filtering with a cut-off wave number of 6 in the mid-stratosphere (e.g. Fetzer and Gille, 1994; Ern et al., 2006, 2018). This zonal filter might allocate gravity wave structures with long zonal but short vertical and/or meridional wavelengths to the background. A sliding polynomial smoothing with a Savitzky-Golay filter (SG-filter; Savitzky and Golay, 1964) in the vertical and/or meridional direction can be applied additionally to the background field to smear out these small scale signals. Through subtracting the smooth background temperature from the total temperature, one receives a perturbation field containing different small scale processes like gravity waves or different weather systems like convection or fronts. However, these weather systems are only present in the troposphere and, thus, do not interfere with the characterisation of gravity waves in the stratosphere. For the analysis and reanalysis model data used in this thesis, a zonal Fast Fourier transform (FFT) filter with cut-off wave number 18 was combined with a 4th order SG-filter over a window of 5 km in the vertical and a 3rd order SG-filter over a window of 750 km in the meridional direction to get a smooth background.

Due to the local nature of GLORIA measurements, global filtering algorithms, like the zonal method described above, are not suitable. A number of low-pass filters are in general suitable for the scale separation on regional data sets. To identify the best method for the GLORIA measurements, a 2D FFT-filter, a running mean filter, a Gaussian filter, an SG-filter, and a Butterworth filter (BW-filter; Butterworth,1930) are compared in the following (see also appendix of Krisch et al., 2020). The separation of pass and stop frequencies are handled differently in each method (Figure 4.1). The FFT-filter has a very sharp transition from pass to stop band, but requires a periodic signal, which GLORIA mea-

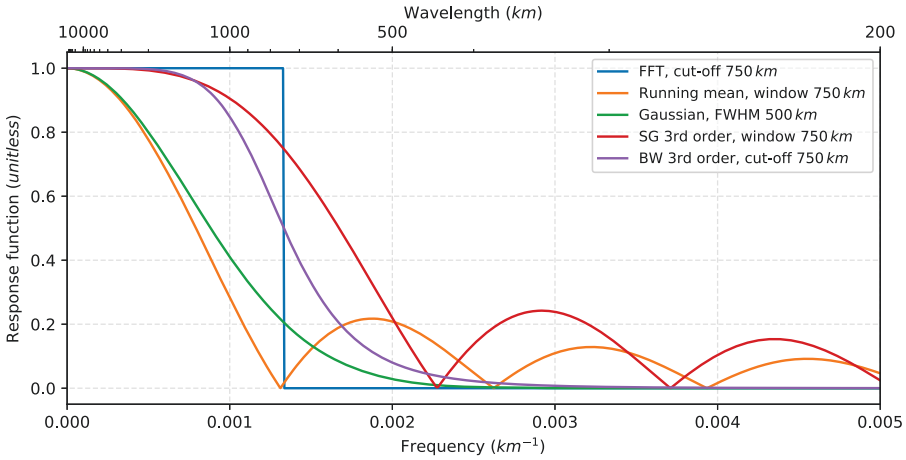

Figure 4.1: Frequency response of different low-pass filters to a delta function. Shown are a Fast Fourier Transform (FFT) with a cut-off wavelength of 750 km, a running mean filter with a window width of 750 km, a Gaussian filter with a full width at half maximum (FWHM) of 500 km, a Savitzky-Golay (SG) 3rd order polynomial smoothing in running windows of 750 km width, and a 3rd order Butterworth (BW) filter with a cut-off wavelength of 750 km. Figure from appendix of Krisch et al. (2020).

surements cannot provide. The running mean filter and the Gaussian filter have both a very flat transition between pass and stop band. This makes a clear separation more challenging. In contrast, the SG-filter as well as the BW-filter have a faster transition between pass and stop band.

To test these filters systematically on GLORIA-like data, a synthetic temperature field is constructed, which covers an altitude range from 8 km to 15 km and has a horizontal extent of 1000 km centred around 0 km (Figure 4.2). This temperature field is composed of a mean background profile (Figure 4.2 a-c), a synoptic scale wave (Figure 4.2 d-f) and a mesoscale gravity wave (Figure 4.2 g-i). The mean temperature is defined in three altitude ranges with different properties to generate a smooth transition. Above 11 km, a constant value of 220 K is assumed. Between 11 km and 9 km altitude, the temperature gradient smoothly

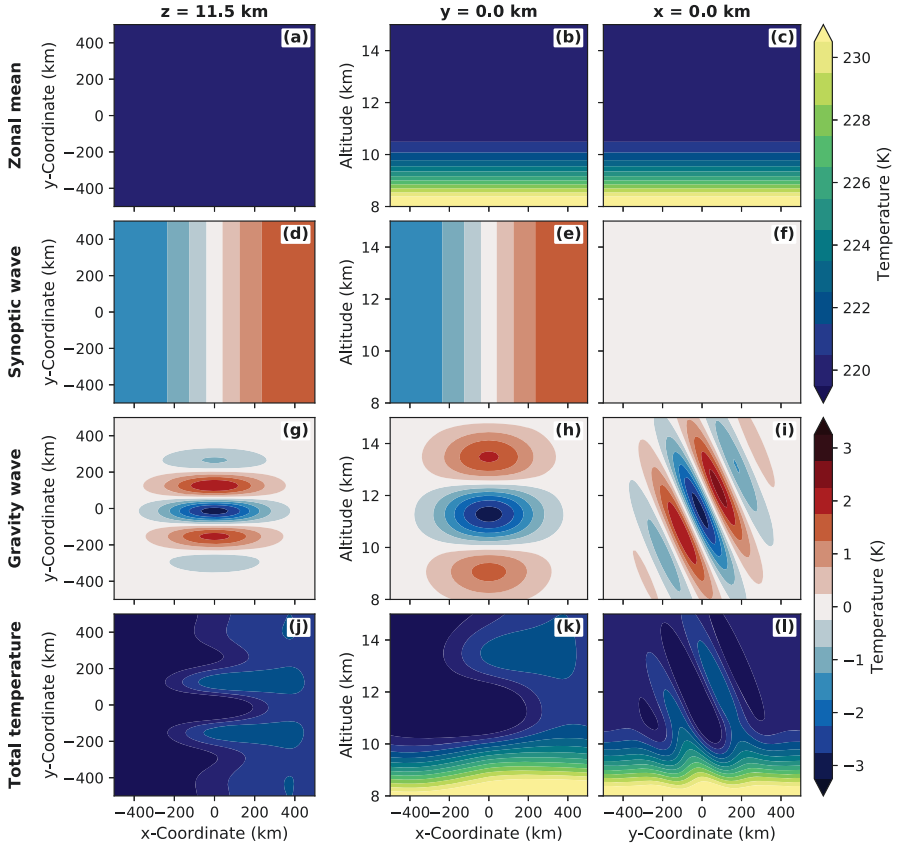

Figure 4.2: Synthetic temperature structure generated to test different scale separation methods. The total temperature (last row) is constructed from a mean temperature field (first row), a synoptic scale zonal wave (second row) and a mesoscale gravity wave (third row). Detailed descriptions of the different fields and their exact structure can be found in the text. Figure adapted from appendix of Krisch et al. (2020).

Table 4.1: Different filters used for the scale separation of gravity waves and background and their set-up parameters.

	polynomial	cut-off wavelength	window length	FWHM
Fast Fourier transform (FFT)		750 km		
Running mean			750 km	
Gaussian				500 km
Savitzky-Golay (SG)	3rd order		750 km	
Butterworth (BW)	3rd order	750 km		

decreases with altitude from $0\,\mathrm{K\,km^{-1}}$ to $-6.5\,\mathrm{K\,km^{-1}}$. Below 9 km the temperature gradient is then kept constant at $-6.5\,\mathrm{K\,km^{-1}}$. The synoptic scale wave has a wavelength of 1500 km (corresponds to wave number 12 at 60° latitude), phase fronts oriented parallel to the y-axis and a temperature amplitude of 1.5 K. The mesoscale gravity wave is chosen to have a horizontal orientation perpendicular to the synoptic scale wave, a vertical wavelength of 300 km, and a horizontal wavelength of 5 km. The constructed wave is further multiplied by Gaussian functions in all spatial dimensions to simulate the often localised nature of real gravity waves. The Gaussian functions have a FWHM of 400 km in both horizontal directions and a FWHM of 5 km in the vertical. The sum of mean temperature, synoptic scale wave and gravity wave (Figure 4.2 j-l) is used as input for the different filtering algorithms.

All filtering algorithms are applied in both horizontal dimensions, to avoid, that gravity waves which are oriented along one horizontal axis, are erroneously considered as background. The exact set-ups of the different filters are summarized in Table 4.1. The results are shown in Figure 4.3. With the FFT-filter (first row), the running mean (second row) and the Gaussian-filter (third row), parts of the synoptic scale wave remain in the perturbation field. Thus, these filters are not appropriate for the scale separation of GLORIA data. Both, the SG-filter (fourth row) as well as the BW-filter (fifth row) qualitatively reproduce the original gravity wave structure with minimal altering effects. The BW-filter seems to shift the wave phases outwards, which is likely to be due to a small part

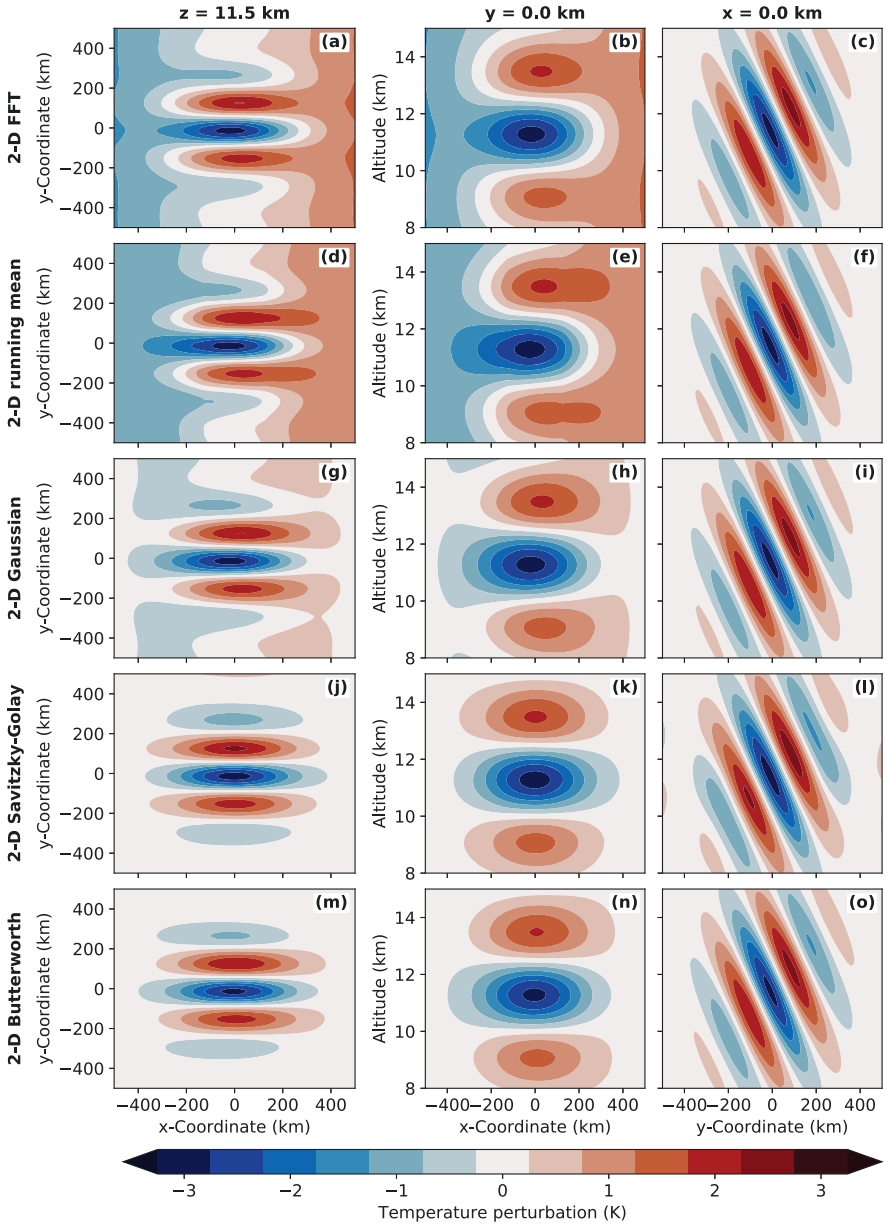

Figure 4.3: Temperature fluctuations calculated by subtracting the low-pass filtered background fields from the original synthetic temperature field (Figure 4.2 j-l). Figure adapted from appendix of Krisch et al. (2020).

of the synoptic scale wave remaining in the signal. A quantitative comparison is done by calculating the Pearson coefficient P correlating the original wave with the filtered results:

$$P = \frac{\sum_{i=1}^{n}(x_i - \bar{x})(y_i - \bar{y})}{\sqrt{\sum_{i=1}^{n}(x_i - \bar{x})^2}\sqrt{\sum_{i=1}^{n}(y_i - \bar{y})^2}}, \tag{4.1}$$

with $x_1 \dots x_n$ all data points of the original wave field, $\bar{x}$ the mean of the original wave field, $y_1 \dots y_n$ all data points of the remaining wave field after filtering, and $\bar{y}$ the mean of the remaining wave field after filtering. The FFT-filter reaches a correlation with the original of 53.2 %, the running mean of 51.5 %, the Gaussian of 86.9 %, the SG-filter of 99.4 % and the BW-filter of 98.5 %. Thus, the Pearson coefficients confirm that the SG-filter is the best choice for GLORIA measurements. Other orientations and wavelengths of both synoptic scale waves and gravity waves have been tested and lead to similar results.

Including an additional filter over the altitude dimension can further improve the results. For the GLORIA measurements presented in this thesis, an additional 3rd order SG-filter with a window length of 3 km is applied in the vertical after the horizontal filtering.

4.2 Spectral analysis using a three-dimensional sinusoidal fitting routine (S3D)

To characterise the temperature perturbations with respect to gravity waves, wave parameters (horizontal and vertical wavelengths, wave amplitude and wave direction) are derived. For this task, a small-wave decomposition method called three-dimensional sinusoidal fitting routine (S3D) has been developed in Jülich. The method has already been used for the characterisation of gravity waves in several publications (Lehmann et al., 2012; Preusse et al., 2014; Ern et al., 2017).

S3D uses a least square approach to fit a sine function to the 3-D tem-

perature perturbation field $T'(\boldsymbol{x})$ received after scale separation:

$$\chi^2 = \sum_i \frac{(f(\boldsymbol{x}_i) - T'(\boldsymbol{x}_i))^2}{\sigma_f^2(\boldsymbol{x}_i)} \tag{4.2}$$

with weighting function $\sigma_f^2(\boldsymbol{x})$ and the sine function

$$f(\boldsymbol{x}) = \hat{T} \cdot \sin(\boldsymbol{k}\boldsymbol{x} + \phi) = A \cdot \sin(\boldsymbol{k}\boldsymbol{x}) + B \cdot \cos(\boldsymbol{k}\boldsymbol{x}), \tag{4.3}$$

with 3-D wave vector $\boldsymbol{k} = (k, l, m)$, temperature amplitude $\hat{T}$, wave phase ϕ, sine amplitude $A = \hat{T}\cos\phi$, and cosine amplitude $B = \hat{T}\sin\phi$. The reformulation into a sine and a cosine part reduces the number of fitting parameters, since A and B can be calculated analytically for every combination of wave vector $\boldsymbol{k}$ and atmospheric temperature perturbation $T'(\boldsymbol{x})$. The wave numbers k, l, and m are derived in an iterative minimisation scheme reducing χ^2. There are different minimisation approaches implemented, such as a parameter nesting and steepest descent. The iteration is ended when the method converges (i.e. χ^2 falls below a limit) or a maximum number of iteration steps is reached. As weighting function, a Gaussian can be applied to reduce the impact of data further away from the cube centre. After the minimisation is completed, the amplitudes A and B are converted back into the temperature amplitude $\hat{T}$ and the wave phase ϕ, which are more intuitive for physical interpretation.

The method is applied on analysis cubes – small three-dimensional sub-regions of the perturbation field. In each cube, a superposition of monochromatic sine waves is assumed and determined by fitting. The quality of the results depends on the used cube size. If the cube is too large compared to the resulting wavelengths small fluctuations get masked by larger scale waves. Additionally, since real gravity waves are highly variable and complex, an approximation with monochromatic waves is only valid inside small areas (see also Chapter 6.4). If the cube is too small, the amount of data points is not sufficient to uniquely identify the dominant wave structure. Systematic tests with synthetic waves have shown, that cube sizes covering only 40 % of one wave cycle per

direction in general still lead to reasonable results.

Originally, the method was implemented in the programming language IDL and used for satellite or numerical weather prediction model data. To apply S3D to GLORIA data, the code had to be adapted. To make it easier accessible, the code was first transferred to the open source language Python, and stored in a version controlled repository (Git), to manage the changes made by different contributors. The new version management system also includes an issue management system for necessary future code changes, which can subsequently be addressed by different developers. The following changes are made to make the code applicable to GLORIA measurements: Since GLORIA measurements are sampled on regular Cartesian km-grids instead of spherical longitude-latitude-grids, a new reading routine is implemented. The generation of the small analysis cubes is updated to handle the new grids. To reduce the impact of measurement data with low confidence values, the weighting function σ_f^2 can now be given as an external input and is chosen to be 1 if a tangent point exists in the corresponding grid cell and 10^5 if not. GLORIA measurement data show a highly variable strength in the temperature perturbations. To recover these variations in gravity wave amplitude and still keep the cube sizes large enough for reasonable fits of the wave vector, a refitting routine is inserted. The wave vector is determined in large cube sizes first and then, in smaller cube sizes, the wave amplitude and phase are calculated analytically using the wave vectors determined before.

5 The measurement sensitivity of GLORIA to gravity waves

Airborne limb imaging is a novel technique, which for the first time allows the measurement of 3-D temperature and trace gas distributions in the upper troposphere–lower stratosphere region (Ungermann et al., 2011; Kaufmann et al., 2015). In this Chapter, the capability of GLORIA, the first implementation of this technique, to measure the 3-D structure of mesoscale gravity waves is investigated (see also Krisch et al., 2018). In this context, the following research questions stated in the introduction will be answered in this Chapter: Are the achieved 3-D volumes of atmospheric temperature sufficient in size and spatial resolution to fully characterise mesoscale gravity waves? How does the measurement set-up influence the quality of retrieved wave parameters? Can limited angle tomography be used to study mesoscale gravity waves? What is the optimal flight strategy to observe these waves with GLORIA?

For this purpose, the accuracy of reconstructing gravity wave parameters, such as horizontal and vertical wavelength, amplitude and wave orientation is studied with an end-to-end simulation study for full angle tomography (FAT) and limited angle tomography (LAT). The concept of the end-to-end simulation is described in Section 5.1. The results for FAT and LAT are presented in Sections 5.2 and 5.3, respectively. In addition to this synthetic study, the temperature structures reconstructed by FAT and LAT are compared for a real measurement case on 25 January 2016 (Section 5.4). On this day, the HALO aircraft first performed a linear flight through a gravity wave, which was followed by a hexagon around the same structure. Thus, both techniques are applicable.

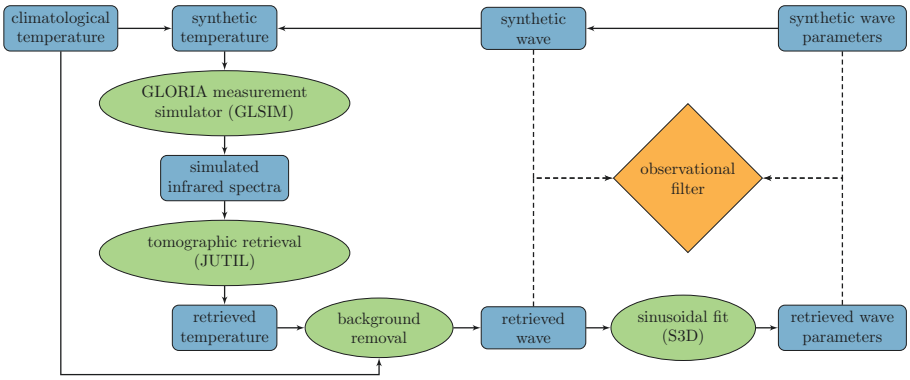

Figure 5.1: Methodological concept of the performed simulation study. A detailed description can be found in the text. Figure from Krisch et al. (2018).

5.1 Concept of the sensitivity study

Figure 5.1 shows the concept of the end-to-end simulation, which investigates the sensitivity of different GLORIA measurement concepts to gravity waves. The basic idea is to generate a monochromatic gravity wave of fixed amplitude and wavelength and see if and with which accuracy these wave parameters can be reproduced from simulated measurements. For this the standard processing chain of GLORIA with retrieval, scale separation, and S3D fit is used.

To simulate a realistic atmosphere, a climatological field $\boldsymbol{a}_c \in \mathbb{R}^n$ from Remedios et al. (2007) was used, including temperature, pressure and several trace gases. The climatological temperature $\boldsymbol{T}_c \in \mathbb{R}^m$ was perturbed at each point $\boldsymbol{x}_i \in \mathbb{R}^3$ in space by a synthetic wave

$$w_s^i = \hat{T} \cdot \sin(\boldsymbol{k}\boldsymbol{x}_i + \phi), \tag{5.1}$$

where $\hat{T}$ is the temperature amplitude, $\boldsymbol{k} \in \mathbb{R}^3$ the 3-D wave vector, and ϕ the phase of the wave. In the present simulation study, the temperature amplitude $\hat{T}$ is chosen to be 3 K and the wave phase ϕ to be 0°. From now on, the 3-D wave vector $\boldsymbol{k} = (k, l, m)$ will mainly be ex-

pressed in terms of vertical wavelength $\lambda_z = \frac{2\pi}{m}$, horizontal wavelength $\lambda_h = \frac{2\pi}{\sqrt{k^2+l^2}}$, and horizontal wave direction $\psi = \arctan2(k,l)$[1]. Thus, if a downward pointing wave vector is assumed ($m < 0$, upward propagating wave), a wave with wave direction of 0° has east-west oriented phase fronts and is tilted towards the north, a wave with wave direction of 180° is tilted towards the south.

This predetermined atmospheric state with synthetic temperature $\boldsymbol{T}_s$ is used to calculate a set of simulated infra-red radiances using the GLORIA measurement simulator (GLSIM; Chapter 3.2.2.1). For simulation of FAT a hexagonal flight path around 0° N and 0° E with 200 km radius was chosen, according to the hexagonal flight path tested in (Ungermann et al., 2011) for trace gas retrievals. For LAT a flight along the zero meridian from 5° S to 5° N was simulated. Using these simulated infrared spectra, a tomographic retrieval (Chapter 3.2.2.2) is performed. This retrieval uses only a well-defined set of infrared radiances (Table 3.4, rows 1 to 7) and can reconstruct the atmosphere only in a reduced area, limited by the measurement geometry.

The retrieved temperature structure has to be scale separated into temperature background and gravity wave perturbations before applying the wave characterisation tool S3D to derive the wave parameters. To solely investigate the sensitivity of the measurement concept and exclude any additional effects due to the scale separation, the filtering methods presented in Chapter 4.1 are not used for this simulation study. Instead the original temperature background from the climatology $\boldsymbol{T}_c$ is subtracted from the retrieved temperature field $\boldsymbol{T}_r \in \mathbb{R}^m$ to obtain the retrieved wave perturbation $\boldsymbol{w}_r \in \mathbb{R}^m$. Due to the GLORIA measurement resolution and extent, mesoscale gravity waves with horizontal wavelengths between 100 km and 1000 km and vertical wavelengths between 1 km and 10 km are investigated with this sensitivity study. As waves with wavelengths up to 2.5 times of the cube size can be characterised, a cube size of 400 km × 400 km × 5 km was chosen.

The retrieved wave structure and the results from the S3D wave char-

[1] $0° \leq \psi < 360°$ is the angle between y-axis and horizontal wave vector $\boldsymbol{k}_h = (k,l)$ in clock-wise direction.

acterisation, are then compared to the synthetic wave and the synthetic wave parameters, respectively. The absolute error of the retrieval within an area A containing the points $\boldsymbol{x}_i$, with $i = 1 \ldots n$, can be calculated as follows:

$$S = \frac{1}{n} \sum_{i=1}^{n} \Big(\boldsymbol{w}_s(\boldsymbol{x}_i) - \boldsymbol{w}_r(\boldsymbol{x}_i) \Big) \tag{5.2}$$

For a fair comparison, the area A must be chosen in a way, that it covers the measurement region. The best coverage is achieved by choosing the area A between 9.5 km to 11.5 km altitude, 1.75° to 2.25° longitude, and −1° to 1° latitude for LAT and 9.5 km to 11.5 km altitude, −1° to 1° longitude, and −1° to 1° latitude for FAT. The absolute error is used to determine the ability of the measurement technique to reproduce the temperature amplitude $\hat{T}$ of a certain synthetic wave $\boldsymbol{w}_s$:

$$O_{\hat{T}} = \frac{\hat{T}_s - S}{\hat{T}_s}. \tag{5.3}$$

By repeating this process for different horizontal and vertical wavelengths, the observational filter of the measurement concept is established. The observational filter is a helpful measure for the reproducibility of gravity waves by the measurement set-up and the retrieval concept. The knowledge of the observational filter is necessary for meaningful comparisons of measurements from different instruments or measurement and model results (Ern et al., 2005; Alexander et al., 2010; Trinh et al., 2015). However, this traditional observational filter does not give detailed information about all wave parameters relevant, e.g., for determining the GWMF (Equation 2.33). Using the results of the S3D wave characterisation, the concept of the observational filter thus is expanded to detailed observational filters for all important wave parameters. The observational filter for the horizontal wavelength λ_h, the vertical wavelength λ_z, the horizontal wave direction ψ, and the temperature amplitude $\hat{T}$

are determined for each synthetic wave parameter as follows:

$$O_\zeta = 1 - \frac{1}{n}\sum_{i=1}^{n}\frac{\zeta_s - \zeta_r(\boldsymbol{x}_i)}{\zeta_s} \text{ for } \zeta \in \lambda_h, \lambda_z, \hat{T}, \psi. \tag{5.4}$$

The so constructed more specific observational filters define the quality of GLORIA measurements for gravity wave research. The observational filters for FAT and LAT are presented in Sections 5.2 and 5.3, respectively.

5.2 Full angle tomography (FAT)

Figure 5.2 shows an example of a FAT of a synthetic gravity wave. The temperature error of the retrieval remains below 0.5 K within the tangent point area. Thus, FAT is capable of reproducing this gravity wave with high accuracy. Conventional 1-D limb-sounding retrievals usually introduce large phase shifts (Preusse et al., 2002, 2009b; Ungermann et al., 2010a). These phase shifts can introduce errors in the vertical wavelength of up to 25 % (Preusse et al., 2002). With FAT, no phase shift between synthetic wave and retrieved wave is observed. Such a retrieval which does not introduce a phase shift, is a large improvement.

An S3D fit was performed for this retrieval with cube centres at 10.5 km altitude and cube sizes of 5 km × 400 km × 400 km. The results of this fit can be seen in Figure 5.3. The horizontal and vertical wavelength, and the horizontal wave direction are well reproduced within the hexagonal flight pattern. The original amplitude of 3 K is underestimated by only 0.1 K. The area outside the hexagonal flight pattern is not covered by measurements. Thus, the quality of the fitted wave parameters is expected to decrease towards the edges of the hexagonal flight path.

Such S3D results are used to construct the specific observational filters in Figure 5.4 following Equation 5.4. These observational filters show that the horizontal wavelength, the vertical wavelength and the horizontal wave direction are really well reproduced for all tested waves. The amplitude of the waves is continuously reduced for waves with horizontal wavelength below 200 km or vertical wavelength below 3 km.

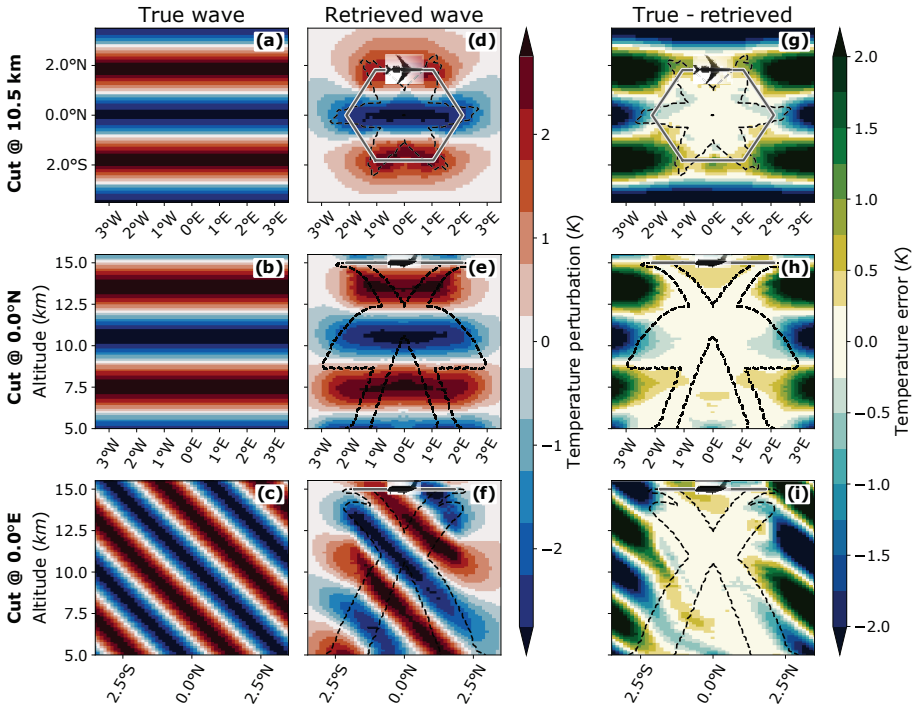

Figure 5.2: FAT retrieval results for a wave with 400 km horizontal, 6 km vertical wavelength, horizontal wave direction $\psi_s = 180°$, and temperature amplitude of 3 K. Panels **(a-c)** show the synthetic wave, panels **(d-e)** the retrieved wave, and panels **(g-i)** the difference between both. The black dashed lines mark the area covered by tangent points. Figure from Krisch et al. (2018).

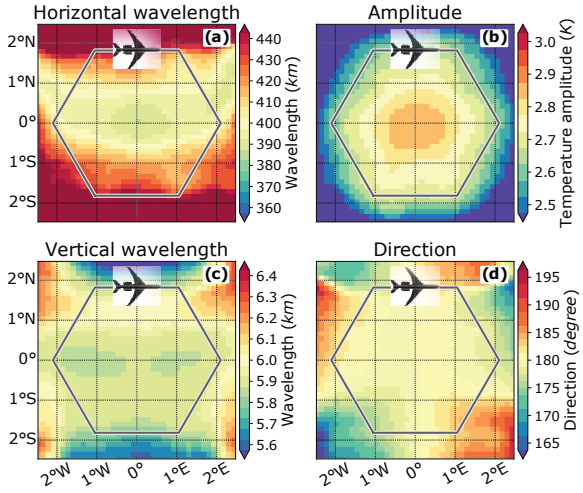

Figure 5.3: S3D results of the FAT retrieval in Figure 5.2. Shown are horizontal wavelength λ_h **(a)**, temperature amplitude $\hat{T}$ **(b)**, vertical wavelength λ_z **(c)**, and horizontal wave direction ψ **(d)**. Figure from Krisch et al. (2018).

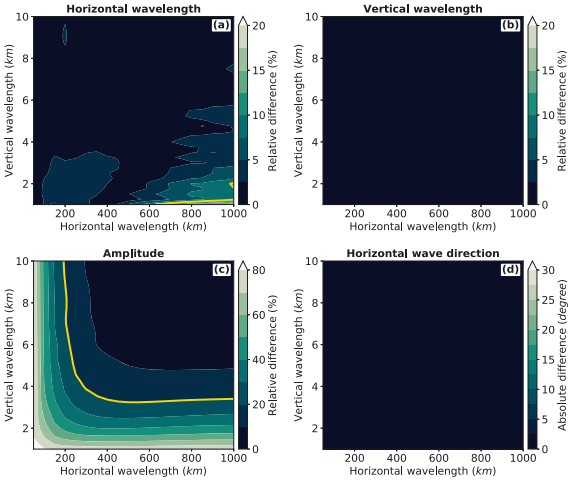

Figure 5.4: Specific observational filters for **(a)** horizontal wavelength λ_h, **(b)** vertical wavelength λ_z, **(c)** temperature amplitude $\hat{T}$, and **(d)** horizontal wave direction ψ for the FAT retrieval. The yellow lines mark errors of 10 % for the horizontal wavelength (Panel **(a)**) and 20 % for the amplitude (Panel **(c)**). Figure from Krisch et al. (2018)

This simulation study shows, that FAT is able to properly reconstruct the wave vectors of mesoscale gravity waves. However, the observational filter of the temperature amplitude has to be taken into account, when comparing these measurements to different data sets.

5.3 Limited angle tomography (LAT)

5.3.1 Dependence of the retrieval results on horizontal and vertical wavelengths

Figure 5.5 shows a comparison of the LAT retrieval results for different wavelengths. The waves in column 1 and 4 have a larger horizontal wavelength of 600 km compared to the waves in columns 2 and 3 with 200 km horizontal wavelength. The vertical wavelength of 6 km of the waves in columns 1 and 3 is longer than the vertical wavelength of 2 km of the waves in columns 2 and 4. The waves with large vertical wavelength in columns 1 and 3 are well reproduced by the LAT retrieval within the tangent point covered area with errors below 0.5 K. The waves with short vertical wavelengths show larger temperature errors of up to 1.5 K within the tangent point area. This difference comes from the curved LOS through the straight phase fronts, which leads to an averaging over different wave phases. For the waves with short vertical wavelength the LOS crosses multiple opposite wave phases, which decreases the measurement signal. A similar dependence of the sensitivity on the alignment of phase fronts with LOS was observed for sub-limb viewers (Wu and Waters, 1996; McLandress et al., 2000).

All retrieved waves show a slight V shape pattern, which is more emphasized for the waves with short vertical wavelength. This V shape is probably caused by the parabola shape of the LOS in the vertical. The retrieval does not know, where along the line-of-sight how much of the measured radiation was emitted, unless crossing measurements give sufficient information. As the LAT has fewer measurements at different angles, the temperature signal is redistributed according to the weighting function (Figure 3.3 b) along the LOS. This can be nicely seen

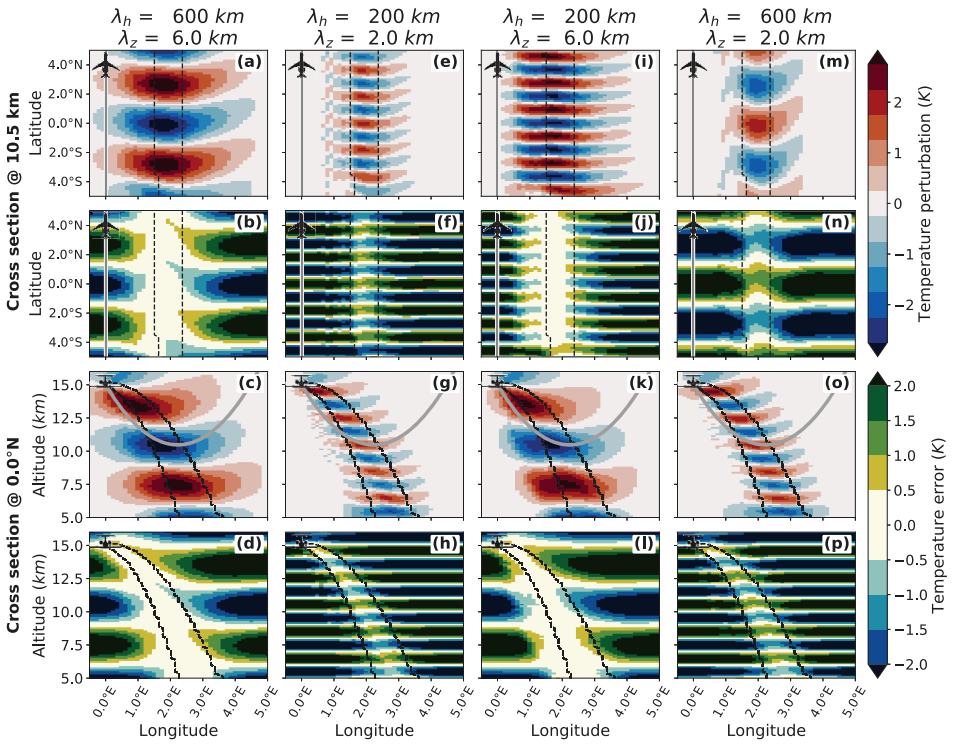

Figure 5.5: Cross sections of retrieved waves (first and third row) and differences between true and retrieved waves (second and fourth row) of the LAT retrieval. The different columns show waves with different horizontal and vertical wavelengths. The true horizontal wave orientation of all waves is $\psi_s = 180°$ and, thus, these waves have phase fronts perpendicular to the flight path. The black dashed lines mark the area covered by tangent points. The grey line in the vertical cross sections indicates a LOS for a measurement with 90° azimuth angle and tangent point altitude of 10.5 km. Figure from Krisch et al. (2018)

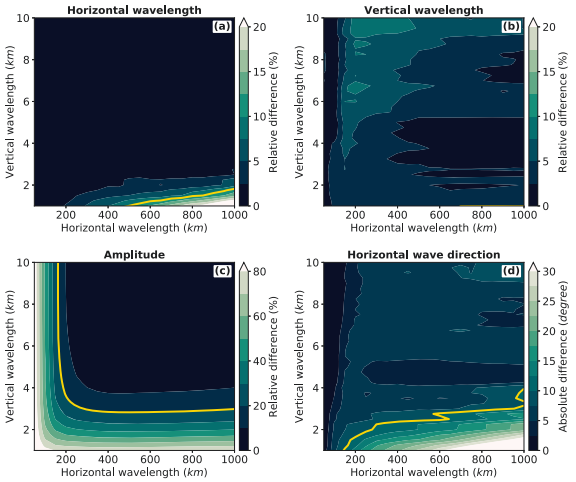

Figure 5.6: Specific observational filters for **(a)** horizontal wavelength λ_h, **(b)** vertical wavelength λ_z, **(c)** temperature amplitude $\hat{T}$, and **(d)** horizontal wave direction ψ for the LAT retrieval and true horizontal wave orientation $\psi_s = 180°$. These waves have phase fronts perpendicular to the flight path. The yellow lines mark errors of 10 %, 10 %, 20 %, and 10° in Panels **(a-d)**, respectively. Figure from Krisch et al. (2018)

in the vertical cross sections in Figure 5.5 g & o, where the warm temperature follows the LOS upwards behind the tangent point. This vertical shift of temperature also causes the northward oriented V shape in the horizontal cross sections.

As already for the FAT case, the specific observational filters were calculated using the S3D fits of the LAT retrievals (Figure 5.6). The deviations of horizontal and vertical wavelengths are mainly below 10 %. Only for very short vertical and very long horizontal wavelengths errors of above 20 % appear. This is probably due to the above mentioned V shape deformation of the wave, which is more difficult to fit with one single sinusoidal wave. The same problem appears for the horizontal wave direction. For waves with short vertical and long horizontal wavelengths and, thus a strong V shape, the direction cannot be derived properly anymore. For the rest of the waves the direction error stays everywhere

below 10°. The observational filter for the amplitude shows a similar pattern as for the FAT case.

5.3.2 Dependence of retrieval results on the wave orientation

Figure 5.7 depicts the retrieval results for waves with horizontal wave directions turned by 30° ($\psi_s = 210°$) compared to those in Figure 5.5. In the vertical, the phase fronts are tilted southward and, thus, towards the instrument (compare, e.g., Figure 5.7 k).

Overall, the structures are reproduced reasonably well. As for the perfectly perpendicularly-aligned waves already, waves with long vertical wavelengths (Figure 5.7 a–d and Figure 5.7 i–l) are reproduced better than waves with short vertical wavelengths (Figure 5.7 e–h and Figure 5.7 m–p).

Due to the tilt of the waves towards the aircraft, the LOS is partly aligned with the phase fronts before the tangent point. This effect is stronger for steep waves such as in Figure 5.7 k than for relatively flat waves such as in Figure 5.8 c, g and o. Due to this alignment the area of best sensitivity is shifted towards the aircraft for the steep wave. Spreading the signal now around this shifted sensitivity maximum, just spreads the signal along the same wave phase, as the LOS has little curvature in this region. Therefore, no strong shape deviation is observed. For the flat waves a similar V shape can be observed as for the waves in Figure 5.5, due to a spreading of signal along LOS around the tangent point.

In the observational filter (Figure 5.8) a small decrease in the quality of amplitude reproduction can be seen compared to the observational filter of perfectly east-west aligned waves (Figure 5.6). However, the wavelengths and wave direction are barely influenced and reproduced at a similar high quality. The V shape of the waves only occurs outside the tangent point region, thus proper horizontal wave directions can be observed.

Figure 5.9 shows the retrieval results for waves turned by −210° compared to Figure 5.5 ($\psi_s = 30°$). These waves are tilted northward and,

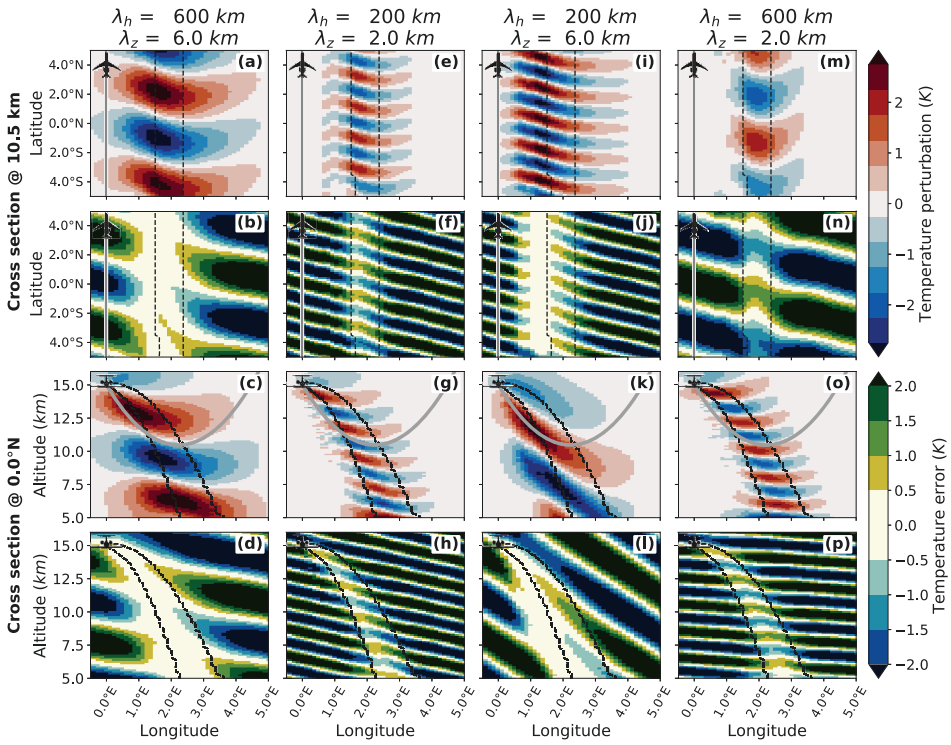

Figure 5.7: Cross sections of retrieved waves (first and third row) and differences between true and retrieved waves (second and fourth row) of the LAT retrieval. The different columns show waves with different horizontal and vertical wavelengths. The true horizontal wave orientation of all waves is $\psi_s = 210°$. These waves are tilted towards the aircraft. Figure from Krisch et al. (2018)

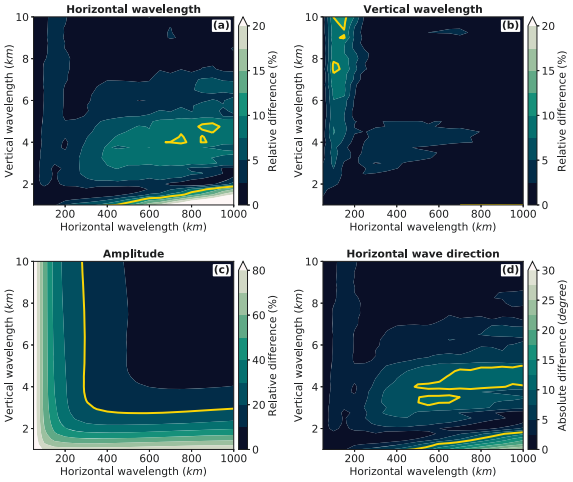

Figure 5.8: Specific observational filters for **(a)** horizontal wavelength λ_h, **(b)** vertical wavelength λ_z, **(c)** temperature amplitude $\hat{T}$,and **(d)** horizontal wave direction ψ for the LAT retrieval with true horizontal wave orientation $\psi_s = 210°$ and, thus, waves, which are tilted towards the aircraft. The yellow lines mark errors of 10 %, 10 %, 20 %, and 10° in Panels **(a-d)**, respectively. Figure from Krisch et al. (2018)

thus, away from the flight path. Only for the wave with large horizontal and large vertical wavelength (Figure 5.9 a–d) the temperature amplitude is reproduced well within the tangent point region. However, the horizontal orientation in this area, which should be similar to Figure 5.7 a, from north-west to south-east is not recovered. The same happens for waves with short vertical wavelengths (Figure 5.9 e–h and m–p): The information about the horizontal wave direction is lost within the retrieval. Again a V shape appears for all these waves. Due to the inverse vertical tilt compared to Figure 5.7, the opening of the V shape is this time to the south.

For steep waves (Figure 5.9 k) the main signal is again shifted, this time behind the tangent point area, where the LOS and the phase fronts are well aligned. Thus the spreading of the signal does not influence these waves as strongly as the flat waves and the horizontal orientation

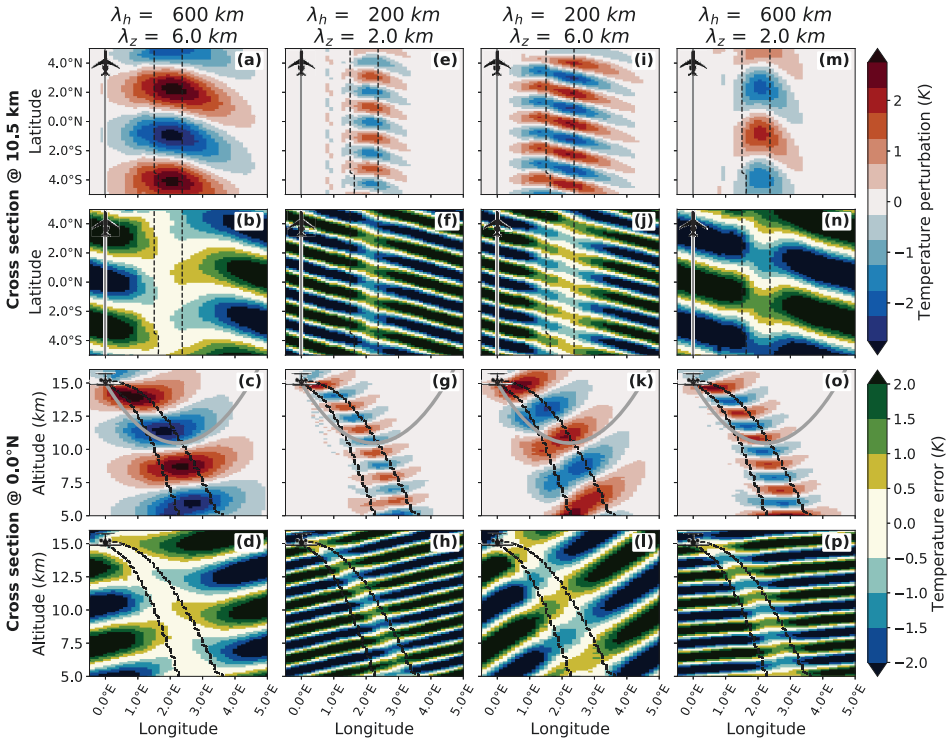

Figure 5.9: Cross sections of retrieved waves (first and third row) and differences between true and retrieved waves (second and fourth row) of the LAT retrieval. The different columns show waves with different horizontal and vertical wavelengths. The true horizontal wave orientation of all waves is $\psi_s = 30°$. These waves are tilted away from aircraft. Figure from Krisch et al. (2018)

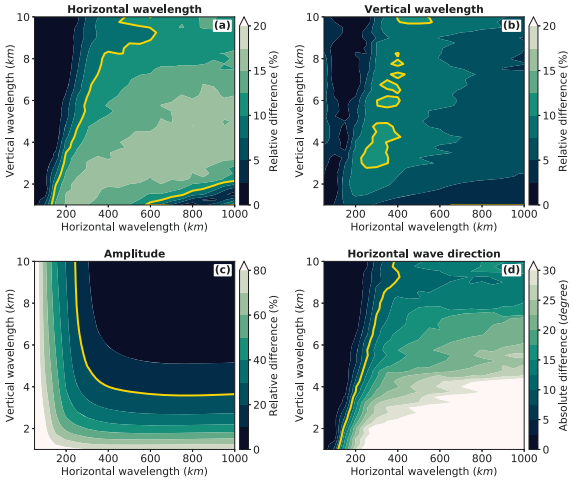

Figure 5.10: Specific observational filters for **(a)** horizontal wavelength λ_h, **(b)** vertical wavelength λ_z, **(c)** temperature amplitude $\hat{T}$, **(d)** and horizontal wave direction ψ for the LAT retrieval with true horizontal wave orientation $\psi_s = 30°$ and, thus, waves, which are tilted away from aircraft. The yellow lines mark errors of 10 %, 10 %, 20 %, and 10° in Panels **(a-d)**, respectively. Figure from Krisch et al. (2018)

does not get lost in the retrieval. The decreased amplitude compared to Figure 5.7 can be explained by the fact that the maximum of the weighting function along LOS is located slightly before the tangent point (Figure 3.3 b).

A similar picture is given from the observational filter in Figure 5.10. Even though the amplitude is underestimated for very steep waves, the horizontal wave orientation can be derived accurately. However, the flatter the wave gets, the worse the derived horizontal wave direction. For waves with horizontal to vertical wavelengths ratio of above 200, the direction error exceeds 30°. Also the horizontal wavelength reproduction is decreased somewhat compared to the two cases before (Figure 5.6 and Figure 5.8).

Further tests with horizontal wave direction $30° < \psi_s < 90°$ and $210° < \psi_s < 270°$ show a drastic decline in the amplitude sensitivity

to waves with short horizontal wavelengths. For waves tilted away from the flight path ($\psi_s > 30°$) the fit quality of the horizontal wave direction and the horizontal wavelength decreases drastically already at $\psi_s = 40°$.

These studies show that LAT applied to gravity waves gives best results for waves with phase fronts perpendicular to the flight path and, thus, horizontal wave vector $\psi_s = 180°$. However, if the wave is slightly turned, the quality of the derived wave parameters is not affected strongly as long as the wave is tilted towards the instrument ($180° <= \psi_s <= 210°$). In general, waves are best retrieved when their aspect ratio of horizontal and vertical wavelengths, i.e. their steepness, is favourable for an alignment with the LOS. In these cases, tilts towards and away from the instrument may give reasonable results. Thus, for LAT, a more or less accurate prediction of the wave orientation is required before the flight, to adjust the flight path respectively.

5.4 Comparison of LAT and FAT results for a real measurement case on 25 January 2016 over Iceland

From December 2015 to March 2016, GLORIA was deployed on board of the German research aircraft HALO for a research campaign covering several scientific targets (see Chapter 3.1). On 25 January 2016, a research flight over Iceland investigated a gravity wave excited at the Icelandic Mountain. A linear flight leg of 500 km length crossing the phase fronts almost perpendicular, was followed by a hexagonal flight pattern with 460 km diameter around the wave structure. A full discussion and scientific interpretation of this flight is given later in Chapter 6. Here, the focus is put on the comparison of the wave structures derived from LAT and FAT (Figure 5.11). For the LAT retrieval, only measurements taken during the linear flight leg are used. For the FAT retrieval, only those taken during the hexagonal flight are employed. To compare the differences in gravity wave structure, the temperature structure of both retrievals first has to be separated into background state and wave

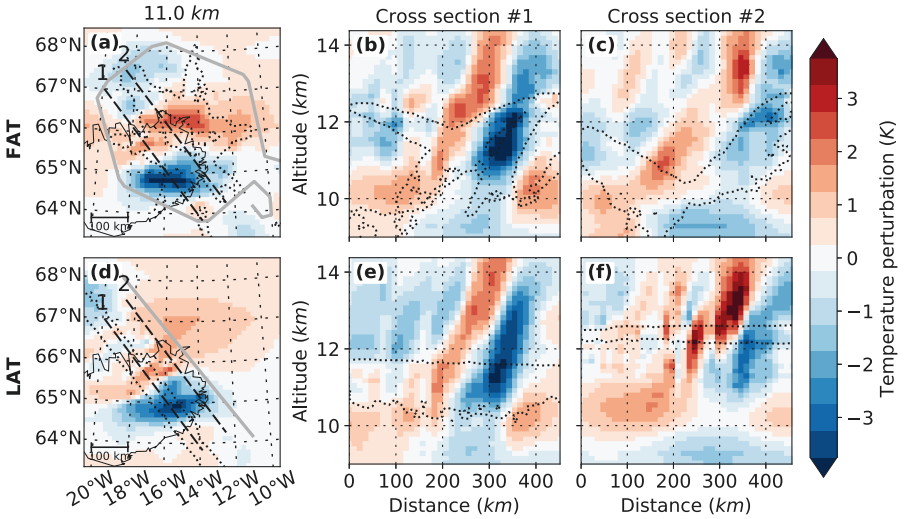

Figure 5.11: Comparison of FAT (Panels **(a-c)**) and LAT (Panels **(d-f)**) retrieval results for a research flight over Iceland on 25 January 2016. Shown are the temperature perturbations after scale separation as described in Sec. 4.1. The grey line indicates the part of the flight path, from which the measurements are used for the retrieval. The left column depicts horizontal cross sections at 11 km altitude, the two right columns present vertical cross sections along the dashed lines of the left column. The dotted lines mark the area covered by tangent points. Figure from Krisch et al. (2018)

perturbation. This is done using the scale separation methods described in Chapter 4.1.

In Figure 5.11, the temperature perturbation is shown for both LAT and FAT. In general the LAT results (Figure 5.11 d–e) agree very well with the FAT results (Figure 5.11 a–c) within the volume covered by both. FAT as well as LAT retrieval, show a superposition of waves with longer and shorter horizontal wavelengths. Differences in strength and scale of the waves, for example in cross section #2, can be explained due to the different tangent point coverage of both methods. Especially higher altitudes in cross section #2 are not well covered with tangent points in the FAT retrieval (Figure 5.11 c). This is probably the reason

Table 5.1: Diagnostics of the tomographic retrievals of the measurement flight on 25 January 2016. A detailed description how these parameters are calculated can be found in Chapter 3.2.2.3.

Quantity	FAT	LAT
Horizontal resolution	20 km	along flight track: 30 km across flight track: 70 km
Vertical resolution	200 m	400 m
Accuracy	0.5 K	0.7 K
Precision	0.05 K	0.05 K

why variations seen in the temperature perturbations are smaller in the FAT retrieval compared to LAT. Also the smaller scale waves in this region (Figure 5.11 f) are less prominent in the FAT retrieval (Figure 5.11 c).

A more quantitative comparison of the similarities of both retrievals can be given by the Pearson correlation coefficient. Including only areas which are covered by tangent points gives a Pearson correlation coefficient of 0.91. Expanding this area to places with measurement content larger than 0.8 (includes areas crossed by a LOS before or after the tangent point) still leads to a Pearson correlation coefficient of 0.75. Thus, as expected the two retrievals are highly correlated.

Following the description in Chapter 3.2.2.3, the spatial resolution and measurement errors have been calculated for both methods (Table 5.1). The FAT retrieval has a horizontal resolution of 20 km in the middle of the hexagon at an altitude of 10.5 km. The vertical resolution is 0.2 km. The precision (noise error) is below 0.05 K, the accuracy is on the order of 0.5 K. The LAT retrieval has a decreased spatial resolution of 30 km × 70 km × 0.4 km in along track, across track and vertical direction, respectively. The precision is similar to the FAT retrieval, the accuracy is slightly worse with 0.7 K.

A main advantage of 3-D tomographic measurement of gravity waves over conventional limb measurements is the ability to fully characterise the wave structure. This is here done by applying the S3D fitting routine. Figure 5.12 shows the wave parameters obtained from these fits for both cases. Within the confidence area of our fits, all wave parame-

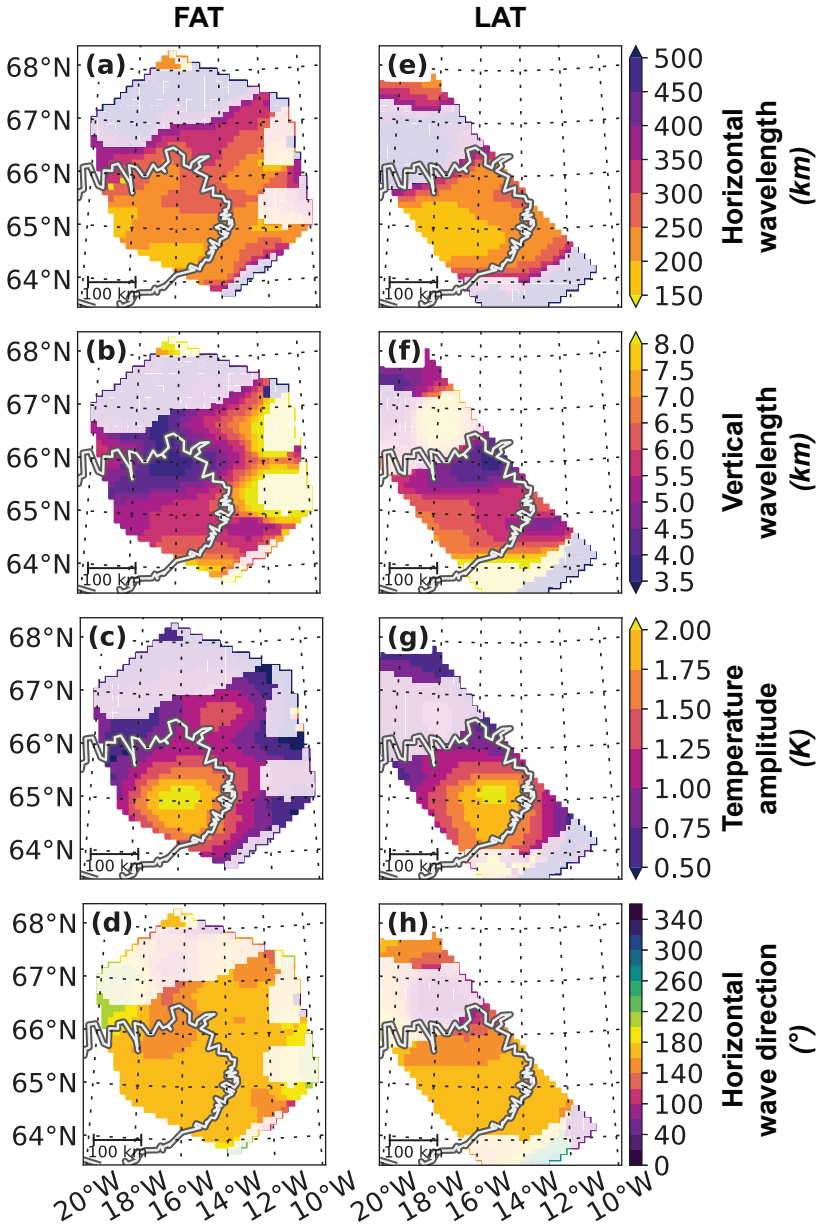

Figure 5.12: Wave parameters as obtained from the S3D fit with fitting cubes of 160 km x 160 km x 3.6 km at centre height of 11.5 km for FAT (Panels **(a-d)**) and LAT (Panels **(e-h)**). Non-significant fitting results with wavelengths above 2.5 times the cube size are shaded. Figure adapted from Krisch et al. (2018)

ters agree very well for both methods. The observed gravity wave has a horizontal wavelength of around 200 km, a vertical wavelength around 5.5 km, amplitudes up to 2 K and a horizontal wave direction of 160°. Thus, the wave vector is turned by 20° compared to the flight direction. The phase fronts are tilted southward and, thus, away from the flight path. Figure 5.10 predicted for such waves a wavelength reproduction of more than 90 % and an error in the estimation of the horizontal wave direction below 7.5°. This can be confirmed with the real measurement.

5.5 Conclusions

This chapter has investigated the capability of GLORIA to measure gravity waves with FAT and LAT. In contrast to FAT, which allows for the reconstruction of a large, cylindrical, 3-D volume, LAT can only reconstruct a band of 150 km around a banana-shaped vertical curtain parallel to the flight path (cf. Figure 3.3 a). The horizontal resolution of LAT is 30 km in flight direction and 70 km perpendicular to flight direction. The vertical resolution is on the order of 400 m. This volume and resolution are sufficient to properly derive all important wave parameters such as the horizontal and vertical wavelengths, the amplitude, and the wave direction for waves with phase fronts perpendicular to the flight path, horizontal wavelength above 200 km and vertical wavelength above 3 km. This is feasible due to the perfect alignment of wave phases and LOS and agrees well with earlier studies for other limb sounding concepts (Wu and Waters, 1996; McLandress et al., 2000; Ungermann et al., 2010a).

For LAT, the quality of the 3-D reconstruction strongly depends on the orientation of the wave with respect to the instrument. If the waves are slightly turned away from the perfect orientation the quality of the derived wave parameters is not strongly affected as long as the phase front is tilted towards the instrument. If the phase fronts are tilted away from the instrument, the retrieval will create artefacts which reduce the quality of the derived horizontal wave directions and both wavelengths. For waves with horizontal wavelength under 300 km, the amplitude error is larger for waves with phase fronts tilted away from the instrument than

for waves with phase fronts tilted towards the instrument. In general, the better the alignment of the wave phases and the LOS, the more information is attained by the tomographic retrieval. Thus, steeper waves can be derived with better accuracy than flatter waves. For steep waves with a horizontal to vertical wavelength ratio below 200 correct wave directions can be derived independently of the tilt. However, for waves turned by more than 40° compared to the perfect, perpendicular case, the reconstruction quality decreases drastically for all tested waves.

In summary, both tomographic methods can reproduce gravity wave structures much better, than traditional 1-D limb sounding retrievals. They do not show phase shifts and do not overestimate the horizontal wavelength, in cases where the phase fronts are not aligned with the LOS. For short scale waves FAT is preferable to LAT due to the higher spatial resolution of 20 km × 20 km × 0.2 km. The slightly better accuracy of 0.5 K for FAT compared to 0.7 K for LAT also makes FAT favourable for low amplitude waves. Furthermore, when the precise orientation of the wave cannot be predicted before the flight, FAT should be the method of choice, as no orientation dependent artefacts are introduced by the FAT retrieval. Nevertheless, for many other cases, LAT might be preferred due to its shorter acquisition time. Especially in cases where the wave field is not stable, LAT is the better choice. If LAT is the method of choice, one should try to plan the flight in a way that the flight path is as perpendicular to the phase fronts as possible.

For the very first gravity wave flight with GLORIA, which took place above Iceland on 25 January 2016, both measurement concepts were applied. The temperature perturbations derived from both methods agree very well with each other. The wave parameters determined with a sinusoidal fitting routine yield similar results. The results of the FAT are used in the following chapter, to study the sources and propagation characteristics of this gravity wave case.

6 The importance of 3-D wave propagation – a case study observed above Iceland on 25 January 2016

The gravity wave parameterisation schemes in current general circulation model (GCM) of the atmosphere assume gravity waves to propagate solely vertical. Several theoretical studies have highlighted that this simplification leads to a wrong location of momentum deposition and accordingly a misrepresentation of middle atmospheric circulations in these models (e.g. Sato et al., 2009; Kalisch et al., 2014; Garcia et al., 2017). However, measurements are still missing which are capable to confirm that oblique propagation can happen over large distances. This chapter presents observations of gravity waves measured with GLORIA above Iceland, which show such oblique propagation over large distances (see also Krisch et al., 2017). The synoptic situation which leads to the generation of these gravity waves and determines their propagation characteristics is described in Section 6.1. The GLORIA measurement results are presented in Section 6.2 and analysed for gravity waves in Section 6.3. The wave propagation is studied in Section 6.4. The discrepancies between oblique gravity wave propagation and simplified parameterisation schemes are investigated here as well. Section 6.5 compares the results of the propagation study to AIRS satellite measurements. The scientific findings are summarized and interpreted in Section 6.6.

6.1 Synoptic situation

On the measurement day 25 January 2016, gravity waves were excited by the interaction of low-level winds from a low-pressure system east of Greenland with the Icelandic orography (Figure 6.1 a). The low pressure system induced a southerly wind approaching the mostly east-west aligned mountain ridge of Iceland. The generated gravity waves will have phase fronts parallel to the main mountain ridge and will be tilted against the exciting background wind. Due to the complex orography of Iceland with the mentioned main mountain ridge but also many single mountain peaks spreading all over the island, a very complex gravity wave phase structure with interference patterns of different waves is expected (Chapter 2.4.1). The low pressure system and with it the generated southerly winds above Iceland did not change for more than 6 h around the measurement time according to ECMWF forecast data. Thus, a stationary wave pattern is expected.

Above 10 km altitude the zonal wind increases drastically with height and, thus, the horizontal wind turns from southerly to an almost westerly direction at 15 km (Figure 6.1 b). East of Scandinavia, the horizontal wind turns southward (Figure 6.1 b), which is probably caused by planetary waves interfering with the subtropical jet stream. It will be shown later, that both processes are important for the propagation characteristics of gravity waves.

Towards higher altitudes (Figure 6.1 c & d), the influence of the planetary wave decreases and the wind turns back to a westerly direction. These strong westerly winds in the middle stratosphere in winter are caused by the strong polar vortex and provide optimal conditions for westward propagating gravity waves to reach high altitudes (Chapter 1). On the flight day, the horizontal wind maximum shifts southward at higher altitudes to around 55° N at 30 km altitude.

Due to the expected complex but stationary wave pattern, FAT was chosen as optimal measurement concept for GLORIA. Thus, a hexagonal flight pattern was planned around the predicted location of the wave structure. The flight was planned for slightly before 12:00 UTC, because the NWP models used for flight planning predicted the wave to

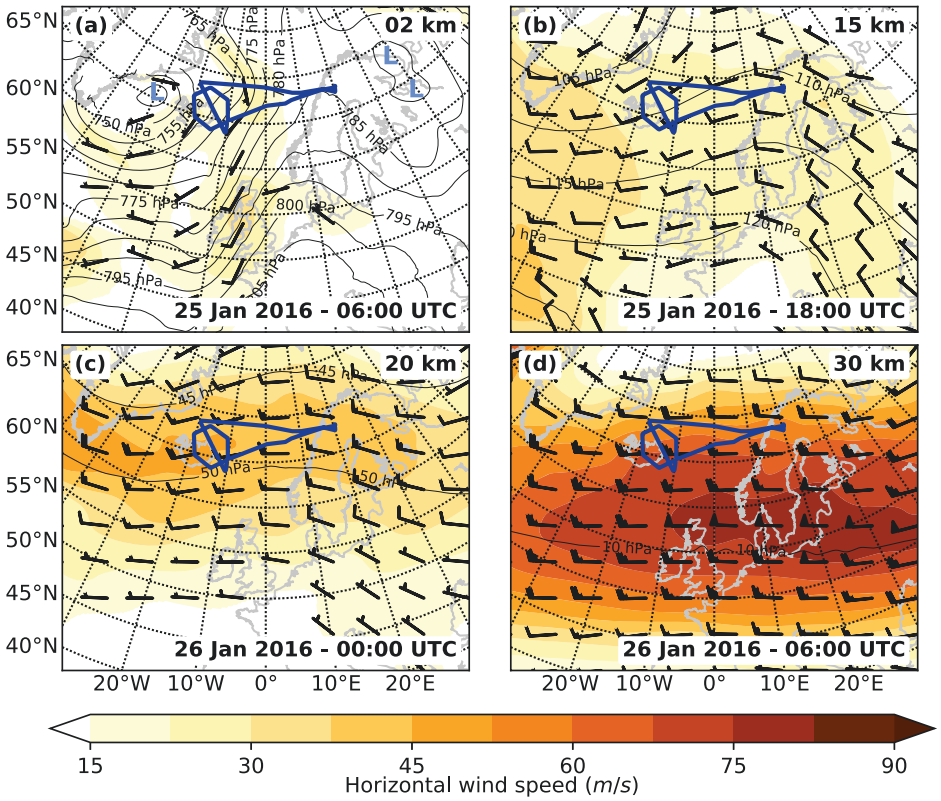

Figure 6.1: Synoptic situation on 25/26 January 2016. Shown are ERA5 horizontal wind (colour and barbs) and pressure (contour lines) fields at different altitudes and time steps. Low pressure systems are marked with a light blue "L". The altitude of the respective cross section is given on the top right of the panels, the model time at the bottom right. The dark blue line marks the flight path.

have maximum amplitude at this time. To take in-situ measurements and release dropsondes, the wave structure was not only encircled by a hexagon, but also crossed with a linear flight path almost perpendicular to the phase fronts. This additional linear flight leg provided the opportunity to compare the results of both measurement concepts LAT and FAT for a real measurement case. The results of this comparison were

already discussed in Chapter 5.4. The gravity wave structures found in both retrievals are similar. However, the FAT retrieval has a larger coverage area and a higher spatial resolution. Thus, in this chapter, only the FAT results will be used for the scientific interpretation.

In Chapter 5.4, a comparison of FAT (measurements taken during the hexagon) and LAT (measurements taken on the linear flight) results for this flight was presented.

6.2 GLORIA measurement results

The wave structure over eastern Iceland was first crossed perpendicular by a linear flight leg of 500 km length between 9:00 UTC and 10:00 UTC. On this leg, in-situ data of the wave structure were collected at flight altitude and dropsondes were released. This linear flight pattern was then encircled by a hexagon with 460 km diameter between 10:00 UTC and 12:00 UTC (Figure 6.1). The aircraft flight altitude during this time was between 12.5 km and 13.5 km. Towards low altitudes, the GLORIA measurements were limited by clouds reaching up as far as 9–10.5 km.

The retrieval diagnostics were already discussed in Chapter 5.4 and are summarized in Table 5.1. Figure 6.2 a shows a comparison of the retrieval results with in-situ measurements and analysis data from ECMWF. The retrieval results and model data were interpolated onto the in-situ-measurement locations. The GLORIA measurements agree well with the in-situ measurements. Some very small scales are beyond the spatial resolution of GLORIA. The ECMWF analysis data catches the main variations, but the temperature oscillations are not as strong as indicated by the in-situ measurements. GLORIA agrees well with the in-situ measurements also for fine structure and peaks, such as the strong peaks at 10:40 UTC or at 11:40 UTC. A comparison of the GLORIA retrieval results with dropsonde measurements is shown in Figure 6.2 b. The temperature profiles of GLORIA and the dropsonde agree within expectation with each other. However, small scale variations are again beyond the spatial resolution of the retrieval. These comparisons underline the high quality of the GLORIA measurement data.

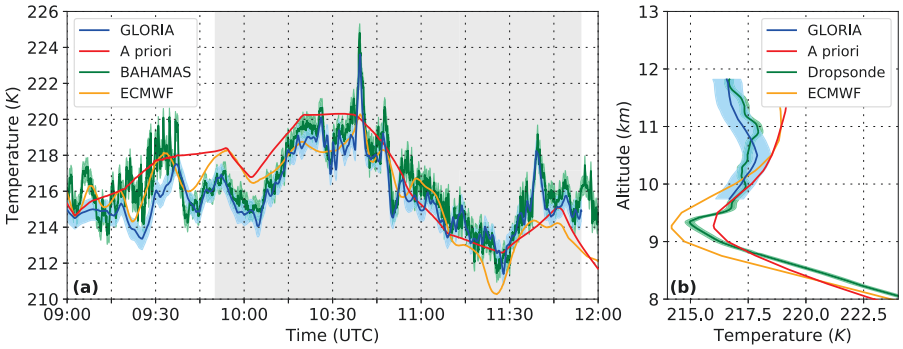

Figure 6.2: A comparison of the GLORIA retrieval results to in situ (Panel **(a)**) and dropsonde (Panel **(b)**) temperature measurements and ECMWF analysis from 12:00 UTC. The dropsonde was released at 09:35 UTC at 65.7° N, 13.2° W. The GLORIA retrievals were interpolated in space onto the flight path and the dropsonde locations, ECMWF data were quadrilinearly interpolated in space and time. Panel **(a)** is adapted from Krisch et al. (2017).

For gravity wave analysis, the retrieved temperature has to be separated into large scale background and small scale gravity wave perturbation. The gravity wave perturbation is determined using a Savitzky-Golay-filter (Savitzky and Golay, 1964), as described in detail in Chapter 4.1. The 3-D temperature perturbation inferred from the GLORIA observations is shown in Figure 6.3. This 3-D plot clearly reveals the complex structure of the wave field. The strongest temperature perturbations can be found in the southern part of the hexagon. There, the phase fronts, which are tilted towards the south, bend and change their vertical wavelength. Horizontal and vertical cross sections through the measurement volume (Figure 6.4) show more detailed how the wave structure varies with height and horizontal location. For instance, the phase fronts directly above Iceland (64° N to 65.5° N and 14° W to 18° W) are aligned east–west and tilted southwards as expected from the excitation mechanism. Further to the north-east (65° N to 67° N and 10° W to 14° W), the horizontal orientation of the phase fronts turns more into south-west to north-east. Visual inspection indicates horizontal wave-

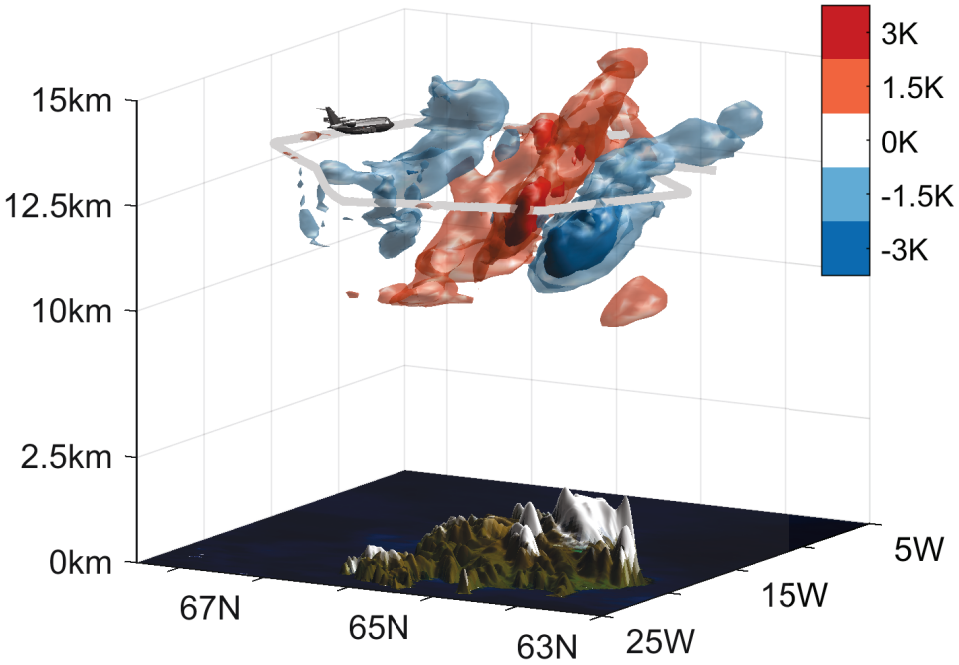

Figure 6.3: Tomographic retrieval for the research flight on 25 January 2016 over Iceland. Shown are isosurfaces of the temperature perturbations. The grey line around the retrieved 3-D pattern indicates the flight path. Figure from Krisch et al. (2017).

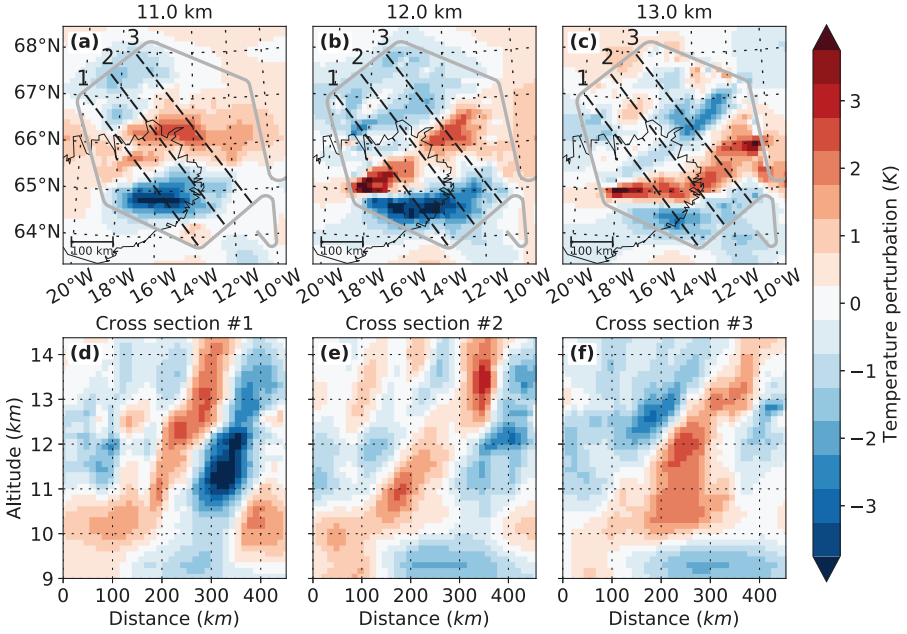

Figure 6.4: Horizontal **(a–c)** and vertical **(d–f)** cross sections through the 3-D volume shown in Figure 6.3. The grey line marks the flight path. The locations of the vertical cross sections are indicated by numbered dashed lines. Figure from Krisch et al. (2017).

lengths from 100 km up to 350 km inside the hexagon. The vertical wavelength of the waves is between 3 km and 6 km. The temperature perturbations range from ±4 K (in the southwest of the hexagon at an altitude of 12 km, 64° N to 65.5° N, and 14° W to 18° W) down to ±1 K (in the smaller-scale waves in the north-western part of the hexagon at 66° N to 68° N and 16° W to 20° W).

6.3 Wave characterisation

In order to further interpret the gravity wave structure and fully characterize it, wave parameters are derived using the S3D method described

in detail in Chapter 4.2. The S3D algorithm performs 3-D sinusoidal fits in small data cubes. Due to the expected wavelength ranges and the GLORIA measurement extent, analysis cubes with sizes of 160 km × 160 km × 3.6 km and a centre altitude of 11.5 km were chosen. The derived wave parameters are shown in Figure 6.5. As expected for a mountain wave, the horizontal wave direction (Figure 6.5 e) is perpendicular to the main mountain ridge orientation (Figure 6.5 f). Also, the horizontal wavelength of 200 km to 300 km agrees well with the ridge width. Further, the derived 3-D wave parameters are used to calculate the direction resolved vertical flux of horizontal pseudo-momentum (GWMF; Equation 2.33). Its direction is given by the horizontal wave direction (Figure 6.5 e), its amplitude is shown in Figure 6.5.

Integrating the GWMF over the horizontal extent of a gravity wave event leads to the total momentum, which determines the maximal drag this gravity wave event can exert on the background flow in coupling and dissipation processes. The fitted wave parameters in Figure 6.5 a–c are used to calculate the GWMF (Figure 6.5 d). The horizontal distribution of the GWMF clearly highlights two distinct wave packets: one with local GWMF of up to 50 mPa north of 66.2° N and one with local GWMF of up to 100 mPa south of 66.2° N. The GLORIA observations provide the horizontal variations of GWMF at 11.5 km altitude. This allows the integration over the corresponding area of the two events and to calculate the total momentum, a measure for the maximal drag this gravity wave event can exert on the background flow in coupling and dissipation processes. This is one of the main advantages with respect to 1-D wind observations, which can provide peak GWMF values but not the area for which these values are valid. The wave packet further south has a total momentum of 2.7 GN, the second wave packet further north only 0.4 GN. The total momentum of all the measured gravity waves above Iceland is 3.1 GN.

To classify this event, a comparison of all gravity wave events in January 2016 has been performed in the 6-hourly operational analyses of ECMWF. First the temperature background was isolated, as described in Chapter 4.1 and subtracted from the original field. The remaining temperature perturbations were analysed for gravity waves using the

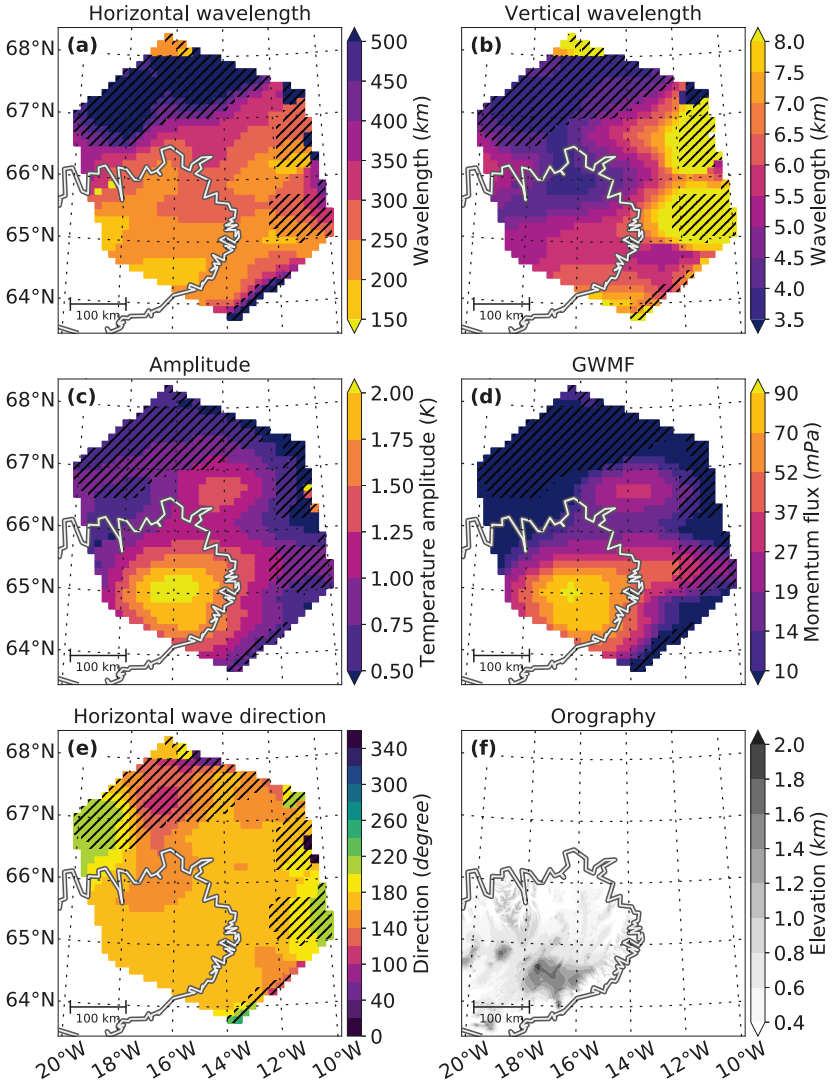

Figure 6.5: Three-dimensional sinusoidal wave fits of the GLORIA measurements in fitting cubes of 160 km × 160 km × 3.6 km at a centre height of 11.5 km. Non-significant fitting results with wavelengths above 2.5 times the cube size are hashed. These parameters are used to drive the GROGRAT model, the results of which are shown in Figure 6.8. Panel **(e)** shows the direction of the horizontal wave vector. Eastward direction corresponds to 90° and southward direction to 180°. Figure from Krisch et al. (2017).

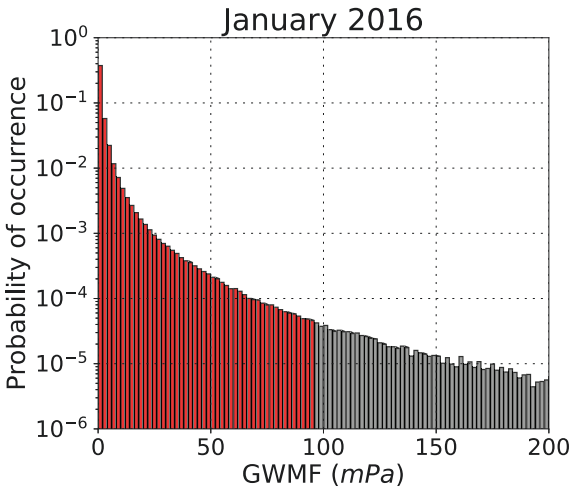

Figure 6.6: Probability of occurrence for gravity waves with specific momentum flux at 11.5 km altitude in a latitude band between 60° N and 70° N in January 2016 calculated from 6-hourly ECMWF operational analyses fields. Red marked values are found in the GLORIA measurements on 25 January 2016 above Iceland. Figure adapted from Krisch et al. (2017).

3-D sinusoidal fit algorithm described in Chapter 4.2. The GWMFs for all grid points between 60° N and 70° N were calculated. The GWMFs from all 124 analyses fields were combined to obtain the probability of gravity wave occurrence (Figure 6.6). Here, all GWMF values were considered independent of the horizontal and vertical wavelengths. Removing wavelengths larger than 2.5 times the cube size in order to filter less significant fits (not shown) induced no major changes in the general shape of the distribution. This indicates that gravity wave events with less certain fits do not bias the probability distribution.

For the gravity wave event over Iceland similar GWMF magnitudes were determined from the ECMWF analyses and from the GLORIA measurements. Thus, a comparison of the measurement results with the occurrence probability determined from the ECMWF analyses seems reasonable. According to Figure 6.6 the measured gravity wave event can be classified as a very strong case since the sum of all occurrence proba-

bilities of stronger events is well below 1 %. This occurrence frequency is in good agreement with Alexander et al. (2010), Hertzog et al. (2012), and Podglajen et al. (2016), who present satellite and super-pressure balloon measurements at somewhat higher altitudes.

6.4 Wave source and propagation

In order to identify the gravity wave source, the Gravity wave Regional Or Global RAy Tracer (GROGRAT; Chapter 2.3) is used. Backward ray tracing has already been used in previous studies to locate gravity wave sources (Wrasse et al., 2006; Preusse et al., 2014; Pramitha et al., 2015). In order to initialize a ray tracer, the wave must be fully characterized. This capability for a full wave characterization is the main improvement of the GLORIA observations compared to previous remote sensing observations of temperature. gravity wave parameters obtained from single vertical temperature profiles lead to a cone of potential source regions instead of a precise source location (Gerrard et al., 2004). This is the reason why gravity waves derived from conventional limb scanner measurements have not been interpreted in terms of backward ray tracing. Only the 3-D nature and accuracy of the GLORIA measurements allow for back-tracing to the precise source location. This is further highlighted by a discussion about the accuracy of back-tracing presented in Appendix A.

The S3D method, is based on the assumption that the fitting volume is filled by a homogeneous wave with a constant wave amplitude and a constant wave vector over the fitting volume. However, this assumption is only valid to a certain degree. In particular, one notices in Figure 6.4, that the direction of the horizontal wave vector and the vertical wavelength change with height. The GROGRAT model is used to estimate errors due to this change over height within the fitting volume (Figure 6.7). The model is initialised with the wave parameters determined by S3D (Figure 6.5). The development of these wave parameters over the hieght of the fitting cube (9.7–13.3 km) is calculated with GROGRAT. In Figure 6.7 the instantaneous value $\xi_{z=11.5\,\mathrm{km}}$ at the middle point of the

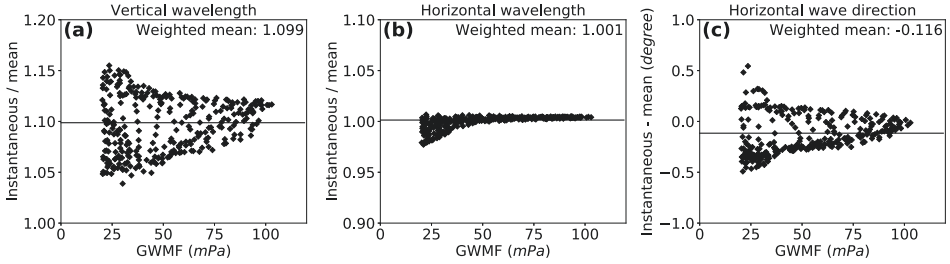

Figure 6.7: Comparison of mean values over the whole S3D fitting volume and instantaneous values in the middle for different wave parameters determined with GROGRAT. For all graphs GWMF weighted means are calculated and depicted as black lines. Figure adapted from Krisch et al. (2017).

fitting volume of each individual ray (corresponds to the initialisation parameters) is compared to an GWMF weighted average value $\overline{\xi}$ over the full height range of the S3D fitting volume; here ξ stands for either the vertical or horizontal wavelength or the horizontal wave direction. The mean value is comparable to the result the S3D fitting routine would detremine as monochromatic wave in this height range. The mean vertical wavelength in this case shows a systematic low bias of around 10 % compared to the instantaneous value in the middle (Figure 6.7a). For the horizontal wavelength (Figure 6.7b) and the horizontal wave direction (Figure 6.7c) no systematic bias could be identified. Due to these results, the vertical wavelengths from the sinusoidal fits were scaled by a factor 1.1, according to the determined bias, before being used for source identification and propagation studies.

Figure 6.8 a shows the backward ray traces using the scaled wave parameters. The measurement position (black crosses) has been defined as the centre point of the sinusoidal fitting cube. The ends of the ray traces, which are the probable source locations, are marked with red dots. The strengths of the gravity waves are expressed by the size of the red dots, which has been chosen according to the GWMF determined by the S3D fits. The source locations of the gravity waves, and in particular those of gravity waves with the highest GWMF values, gather around the main mountain ridge of Iceland. This ascertains the hypothesis, that

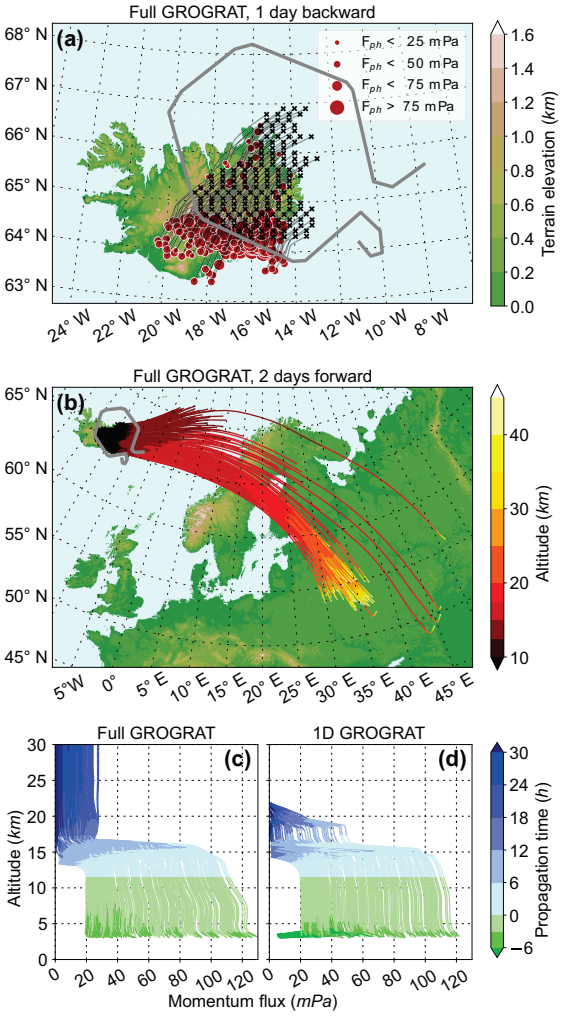

Figure 6.8: Ray traces calculated using the GROGRAT model. The starting positions of the rays are marked with black crosses and the grey line indicates the flight path. The size of the red circles in panel **(a)** indicates the GWMF at the end of the ray. Panel **(a)** shows the backward ray traces and panel **(b)** the forward ray traces, all starting at the measurement locations. Panels **(c)** and **(d)** show the change of GWMF with height for a full 4-D GROGRAT **(c)** model run and a solely vertical 1-D run **(d)**. Panels **(a)** and **(b)** are from Krisch et al. (2017).

the gravity waves were excited by the southerly wind approaching these mountains. The ray traces from the wave packet measured further in the north partly stop in the north of the island at single mountain peaks. As can be seen in Figure 6.8 c, the ray traces need between 3 h and 6 h to reach the ground. Thus, the a vertical group velocity of these gravity waves, which can also be calculated directly from the measurements and the horizontal wind speed at the surface (Equation 2.47), is between $2\,\mathrm{km\,h^{-1}}$ to $3\,\mathrm{km\,h^{-1}}$.

Forward ray tracing is used to examine the propagation of the gravity waves away from the measurement location (Figure 6.8 b). On the measurement day, the southerly wind turned into a strong westerly direction above 10 km, creating a vertical wind shear. In this wind shear the gravity waves started to propagate eastward. This is confirmed by the measurements: at 11 km (Figure 6.4 a) the gravity waves are mainly located above the eastern part of Iceland, while at 13 km (Figure 6.4 c) the phase fronts already stretch far across the ocean. The waves require about 1 day to propagate to an altitude of 20 km (Figure 6.8c). At the same time, they travel horizontally more than 2000 km away from their source and the measurement location (Figure 6.8 b).

Due to this large travel time and distance, the ray tracing calculations might be very sensitive to background and initiation conditions. To support the ray tracing results, the propagation of this wave packet is also investigated using ERA5 reanalysis data additionally to GROGRAT. ERA5 data has been chosen due to its hourly availability. Figure 6.9 shows cross sections through the ERA5 temperature perturbation field at different time steps along one arbitrary chosen GROGRAT ray trace initiated with GLORIA measurement data. In this way the gravity wave can be followed through time and space. The location and phase orientations of GROGRAT (grey dot and green line in Figure 6.9) follow nicely a wave structure observed in ERA5.

The gravity wave travels at low altitudes over the Atlantic towards Scandinavia. There, the horizontal wind changes from an eastward to a southward direction (compare also Figure 6.1 b) and takes the gravity wave with it. Due to this changing background wind, the wave is refracted and the wave vector changes its horizontal orientation from

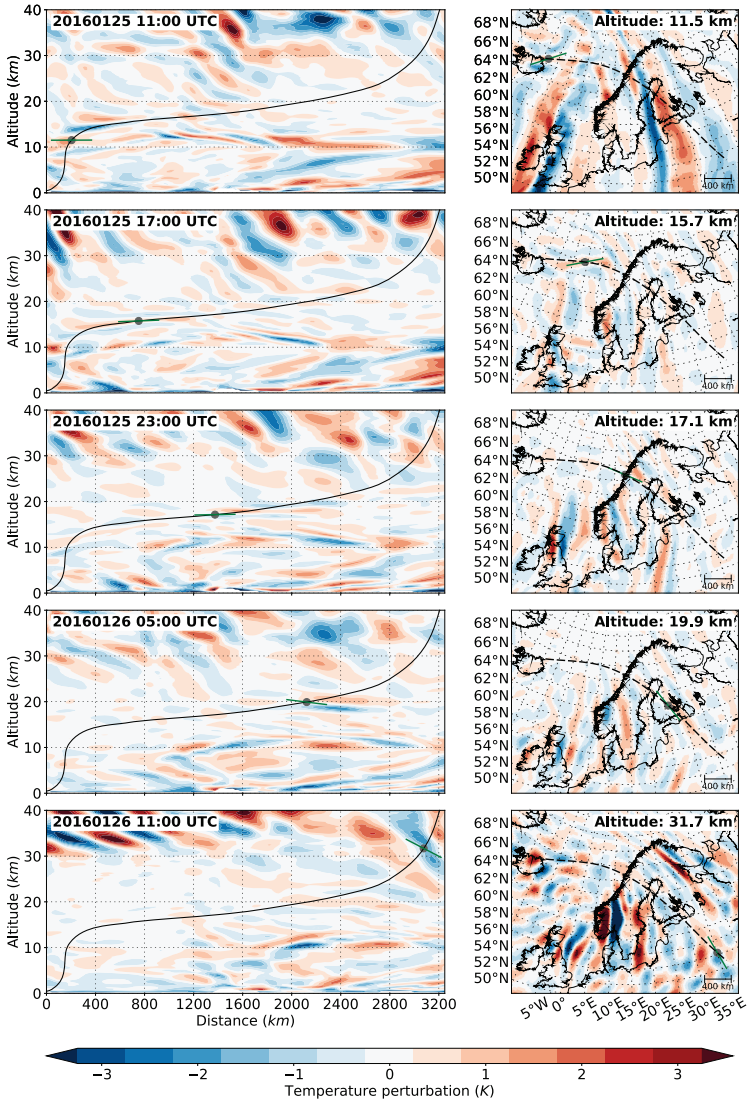

Figure 6.9: Cross sections through 6 hourly ERA5 temperature perturbations along an exemplary GROGRAT ray trace originating from GLORIA measurements. The left column shows vertical cross sections along the ray trace (black line). The grey dot marks the location of the ray trace at the respective time step of the model. The green line shows the orientation of the phase lines as predicted by GROGRAT. The right column shows horizontal cross sections at the altitude of the ray path at the respective model time.

southward to westward. At higher altitudes, the prevailing wind has an eastward direction (Figure 6.1 c & d). A horizontal background wind opposite to the wave vector is favourable for upward propagation. Due to the increase of the horizontal wind speed with altitude, the vertical wavenumber m decreases and, thus, the vertical wavelength increases. This can nicely be observed in the ERA5 model: Above Estonia, the phase fronts start to become steeper and reach up to higher altitudes (Figure 6.9).

According to Equation 2.13, the group velocity for constant k is proportional to:

$$c_{g,x} \propto \frac{1}{m} \qquad\qquad c_{g,z} \propto \frac{1}{m^2}. \tag{6.1}$$

Due to the decrease in m, the gravity wave starts propagating faster and more vertically. This can also be observed both in GROGRAT as well as in ERA5: The gravity waves propagate quickly upward into the westerly wind in the mid-stratosphere. At 31.7 km, ERA5 shows a complex wave pattern with many different wavelengths and wave orientations. Thus, it is difficult to clearly identify the wave originating from Iceland.

To mimic a typical gravity wave parameterisation scheme used in GCMs (McLandress, 1998), a second GROGRAT run (1D-GROGRAT) was performed with solely vertical propagation, time-independent background, and a horizontal wave direction constant with respect to altitude. In contrast to the full GROGRAT version (Figure 6.8 c), where the gravity waves propagate into the mid-stratosphere, the gravity waves in the simplified version dissipate below 20 km (Figure 6.8 d). Two processes might play a significant role here: first, in the 1-D GROGRAT version the gravity waves are not refracted and the wave vectors do not change their horizontal orientation with altitude. The westerly background winds at higher altitudes do not favour the propagation of gravity waves with wave vectors perpendicular to the wind direction. Second, in the full GROGRAT run, the gravity waves propagate horizontally away from the source. Hence, the gravity waves avoid the critical level positioned above the source location and more GWMF is transported to higher alti-

tudes. Global mountain wave modelling (Xu et al., 2017) suggests that this effect may prevail also on a global basis.

6.5 Comparison to AIRS measurements

The wave propagation study with GROGRAT and ERA5 showed, that the gravity waves measured by the GLORIA instrument need roughly a day to propagate to altitudes above 30 km. Thus, AIRS satellite measurements on 26 January 2016 taken on ascending orbits are chosen for the comparison. The temperature perturbations measured with the satellite are shown in Figure 6.10. According to the propagation study, the gravity waves reach the AIRS measurement altitude of 36 km at around 55° N and 30° E to 35° E. In this area, a wave structure with 1 K to 2 K

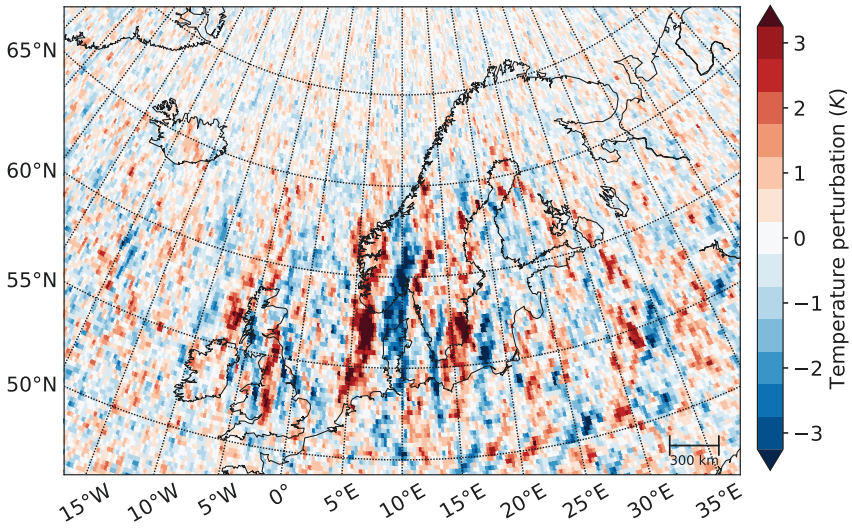

Figure 6.10: Temperature perturbations measured by the AIRS instrument on 26 January 2016 on ascending orbits. The picture consists of data from three different orbits: the easternmost overpass was around 10:15 UTC, the middle overpass around 11:50 UTC, and the westernmost overpass around 13:30 UTC.

amplitude can be observed in the AIRS temperature perturbations (Figure 6.10). This agrees reasonably well with amplitudes of 1 K to 5 K of the forward propagated gravity waves. Sinusoidal fits of the AIRS temperature perturbations (not shown) determine horizontal wavelengths of around 500 km and vertical wavelengths around 30 km. According to the forward ray tracing of the GLORIA measurements, waves with vertical wavelengths around 25 km and horizontal wavelengths between 250 km to 550 km are expected at the AIRS measurement altitude of 36 km. The temperature perturbation pattern of the ERA5 model (Figure 6.9 j) looks very similar to the one observed by AIRS (Figure 6.10). As mentioned above, ERA5 shows at this altitude a really complex wave pattern with superposition of waves with different scale and orientation. In the AIRStemperature perturbations the main wave structure above western Russia has a north-south phase orientation, whereas the gravity wave predicted by the ray tracer has a more north-west to south-east phase orientation. In the AIRS temperature perturbations a wave structure can be observed with such a horizontal orientation between northern Finland and western Russia. However, this wave is too weak to be analysed in detail.

6.6 Conclusions

In this Chapter, the first 3-D measurements of temperature perturbations induced by a gravity wave are presented. The 3-D measurements recorded by GLORIA, the first airborne implementation of a novel limb imaging technique, enabled the deduction of direction-resolved GWMF and the identification of two distinct wave packets. The retrieved 3-D wave vectors were used as input in the ray-tracing model GROGRAT, which highlighted the orography of Iceland as the most likely gravity wave source. Furthermore, upward from 11 km the wave packets propagate obliquely as is indicated in GLORIA observations and reproduced by the ray tracer. Using ERA5 reanalysis data in addition to the GROGRAT model helps to accurately follow the wave packet through space and time and reidentify it above western Russia. In this region a temper-

ature perturbation is also found in AIRS satellite measurements. However, the complexity of the wave field and the limited measurement resolution hinder a direct connection with the ray tracing results.

A comparison between the full GROGRAT model and a simplified 1-D version, which neglects oblique propagation and wave refraction, demonstrates the relevance of these processes for the GWMF deposition height. In the simplified version, all gravity waves deposit their momentum at an altitude of around 20 km, whereas the gravity waves in the full version were able to vertically propagate to the top of the model at 45 km and horizontally more than 2000 km away from their source, thus redistributing GWMF significantly. Neither a realistic orientation of the wave vector and, thus, wave refraction, nor oblique gravity wave propagation are incorporated in gravity wave parameterisations used in current climate and weather prediction models (McLandress, 1998; Alexander and Dunkerton, 1999; Richter et al., 2010; McLandress et al., 2012; Garcia et al., 2017). However, both processes are context of several studies aiming to improve gravity wave parameterisations (Preusse et al., 2009b; Sato et al., 2009; Kalisch et al., 2014; Amemiya and Sato, 2016; Ribstein and Achatz, 2016; Garcia et al., 2017). The present study provides a strong motivation to finally implement these processes in current climate and weather prediction models, especially as this could close gaps of GWMF in regions with sparse sources (McLandress et al., 2012) and reduce the cold-pole bias of climate and weather prediction models in the lower stratosphere (Garcia et al., 2017).

7 The importance of non-linear processes – a case study observed above Scandinavia on 28 January 2016

Several theoretical studies suggest, that non-linear processes can lead to a severe momentum deposition of gravity waves even in the absence of dissipation, saturation and breaking (Buehler and McIntyre, 2003; Eberly and Sutherland, 2014; Boeloeni et al., 2016). Linear gravity wave models, which are often used to identify gravity wave sources and study the propagation of gravity waves, completely neglect those non-linear interactions of gravity waves and the background flow. This chapter tries to analyse, how meaningful the results of those linear gravity wave models are and how well their predictions agree with observations (see also Krisch et al., 2020). For this investigation, the propagation of a gravity wave above southern Scandinavia, which was measured at different altitudes by GLORIA and AIRS, was studied using the linear gravity wave model GROGRAT. The synoptic situation influencing the gravity wave propagation is outlined in Section 7.1. Section 7.2 presents the GLORIA measurements taken on the flight. The results of GROGRAT are presented and examined in Section 7.3 and compared to the AIRS measurements in Section 7.4. The scientific findings are summarized in Section 7.5.

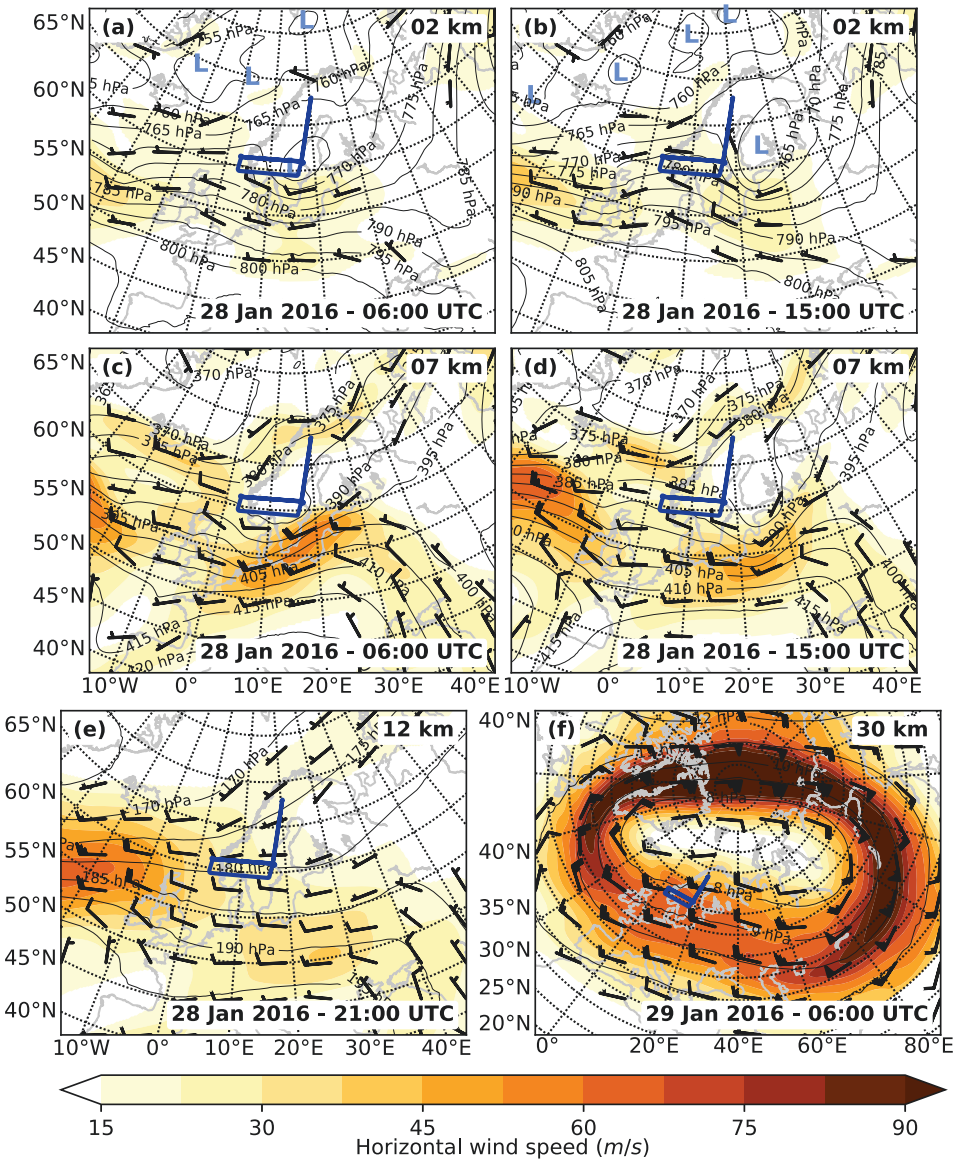

Figure 7.1: Synoptic situation on 28/29 January 2016. Shown are ERA5 horizontal wind (colour and barbs) and pressure (contour lines) fields at different altitudes and time steps. Low pressure systems are marked with a light blue "L". The altitude of the respective cross section is always given on the top right of the panel, the model time at the bottom right. The dark blue line marks the flight path. Figure from Krisch et al. (2020).

7.1 Synoptic situation

For the 28 January 2016, gravity waves were predicted above southern Scandinavia. One prominent source of gravity waves in this region are the Scandinavian Mountains also called Scandes. The Scandes are a mountain ridge with north-south orientation stretching along the complete west coast of Scandinavia. They are up to 400 km wide and their highest mountain is 2469 m. In the southern part, where the HALO flight path was located (Figure 7.1 blue line in all panels), their mean width is around 250 km and their mean elevation is on the order of 1800 m. Due to the ridge width, a typical horizontal wavelength of gravity waves generated by this orography should be on the order of 400 km. According to Equation 2.39, the minimum wind to generate mountain waves with a horizontal wavelength of 400 km at a latitude of 60° is $8\,\mathrm{m\,s^{-1}}$. However, waves generated with such slow wind speeds would have very low vertical group velocities and small saturation amplitudes. A gravity wave with a horizontal wavelength of 400 km which is generated by a flow over orography with $17.5\,\mathrm{m\,s^{-1}}$ at 60° latitude would have a vertical group velocity of $0.86\,\mathrm{km\,h^{-1}}$ and would need 14 h to propagate to an altitude of 12 km (Equation 2.47). Thus, to measure these orographically generated gravity waves with GLORIA at 20:00 UTC, the generating wind should be at least $17.5\,\mathrm{m\,s^{-1}}$ at 06:00 UTC. This, is the case (Figure 7.1 a). Gravity waves with smaller horizontal wavelengths would propagate faster and need less time to propagate to the flight altitude. As the orography of the Scandes is composed of mountain ridges with many different heights and widths, a complex wave structure with many different horizontal wavelengths below 500 km is expected.

In the morning of the measurement day 28 January 2016, a low pressure system evolved over southern Scandinavia, which then moves slowly eastward (Figures 7.1 a & b). This low pressure system forces the eastward jet stream in the upper troposphere to slow down and diverge. Thus, a jet exit region is created over the North Sea between Scandinavia and Great Britain (Figure 7.1 c). This jet exit region is following the low pressure system slowly eastwards. Such a jet-exit region also is a prominent source of gravity waves (c.f. Chapter 2.4.2). In the afternoon

of 28 January, the jet-exit region is located above southern Scandinavia (Figure 7.1 d). Hence, the observed gravity waves may be a mixture of waves generated by orography and this jet-exit region.

The divergence is also connected with a low tropopause altitude and accordingly a low cloud top height of around 8 km above southern Scandinavia, which results in good measuring conditions for GLORIA. However, it also sharpens the tropopause, which can lead to partial reflection of gravity waves. The horizontal wind keeps its eastward orientation at higher altitudes (Figures 7.1 e & f) as the maximum of the circumpolar jet stream on this side of the pole is located just south of Scandinavia. This provides favourable conditions for vertical gravity wave propagation.

7.2 GLORIA measurement results and wave characterization

Jet generated gravity waves are not necessarily stationary. Hence, linear-flight tomography was chosen as measurement strategy. The gravity wave structure was probed with multiple, 700 km long, linear flight legs crossing southern Scandinavia in zonal direction. To study the interaction of the gravity wave with the tropopause, two flight legs were positioned below and two flight legs above the tropopause. Both lower legs were performed at 61° N and were mainly dedicated to in situ and water vapour observations by BAHAMAS and WALES (Table 3.2). GLORIA did not measure during these low level legs, as this part of the flight was mainly inside or just above clouds. At 20:00 UTC, HALO ascended to almost 13 km and performed an east-west leg at 59.5° N. This flight leg was placed further to the south, so GLORIA could look on the earlier performed, lower flight legs, which should allow comparisons with in situ and lidar data. Unfortunately, the cloud cover prohibited GLORIA during most of the flight leg to collect measurements down to the former flight altitude. At the westernmost point of the leg at around 21:00 UTC, HALO ascended further to ≈13.5 km altitude, went back to the original

Table 7.1: Diagnostics of the tomographic retrievals of the measurement flight on 28 January 2016. A detailed description how these parameters are calculated can be found in Chapter 3.2.2.3.

Quantity	Southern leg	Northern leg
Horizontal resolution along flight track	30 km	30 km
Horizontal resolution across flight track	70 km	70 km
Vertical resolution	400 m	400 m
Accuracy	0.7 K	0.7 K
Precision	0.05 K	0.05 K

latitude of 61° N and performed a last west-east leg before returning to the campaign base at Kiruna, Sweden.

The GLORIA measurements from the southern and northern flight legs in the stratosphere, were used to perform two separate LAT retrievals. The retrieval diagnostics are summarized in Table 7.1. The GLORIA measurements agree well with the in-situ measurements taken during the flight leg which was used for the respective retrieval (Figure 7.2). Some very small scales are beyond the spatial resolution of GLORIA. In-situ measurements taken on the southern (northern) flight leg differ stronger from the GLORIA retrieval using only measurements from the northern (southern) flight leg (non-shaded areas in Figure 6.2). However, the main wave structures are still captured. This can be explained by the temporal difference between the two legs and the location of the tangent points of the respective retrievals: The tangent point altitude decreases with distance to the flight path. Hence, the tangent points of measurements taken on the southern flight leg are below flight altitude at the location of the northern flight leg and vice versa. A comparison of in-situ measurements taken for example on the northern flight leg with the temperature retrieval using measurements from the southern flight leg, thus relies on vertical and/or horizontal data extrapolation. The ECMWF analysis catches the main variations, but the temperature oscillations are not as strong as indicated by the measurements. Sometimes the wave structure appears to be shifted in time/space compared to GLORIA and in-situ measurements (e.g., between 20:30 UTC

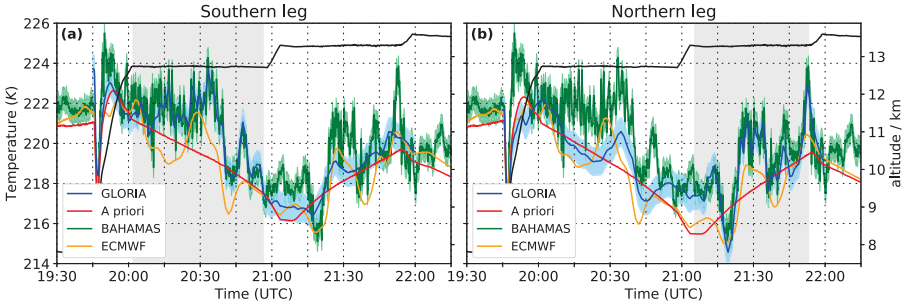

Figure 7.2: A comparison of the GLORIA retrieval results to in-situ-temperature measurements and ECMWF operational analyses. The GLORIA retrievals were interpolated in space onto the flight path, ECMWF data were quadrilinearly interpolated in space and time. The shaded area indicates which GLORIA measurements were included in the respective retrieval. Figure adapted from Krisch et al. (2020).

and 20:45 UTC).

The retrieved temperatures are separated into background state and remaining wave perturbation using the scale separation method described in Chapter 4.1. The remaining temperature perturbations can be seen in Figure 7.3. The left column shows the temperature perturbations derived from tomographic measurements performed during the southern flight leg and the right column shows those taken on the northern flight leg. Both retrievals show a prominent wave structure with around 400 km horizontal and around 6 km to 7 km vertical wavelength. This large scale structure is perturbed by a smaller scale wave with probably longer vertical but shorter horizontal wavelength. The smaller scale wave is more prominent in the east at lower altitudes (Figure 7.3 a & b) and in the west part at higher altitudes (Figure 7.3 c & d). The larger scale wave has strongest amplitudes between 8° E and 12° E.

Even though the main characteristics are similar for the observations during both legs, there are some differences between them. The waves seem to have slightly different horizontal orientations: The main gravity wave structure observed on the southern leg between 60° N and 62° N has north-south oriented phase fronts (Figure 7.3 a & c), whereas the

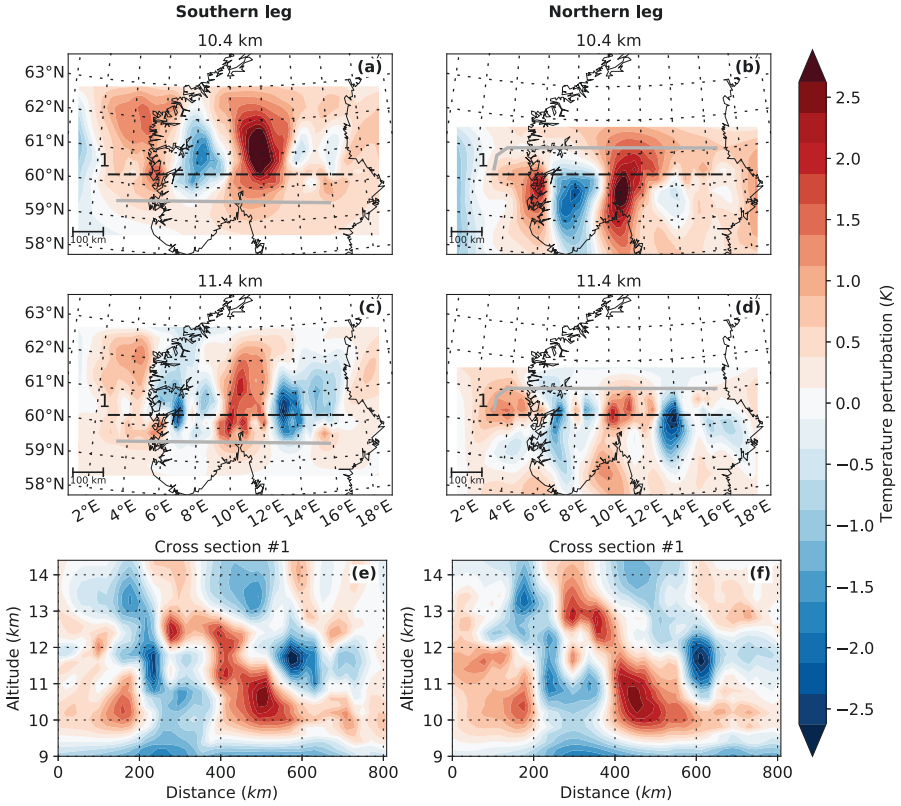

Figure 7.3: Temperature perturbations of the GLORIA tomographic retrieval for the flight on 28 January 2016 over southern Scandinavia. Shown are horizontal (Panels **(a-d)**) and vertical (Panels **(e & f)** cross sections. The vertical cross sections are along the dashed lines in (Panels **(a-d)**). The grey line indicates the flight path. The left column shows results from measurements taken on the southern flight leg, the right column results from measurements taken on the northern flight leg. Figure from Krisch et al. (2020).

phase fronts of the gravity wave structure observed on the northern flight leg between 59° N and 60.5° N seem to be turned slightly and have a north-north-east to south-south-west alignment. Also, the horizontal wavelengths of the main wave component and the steepness of the phase fronts seem to differ slightly between the two legs.

Due to the superposition of different gravity waves, the sinusoidal fit is challenging and the results partly depend on the chosen cube size. To determine first the large scale wave with horizontal wavelength around 400 km, a 400 km × 250 km × 4 km cube size has been chosen. In the horizontal, this cube size is on the order of the wavelength, in the vertical the cube size roughly equals the measurement extent. To capture the spatial variation of the wave amplitude, refits of amplitude and wave phase, using the previously determined wave vector $\boldsymbol{k}$, have been performed in fitting cubes of 100 km × 250 km × 1 km. The different horizontal directions observed during both legs are also indicated by the result of the sinusoidal fit (Figure 7.4). Here, the wave orientation changes from $\varphi = 270°$ measured during the southern flight leg to $\varphi = 290°$ measured during the northern flight leg. The horizontal wavelength increases slightly on both legs from west to east. During the southern leg, the waves also decrease in steepness (increasing vertical wavelength) from west to east, which can also be seen in the vertical cross section of the temperature perturbations (Figure 7.3 e): At 200 km distance along the cross section, the waves have shorter horizontal and longer vertical wavelengths than at 600 km. According to the sinusoidal fit, the waves have highest amplitudes between 12° E and 14° E. There, the waves observed during the northern flight leg are in general steeper than those observed during the southern flight leg, a property already noticed in the temperature perturbations above.

After these large scale waves have been identified, they can be subtracted from the temperature perturbation fields. The remaining fields are shown in Figure 7.5. Here, waves with amplitudes up to 1.5 K with short horizontal and long vertical wavelengths can be seen. However, the wave structure is quite complex and no single monochromatic wave can be identified by eye. Instead, the structure has very localised maxima and a bit of a chess board pattern. This might hint to a superposition

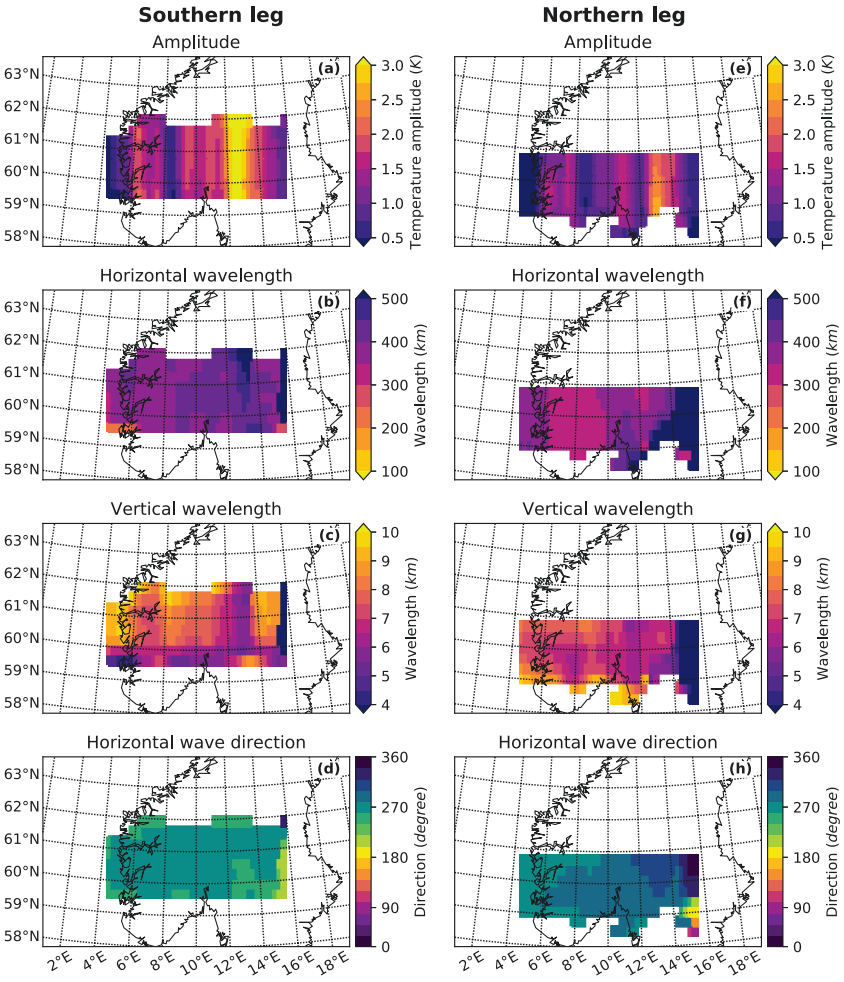

Figure 7.4: Three-dimensional sinusoidal wave fit of the GLORIA measurements at a centre height of 11.4 km in fitting cubes of 400 km × 250 km × 4 km with a tangent point weighting according to Sec. 4.2. In order to capture the spatial variation of the amplitudes, an amplitude and phase refit has been performed in fitting cubes of 100 km × 250 km × 1 km. The fitting results are used to drive the GROGRAT model, the results of which are shown in Figure 7.6. Panel **(b)** shows the direction of the horizontal wave vector. Eastward direction corresponds to 90° and southward direction to 180°. Figure from Krisch et al. (2020).

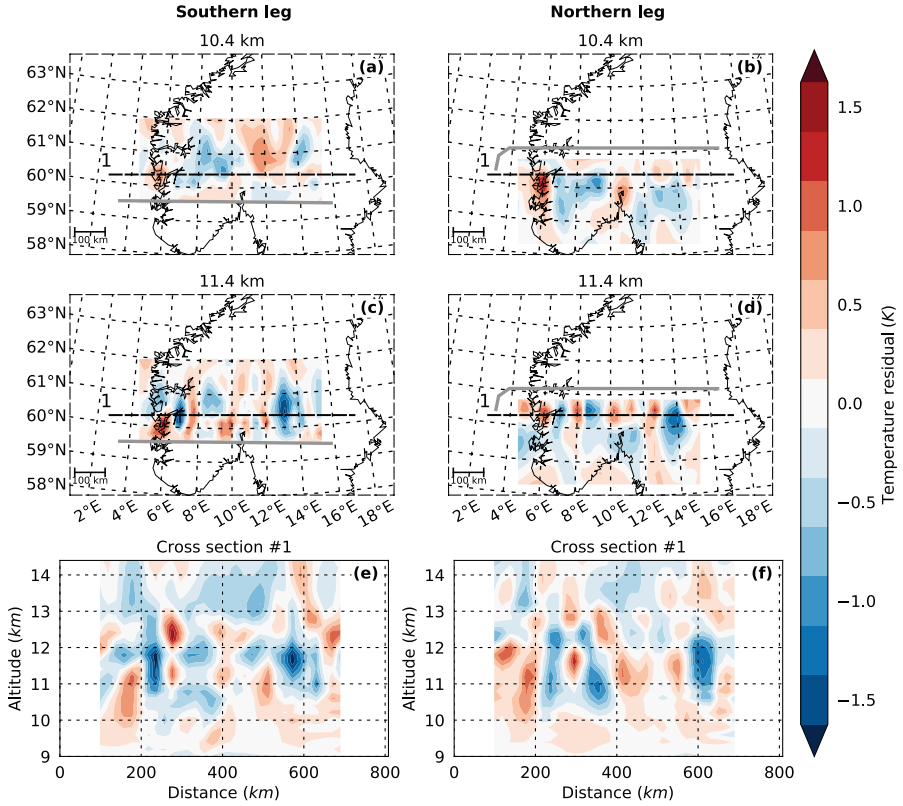

Figure 7.5: Remaining temperature perturbations of the GLORIA tomographic retrieval after subtraction of the wave of Figure 7.4. Shown are horizontal (Panels **(a-d)**) and vertical (Panels **(e & f)**) cross sections. The vertical cross sections are along the dashed lines in Panels **(a-d)**. The grey line indicates the flight path. Figure from Krisch et al. (2020).

of multiple wave packets propagating both upwards and downwards. For such an overlap of upwards and downwards propagating waves, the spectral analysis is challenging. Currently, the fit results strongly depend on the chosen cube size which directly shows, that further synthetic test have to be performed before applying the method to this wave field.

Not only the main wave component changes in time. The phases of the small wave component shifts a tiny bit further to the east at an altitude of 11.4 km from southern to northern leg. This can be seen, for example at the little maximum at 8° E which is located slightly to the left of the meridian for the southern retrieval, whereas it is on the meridian for the northern retrieval. The two little maxima between 10° E and 11°E show a similar behaviour. These differences explain, why a joint retrieval using measurements of both legs simultaneously did not converge properly.

7.3 Wave sources and propagation

In order to identify the sources of the first wave component, the Gravity wave Regional Or Global RAy Tracer (GROGRAT; Chapter 2.3) is used. The derived gravity wave parameters (Figure 7.4) are used together with a background field generated from smoothed 6-hourly ECMWF analysis fields. Most of the backward rays and especially those with highest GWMF values are traced back to the Scandes (Figure 7.6 a). However, other rays and especially those not reaching the surface origin from a wide spread area west of Scandinavia. According to the ERA5 model (Section 7.1) a jet-exit region was moving over this area during the course of the 28 January 2016, which might be a source for these gravity waves. At the measurement altitude, the wave parameters of waves not originating from the surface (Figure 7.6 c-d black crosses) do not differ from those generated by orography.

The sources of these waves are examined further by a comparison of the ray-tracing results with ERA5 (Figure 7.7). One ray trace has been chosen exemplary and ERA5 cross sections are plotted along its path. In the early morning at 3:00 UTC, the gravity wave predicted by the ray tracer does not agree well with ERA5. Thus, the source of the

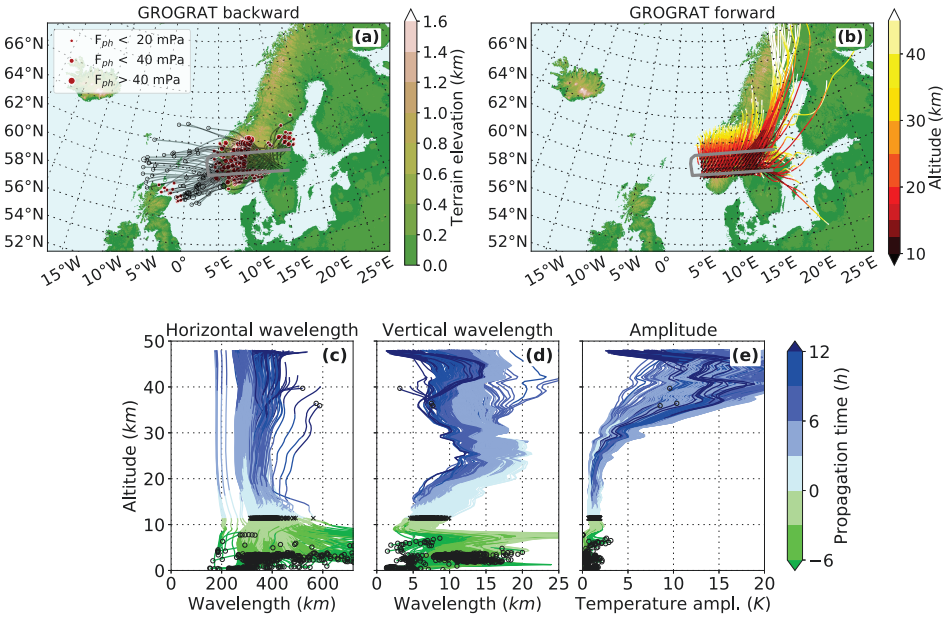

Figure 7.6: Ray traces calculated using the GROGRAT model. Panel **(a)** shows the backward ray traces and Panel **(b)** the forward ray traces. Panels **(c-e)** show the change of wave parameters with height. The end points of backward rays which do not reach the surface are marked with an open circle, rays which reach the surface are indicated with a red dot. The size of the circle marks the strength of the wave (GWMF). In Panels **(c-e)**, the crosses indicate which wave properties the waves not reaching the surface have at flight altitude. Figure from Krisch et al. (2020).

wave might be further towards the measurement location. However, at 9:00 UTC a wave structure with similar orientation as predicted by the ray tracer can be found just in front of the Scandinavian coast in ERA5. This location of the wave in front of the coast, as well as the orientation of the wave which does not agree with the alignment of the main mountain ridge, hint to an excitation by a non-orographic source. At 15:00 UTC, a wave field located directly above the mountains and reaching up to 20 km appears in ERA5. However, the wave structure at

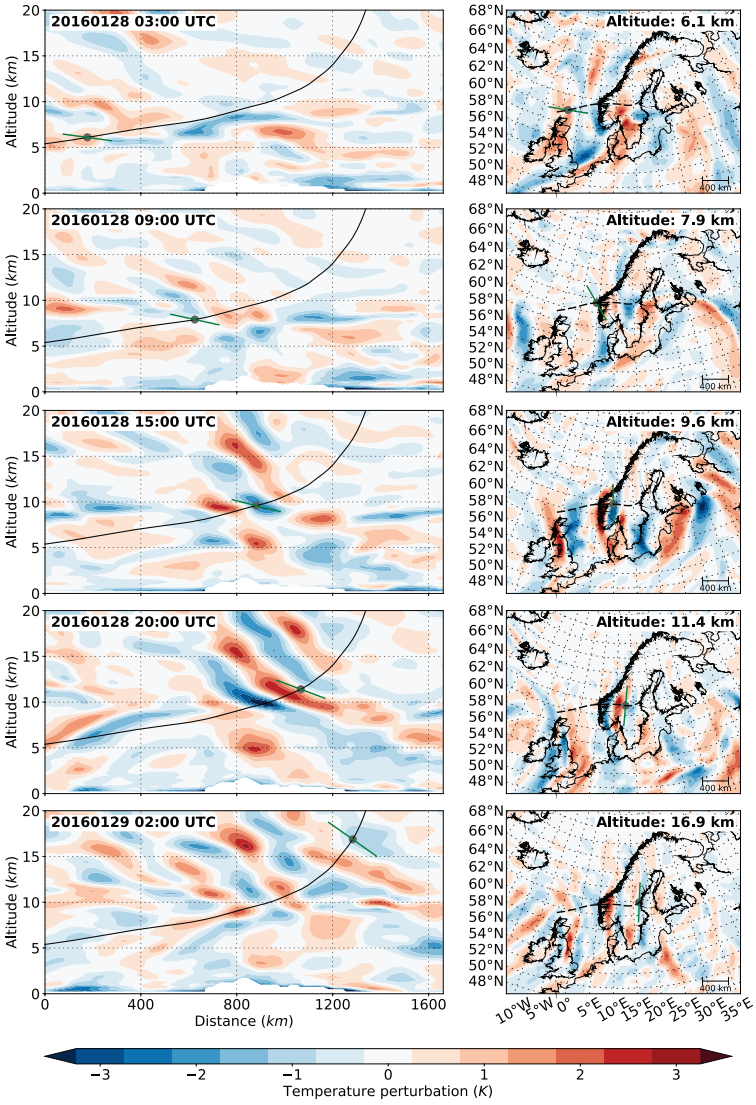

Figure 7.7: Cross sections through different ERA5 temperature perturbations along an exemplary GROGRAT ray trace originating from GLORIA measurements. The left column shows vertical cross sections along the ray trace (black line). The grey dot marks the location of the ray trace at the respective time step of the model. The green line shows the orientation of the phase lines as predicted by GROGRAT. The right column shows horizontal cross sections at the altitude of the ray path at the respective model time. Figure from Krisch et al. (2020).

10 km altitude, which is exactly the location of the traced wave, differs in steepness from the field above and below. At 20:00 UTC, the time of the measurement flight, this slightly flatter structure has propagated a bit further. In the horizontal cross section, the blue phase front has an orientation more or less parallel to the main mountain ridge below 62° N. North of 62° N, the orientation changes and agrees well with the prediction of the ray tracer. At 2:00 UTC on the following day, one can now clearly identify different wave packets both in the horizontal as well as in the vertical cross section. The wave packet followed by the ray tracer is less steep than the waves above the mountains and is now located further to the east. This comparison suggests, that a non-orographic wave packet has travelled through a orographically excited wave above the Scandes during the course of the late afternoon and night of the measurement day. This again explains why the retrieval of both flight legs simultaneously did not work. The wave field was not sufficiently stationary.

Forward ray tracing shows, that the waves propagate slightly northward and to high altitudes (Figure 7.6 b). The temperature amplitude increases with height and reaches values between 10 K to 30 K just below 40 km. The waves need between 3 h to 12 h to propagate to these altitudes. The exact propagation time strongly depends on the wavelength: gravity waves with long vertical and short horizontal wavelengths (steep waves) are faster than those with shorter vertical and longer horizontal wavelengths. The horizontal wavelengths stay on the order of 200 km to 400 km. The vertical wavelengths increase to around 5 km to 15 km at an altitude of 20 km and stay more or less constant above. This doubling of the vertical wavelengths is caused by a doubling of the horizontal wind from 30 m/s at 12 km up 60 m/s above 20 km altitude (Figure 7.1).

7.4 Comparison to AIRS measurements

To investigate, how accurate these forward ray-tracing calculations of the GROGRAT model are, the propagation results are compared to Atmospheric Infrared Sounder (AIRS) satellite measurements. As the waves

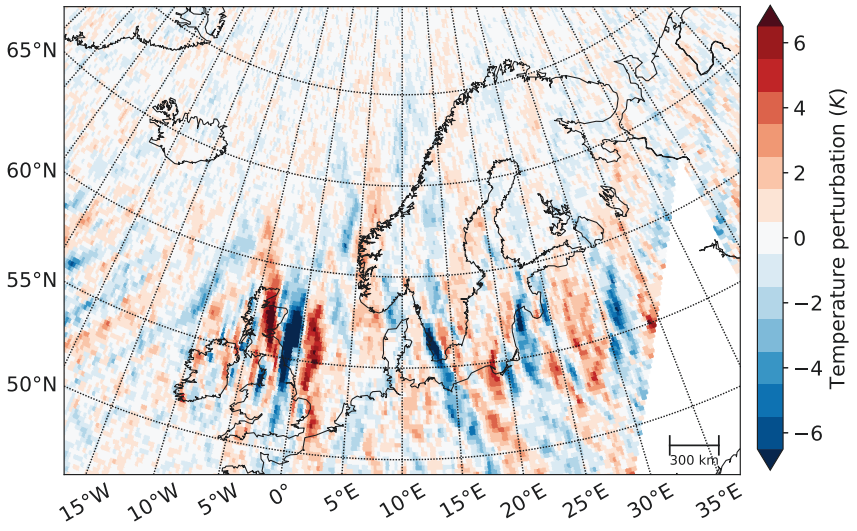

Figure 7.8: Temperature perturbations of the AIRS retrieval for the descending orbits with equator crossing time at 01:30 LT on 29 January 2016. Figure from Krisch et al. (2020).

measured by GLORIA propagate up to altitudes of 40 km, such a comparison with satellite measurements appears feasible. According to the ray-tracing results, the gravity waves take between 3 h and 12 h to propagate up to 36 km. Thus, AIRS measurements of the descending orbit on 29 January 2016 were chosen for the comparison (Figure 7.8). These measurements over Scandinavia were taken between 01:00 UTC and 03:00 UTC and, thus, about 3 h to 6 h after the HALO flight. The forward ray tracing predicts gravity wave amplitudes between 10 K and 30K above middle and northern Scandinavia (Figure 7.6 e). The vertical wavelengths are predicted to be between 5 km and 15 km (Figure 7.6 d). According to the AIRS observational filter (Figure 3.5) such gravity waves are underestimated in amplitude by more than 80 % and overestimated in vertical wavelength by at least 30 %. Thus, these waves should appear only weakly in the AIRS measurements and with wavelengths around 20 km. Sinusoidal fits of the AIRS data show high am-

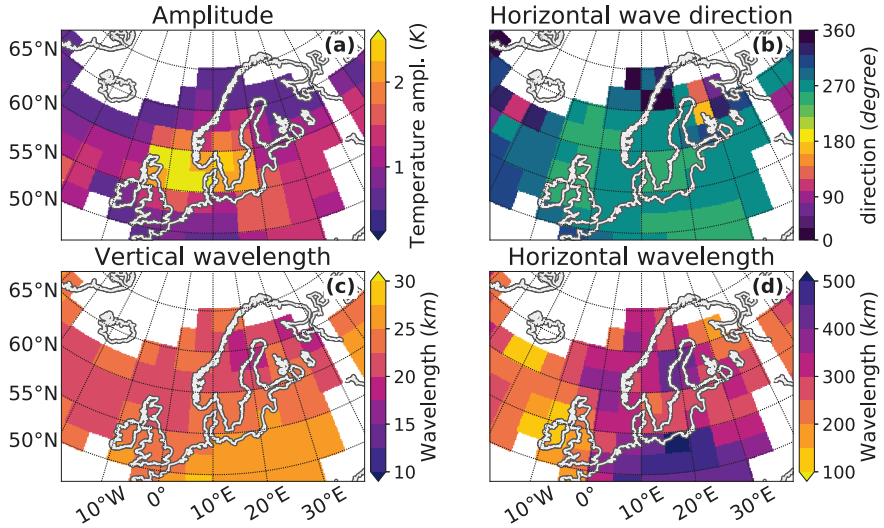

Figure 7.9: Three-dimensional sinusoidal wave fit of the AIRS measurements in fitting cubes of 300 km × 250 km × 20 km at a centre height of 36 km. Figure from Krisch et al. (2020).

plitudes above the southern tip of Scandinavia and the North Sea (Figure 7.9). Above middle and northern Scandinavia, as expected, very low amplitudes are identified with vertical wavelengths on the order of 20 km. Further, the horizontal wavelengths derived from the AIRS measurements comply well with the GROGRAT model results.

The influence of the AIRS observational filter on these gravity waves is studied in more detail using ERA5 model data. Similar to the GLORIA sensitivity study, the influence of the AIRS measurement concept on a certain gravity wave structure can be investigated by multiplying an AIRS averaging kernel matrix with a temperature perturbation field. Thus, the ERA5 temperature field is first separated into small scale gravity wave perturbations and large scale background motion (see Chapter 4.1). Each profile of the gravity wave perturbation field is then multiplied with an AIRS averaging kernel matrix. The results are shown in Figure 7.10. At an altitude of 27 km the ERA5 field is filled with different gravity waves with amplitudes on the order of 3 K

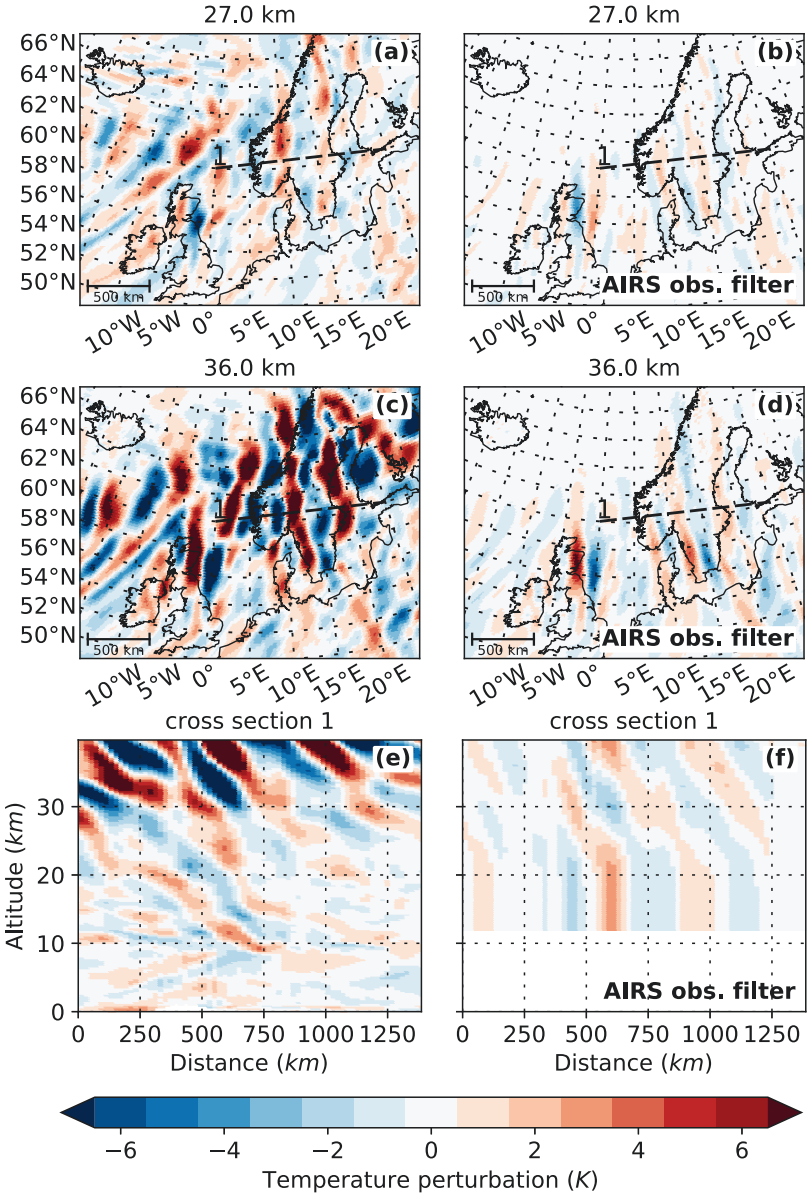

Figure 7.10: ECMWF forecast initialized on 29 January 2016 midnight for 3:00 UTC and the influence of the AIRS observational filter. The left column shows the original ECMWF forecast data, the right column shows what remains if the model data is multiplied with the AIRS averaging kernel matrix. Figure adapted from Krisch et al. (2020).

(Figure 7.10 a). After applying the AIRS observational filter, only small parts of the wave structure remain with strongly underestimated amplitudes (Figure 7.10 b). Also the complex wave structures are replaced by mainly monochromatic wave packets. A similar picture can be seen at 36 km altitude (Figures 7.10 c & d). Additionally to this amplitude underestimation, the vertical cross sections reveal the overestimation of the vertical wavelengths (Figures 7.10 e & f), which was already predicted by the observational filter. Especially the flat waves on the top right in Panel e with vertical wavelengths on the order of 10 km appear with very low amplitudes and much steeper phase fronts in the AIRS simulation (Figure 7.10 f). At altitudes below 20 km, almost no information content remains in AIRS retrieval and, thus, the temperature structure is vertically extrapolated downwards.

A comparison of these simulated AIRS measurements (Figure 7.10 d) with the real AIRS measurements (Figure 7.8) show an excellent agreement. However, due to the observational filter, the gravity waves observed by GLORIA and propagated forward by GROGRAT are only barely visible for AIRS.

7.5 Conclusions

In this Chapter, a gravity wave field above southern Scandinavia was examined with respect to its sources and propagation paths. Measurements taken with GLORIA on the 28 January 2016 revealed a complex wave field composed of multiple wave packets with different spatial structure. The wave field was not time invariant, which made two separate LAT retrievals necessary. The GROGRAT ray tracer indicated two possible source locations: the orography of the Scandes and a jet-exit region, which was travelling from west to east over the Atlantic Ocean and southern Scandinavia. A comparison of one ray trace with ERA5 model data, gave the impression of two crossing wave packets. A stationary, orographic gravity wave above the Scandes extending upwards, and an eastward moving wave packet originating from west of Scandinavia. During the HALO measurement flight, both wave packets were overlap-

ping above southern Scandinavia leading to the complex wave pattern observed by GLORIA. According to both models, these waves propagate up to the middle stratosphere. However, due to the observational filter of AIRS, in the satellite measurements their amplitudes are strongly underestimated and their vertical wavelengths overestimated. The remaining signal agrees qualitatively very well with the predictions by the ray tracer and ERA5. For an exact quantitative comparison and, thus, an experimental evidence on the importance of non-linear processes during gravity wave propagation, either another satellite instrument with different observational filter or a gravity wave with longer vertical wavelengths in the stratosphere would have been required. Nevertheless, this study shows, that a relatively simple model like GROGRAT performs very well on predicting the path of a gravity wave even in complex situations with multiple wave packets.

8 Summary and outlook

Due to computational constraints, gravity waves are implemented in nowadays general circulation models (GCMs) in the form of simplified sub-models called parameterisation schemes. These parameterisation schemes induce large uncertainties in seasonal weather predictions and climate projections. Further, there are hints that these parameterisation schemes cause a misrepresentation of middle atmospheric circulations in GCMs. These erroneous circulations then lead to model artefacts like for example the cold-pole bias in the Antarctic. Several theoretical studies proposed different concepts to improve gravity wave parameterisation schemes in GCMs. However, before implementation, these theories need to be validated by observations. This thesis, provides such validations using observations collected with GLORIA and investigated how such measurements can enhance our current understanding of gravity wave sources and propagation. In this respect, the urgent research questions stated in the introduction are repeated and addressed below:

Can GLORIA be used to study mesoscale gravity waves? Are the 3-D volumes of atmospheric temperature obtained from these measurements sufficient in size and spatial resolution to fully characterise mesoscale gravity waves?
Two different measurement concepts of GLORIA were considered in this thesis: full angle tomography (FAT) and limited angle tomography (LAT). In FAT a 3-D volume is encircled by a closed flight pattern of roughly 400 km diameter and the encircled volume is measured from all around. This enables the reconstruction of a large, cylindrical, 3-D volume with spatial resolution of 20 km in all horizontal directions and 200 m in the vertical. LAT, in contrast, is used for linear flight patterns and can only reconstruct a band of 150 km around a banana-shaped

vertical curtain parallel to the flight path. Further, the resolution of LAT is slightly decreased compared to FAT and amounts to 30 km in flight direction, 70 km perpendicular to the flight direction and 400 m in the vertical. To investigate the sensitivity of both measurement strategies to gravity waves, the concept of the observational filter, which has been applied in previous studies to investigate, how much of the amplitude of a gravity wave can be recovered by a certain measurement technique, has been extended to all important wave parameters needed for a full wave characterisation, i.e. the amplitude, the horizontal and vertical wavelengths, and the wave orientation. These detailed observational filters were derived in a simulation study for gravity waves with different wavelengths and phase front orientations. The derived observational filters show that the extent and resolution of the volumes obtained from both measurement concepts is sufficient to properly derive all important wave parameters of gravity waves with horizontal wavelengths above 200 km and vertical wavelengths above 2 km with high accuracy on optimised flight patterns. Thus, GLORIA measurements can provide a full wave characterisation of mesoscale gravity waves. This thesis directly confirms this theoretical result derived from simulations with the first 3-D reconstructions of mesoscale gravity waves in the lower stratosphere and the respective full wave characterisations.

How does the measurement set-up influence the quality of retrieved wave parameters?

For LAT the quality of reconstruction strongly depends on the orientation of the wave with respect to the instrument, which is not the case for FAT. For LAT, waves with phase fronts perpendicular to the flight path can be reconstructed best. If the phase fronts are turned away from this perfect orientation, the tilt of the wave becomes important for the quality of reconstruction. For waves tilted away from the instrument, the retrieval causes artefacts that reduce the quality of reconstruction. In general, the better the alignment of the line of sight (LOS) of the instrument with the phase fronts, the better can the wave structure be reproduced. Thus, steep waves are often better reconstructed than flat waves. For waves turned by more than 40° compared to the perfect orientation, the

quality of reproduction decreases drastically. A similar dependence of the reproduction quality on the wave orientation was already found in former studies for other limb sounding concepts (Wu and Waters, 1996; McLandress et al., 2000; Ungermann et al., 2010a). A comparison of LAT and FAT for a real gravity wave with 250 km horizontal and 5 km vertical wavelength above Iceland on 25 January 2016 showed a very good agreement between both methods, because the orientation of the LAT leg could be chosen almost perpendicular to the phase fronts.

What is the optimal flight strategy to observe mesoscale gravity waves with GLORIA?
The observation in LAT mode can be recommended as long as the orientation of the wave can be predicted before the flight and the flight path can be chosen more or less perpendicular to the phase fronts of the wave. Due to its slightly higher spatial resolution and accuracy FAT is favourable for short scale waves with small amplitudes and regions where gravity waves with multiple horizontal orientations overlap. Due to its shorter acquisition time, LAT is favourable for non-stationary situations, like experienced for example during a measurement flight on 28 January 2016 above southern Scandinavia. Here, two consecutive LAT retrievals could nicely show the temporal development of the gravity wave field.

Can GLORIA measurements confirm that oblique propagation can happen over large distances?
During a measurement flight above Iceland on 25 January 2016, a gravity wave with complex wave structure excited at the Icelandic orography was observed between 10 km and 14 km altitude. Already inside the measurement volume the gravity wave started to propagate horizontally towards the Atlantic Ocean. A propagation study using the Gravity wave Regional Or Global RAy Tracer (GROGRAT) and gravity wave-resolving reanalysis data from the European Centre for Medium-Range Weather Forecasts showed, that the gravity wave propagates more than 2000 km away from its source to western Russia. The comparatively simple ray-tracing model predicted for the gravity wave exactly the same propagation path as the much more computationally demanding numer-

ical weather prediction model. Surprising in both models: the strong oblique propagation happened in a narrow altitude range between 15 km and 20 km. Many theoretical studies have highlighted the importance of oblique gravity wave propagation for the correct representation of middle atmospheric circulations in GCMs (e.g. Song and Chun, 2008; Sato et al., 2009; Preusse et al., 2009a; Kalisch et al., 2014). However, no one predicted the oblique propagation to happen over such large horizontal distances and in such a small altitude range. On its long horizontal way through the atmosphere, the gravity wave is refracted by the background wind and changes its internal horizontal propagation direction from southward to westward. This change facilitates a final fast upward propagation into the westerly stratospheric jet. Comparisons of the model result to measurements taken by the Atmospheric Infrared Sounder (AIRS) in the mid stratosphere could neither support nor rebut the findings. The complexity of the gravity wave field in the stratosphere and the limited resolution of the AIRS measurements make a direct connection between observations and model results difficult.

How large are discrepancies between reality and simplified gravity wave parameterisation schemes?
Neither oblique propagation nor realistic wave orientations and thus wave refraction are implemented in current gravity wave parameterisation schemes. A 1-D version of GROGRAT was used to imitate a simplified parametrization scheme to study the differences between oblique and solely vertical propagation. It was shown, that such a simplified model does not only deposit the gravity wave momentum at the wrong horizontal location (more than 2000 km away in the studied case), but also at a too low altitude. Thus, these findings support theoretical studies requesting the implementation of oblique gravity wave propagation into climate models. One implementation of such a new parameterisation scheme is at the moment jointly developed by the national research group Multiscale Dynamics of Gravity Waves (MS-GWaves). The observations presented in this thesis act as motivation and validation for new theories and models developed within this research group.

How meaningful are the results of linear ray-tracing models? How

well do they agree with observations?
As mentioned above, the results of the linear ray-tracing model GROGRAT agree very well with the gravity wave-resolving reanalysis data. However, due to the limited vertical resolution of AIRS and the complexity of the stratospheric wave field on 26 January 2016, a direct connection of results from linear ray tracing with observations was not possible for the Iceland case study. On 28 January 2016, a second gravity wave case above Scandinavia was probed with GLORIA. It was predicted by GROGRAT, that this gravity wave propagates straight upward with amplitudes increasing up to 10 K and vertical wavelengths up to 15 km altitude in the mid stratosphere. Due to the observational filter of AIRS, gravity waves with vertical wavelengths in such a range are underestimated in amplitude by at least 80 % and overestimated in vertical wavelength by at least 30 %. This overestimation in vertical wavelength has not been addressed by previous publications using AIRS measurements (e.g. Hoffmann et al., 2013; Ern et al., 2017) and can lead to large errors in GWMF estimates. Further, it shows again the importance of detailed observational filters for all important wave parameters, like they have been derived in this thesis for the GLORIA instrument. Due to the amplitude underestimation, the satellite measurements show only little gravity wave perturbations above Scandinavia. In contrast, the ERA5 model shows gravity wave perturbations similar to the ones predicted by GROGRAT. A convolution of the ERA5 model data with the AIRS averaging kernel matrix, can reproduce the AIRS measurements very well. Thus, this case study shows qualitatively a very good agreement between observations and linear ray tracing. However, for an exact quantitative comparison new measurement concepts are required.

A new aircraft campaign planned for autumn 2019 has as scientific goal to further investigate the propagation of gravity waves. During this campaign, the aircraft will be equipped with a new lidar instrument, the Airborne Lidar for Studying the Middle Atmosphere (ALIMA), measuring the temperature profile between the aircraft and the mesopause. Together, GLORIA and the new lidar system will have a continuous measurement coverage from the tropopause up to the mesopause. As the

whole system is mounted on an airplane, it will be feasible for the first time, to trace a gravity wave with measurements along its oblique way through the atmosphere. Furthermore, a new satellite concept called ATMOSAT, has been proposed. Such a satellite, which is based on the infrared limb imaging concept, will have a much better vertical resolution than AIRS and, thus, resolve gravity wave with much shorter vertical wavelengths. Further, this new satellite would cover an altitude range from 5 km to 100 km altitude with tomographic measurements. Thus, the study of gravity wave propagation will be possible globally with measurements from one single instrument.

A Error analysis of the ray tracing calculations

In this appendix, the effects of different errors on the ray-tracing results are discussed exemplary for the Iceland case presented in Chapter 6 (see also Krisch et al., 2017). These errors may, in principle, be caused during each of the three main processing steps: temperature retrieval, background removal, and sinusoidal wave fits (S3D). Retrieval errors can be divided into precision and accuracy (see Chapter 3.2.2.3). Due to the high number of independent data in each S3D cube, the precision error (mainly due to noise) can be neglected, in particular since in this thesis only gravity wave events with amplitudes above a threshold of 0.5 K are considered. The error sources which lead to the accuracy error are systematic and slowly varying. Thus, their impact is mostly mitigated by the background removal.

The background removal separates the data into large-scale variations and small-scale fluctuations, the latter interpreted as gravity waves. The main effect of an unfavourably tuned background removal would be to eliminate real gravity waves. However, it would not introduce errors in the fitted wave vectors. Thus, this has to be considered in a comparison with other data but is not included in the further error discussion. The third step, the S3D method, is based on the assumption that the fitting volume is filled by a homogeneous wave, which is not always the case. In Chapter 6.4 a systematic low bias of 10 % in the vertical wavelength has been found for this case.

To investigate the effect of wrong input parameters ξ on the ray-tracing, these input parameters are varied by a factor ϵ_ξ. The variations ϵ_ξ for the vertical wavelength and the horizontal wave direction are chosen to be half the difference of the wave parameters at the upper ($\xi_{z=\max}$)

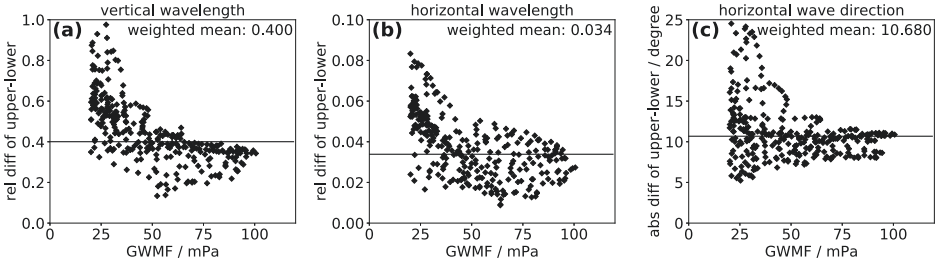

Figure A.1: Variations of wave parameters from the lower to the upper boundary of the S3D fitting volume. For all graphs GWMF weighted means are calculated and depicted as black lines. Figure adapted from Krisch et al. (2017)

and lower ($\xi_{z=min}$) boundary of the S3D fitting volume as determined by a ray-tracing reference run using exactly the S3D results as input (Figure A.1). The horizontal wavelength does not change much over the height of the fitting volume (Figure A.1 b). However, Figures 6.4 and 6.5 indicate a significant variation of the horizontal wavelength over the horizontal extent of the fitting volume. Hence, for the error estimate ray-tracing calculations, an error value of ±15 % is chosen as estimate for the horizontal variation of the horizontal wavelength within the S3D fitting volume. In Table A.1 the used error estimates for the three wave parameters are summarized.

The results of the back-tracing runs with wave parameters varied by the error estimates in Table A.1 are shown in Figure A.2. Longer vertical wavelengths (Figure A.2c, d) lead to more northward located sources, while rays from shorter vertical wavelengths (Figure A.2b) end southward, i.e., upstream of Iceland over the ocean. This is due to the fact that longer vertical wavelengths are associated with higher horizontal phase velocities and hence higher horizontal group velocities. Accordingly, in the case of shorter vertical wavelengths the waves are not able to compensate the background wind velocity and would origin from an upstream source. Actually, we find that the inferred bias (10 % larger values for the vertical wavelengths), when corrected, improves the match of the ray positions with the topography (Figure A.2c).

The horizontal wave direction has similar impact: when the wave is

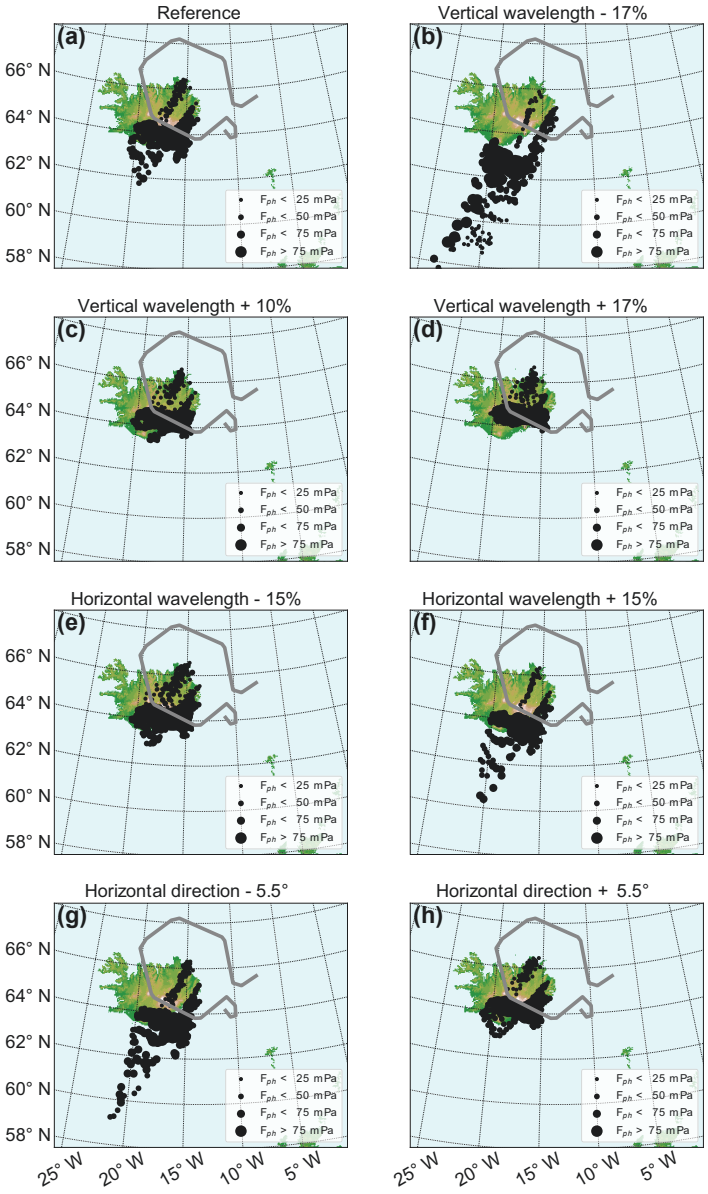

Figure A.2: Backward ray tracing with varying input wave parameters. The black dots mark the ray positions at 3 km altitude. Figure from Krisch et al. (2017)

Table A.1: Error estimates for the wave parameters inferred by the S3D method based on the change of the parameters over the extent of the fitting cube.

Error estimate of the vertical wavelength	±17 %
Error estimate of the horizontal wavelength	±15 %
Error estimate of the horizontal wave direction	±5.5°

turned more into the south-easterly background flow (Figure A.2h) the ray paths are more vertically oriented and therefore reach the ground closer to the measurement volume. When they are turned away from the background wind (Figure A.2g), the intrinsic group velocity and the background wind are at an angle, the intrinsic group velocity does not fully compensate the background wind, and the waves cover a larger horizontal distance reaching onto the ocean upstream of Iceland.

Similar variations for the forward ray traces are shown in Figure A.3. In all cases except for shorter vertical wavelengths, a major group of ray traces reaches the model top at 45 km altitude (white dots); i.e., our main findings presented in Chapter 6.4 are robust.

These calculations demonstrate that the uncertainties of the wave parameters derived from GLORIA measurements are well below the uncertainties stated in Table A.1 and that a correct identification of the gravity wave source is only feasible for highly accurate wave characterisations, such as achieved here thanks to the high spatial resolution and accuracy of GLORIA 3-D temperature measurements.

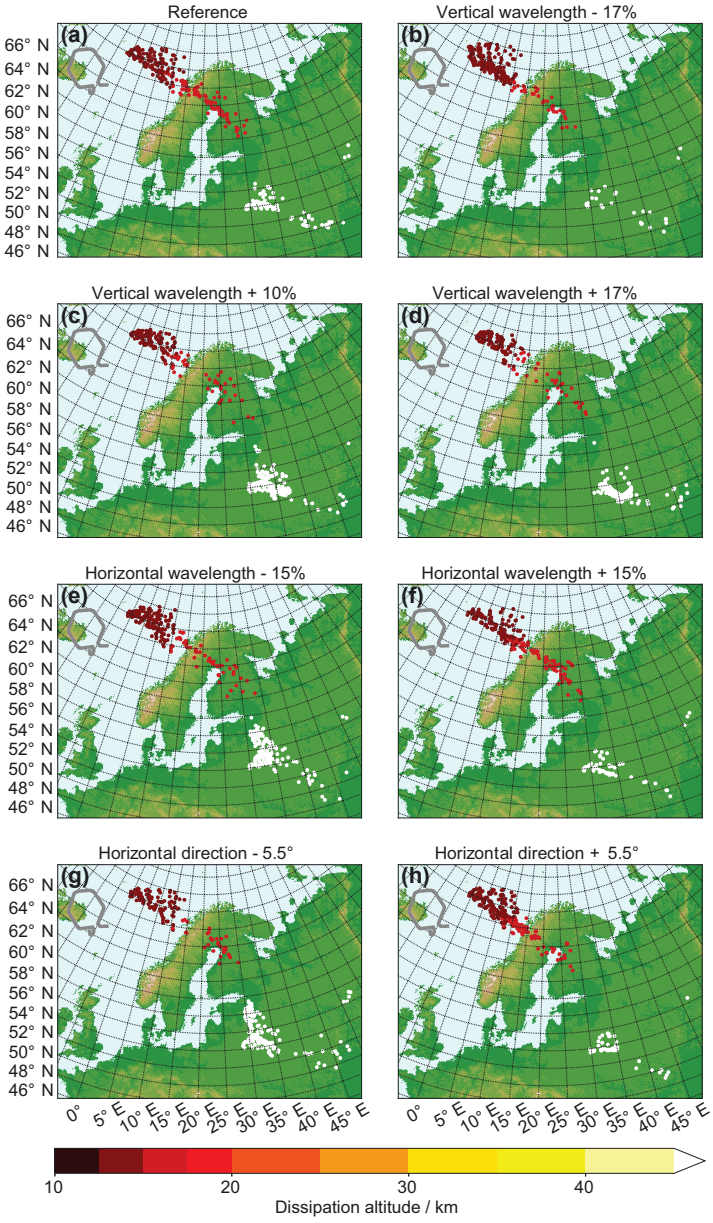

Figure A.3: Forward ray tracing with varying input wave parameters. The dots mark the dissipation point of the ray and the colour indicates the dissipation height. White dots mark waves which reach the model top at 45 km altitude. Figure from Krisch et al. (2017)

B Impact of black-body inhomogeneity on the retrieval results of GLORIA

The quality of GLORIA measurements strongly depends on a correct calibration. For the calibration of the GLORIA measurements, two on-board black bodies are used to estimate an additive and a multiplicative calibration factor for each detector pixel. Uncertainties in the temperature and thus radiation of these black bodies directly lead to uncertainties in the calibration of the measured infrared spectra. The present chapter will investigate, how these black-body uncertainties influence the retrieval results of different geophysical quantities. It is structured as follows: The radiometric calibration approach of GLORIA is described in Section B.1 and the influence of black-body uncertainty on the calibrated radiances in Section B.2. Section B.3 introduces the concept of how the propagation of this uncertainty through the retrieval is investigated. Section B.4 presents the results and a short discussion. For a more detailed discussion see Kleinert et al. (2018).

B.1 Radiometric calibration

The GLORIA measurements in arbitrary intensity units have to be radiometrically calibrated to absolute radiances. Two on-board calibration sources are used to estimate a unique gain and offset for each detector pixel. The two-point calibration approach requires a linear detector response or a correction of any non-linear behaviour of the detector system prior to radiometric calibration.

The radiometric in-flight calibration uses two blackbodies at different temperatures (Olschewski et al., 2013). They are mounted outside of the spectrometer, such that the whole optical path including the entrance window is calibrated. In order to cover the field of view (FOV) of the whole detector array, they have a rather large optical surface area of 126 mm × 126 mm. Since a revision of the black-body design in 2015, the emitting back-surface of the black body consists of 25 by 25 pyramids of 8 mm height. The backplane is wire eroded of one solid piece of aluminium for a good thermal conductivity. It features light traps at the bases of the pyramids to effectively avoid direct reflection of any incoming radiation and to increase the emissivity. Four thermoelectric coolers (TECs), which provide the options of cooling and heating, are used to stabilize the temperature of each black body. The baseplate of the pyramid array is equipped with 10 platinum resistance thermometers (PRTs) calibrated with a temperature uncertainty of 10 mK. The electronics measuring the resistance have an uncertainty of about 15 mΩ to 20 mΩ, corresponding to a temperature uncertainty of about 50 mK. Four of these sensors are placed directly under the TECs and are used to control the heating or cooling rate. The other six sensors are used for monitoring. The temperature of the cold black body is stabilized at or slightly below the ambient temperature (typically around 230 K to 230 K), the hot black body is heated to 30 K to 40 K above the cold one. In order to avoid ice contamination and to suppress stray light, a baffle is mounted in front of the casing of each black body. The baffle is cooled with two TECs to 2 K below the temperature of the pyramid array. The blackbodies are insulated with polystyrene foam sheets and the baffle system is thermally decoupled from the pyramid section with a layer of glass-fiber reinforced plastic.

The gain and offset of an instrument are defined as the multiplicative (gain, g) and additive (offset, L_0) factors, which must be applied to the true radiation L, in order to get the signal measured by the instrument S (Revercomb et al., 1988, see, e.g.):

$$S = g(L + L_0) \tag{B.1}$$

These factors differ for each pixel and wavelength. Gain and offset can be determined from measurements of two black-body sources with known temperature. Assuming an emissivity of 1, the gain is calculated as

$$g = \frac{S_{\mathrm{bb2}} - S_{\mathrm{bb1}}}{\mathscr{B}(T_{\mathrm{bb2}}) - \mathscr{B}(T_{\mathrm{bb1}})} \tag{B.2}$$

and the offset as

$$L_0 = \frac{S_{\mathrm{bb1}}}{g} - \mathscr{B}(T_{\mathrm{bb1}}), \tag{B.3}$$

with $\mathscr{B}(T)$ being the Planck function of the given temperature. More details on the calibration concept of GLORIA are given by Kleinert et al. (2014) and Olschewski et al. (2013).

The calibrated spectral radiation L can be calculated from the measurements by dividing the measured radiation S by the gain g and subtracting the offset L_0:

$$L = \frac{S}{g} - L_0. \tag{B.4}$$

B.2 Impact of black-body temperature uncertainty on radiances

The surface area of the backplane of the GLORIA blackbodies with a size of 126 mm × 126 mm is rather large. It is a technically challenging task to get a completely uniform temperature distribution over this big area. In reality, the temperature varies across the black body due to thermal gradients inside the backplane, the air flow around the pyramids, and an imperfect temperature regulation. If the true black-body temperature $T_{\mathrm{bb}}^{t} = T_{\mathrm{bb}} - \Delta T_{\mathrm{bb}}$ deviates from T_{bb}, which is used for calculating g and

L_0, the true gain g_t and true offset L_0^t differ from g and L_0 as follows:

$$g^t = \frac{S_{bb2} - S_{\mathrm{bb1}}}{\mathscr{B}(T^t_{\mathrm{bb2}}) - \mathscr{B}(T^t_{\mathrm{bb1}})} = g\alpha, \tag{B.5}$$

with

$$\alpha = \frac{\mathscr{B}(T_{\mathrm{bb2}}) - \mathscr{B}(T_{\mathrm{bb1}})}{\mathscr{B}(T^t_{\mathrm{bb2}}) - \mathscr{B}(T^t_{\mathrm{bb1}})} \tag{B.6}$$

and

$$L_0^t = \frac{S_{\mathrm{bb1}}}{g^t} - \mathscr{B}(T^t_{\mathrm{bb1}}). \tag{B.7}$$

This leads to a deviation ΔL of the originally calculated calibrated radiation L from the true calibrated radiation L^t . The calibrated spectra can be expressed in terms of the "true" calibrated spectra $L^t = S/g^t - L_0^t$:

$$L = \frac{S}{g} - L_0 = \frac{S - S_{\mathrm{bb1}}}{g^t}\alpha + \mathscr{B}(T_{\mathrm{bb1}}) = \left(\frac{S - S_{\mathrm{bb1}}}{g^t} + \mathscr{B}(T^t_{\mathrm{bb1}})\right)\alpha + \mathscr{B}(T_{\mathrm{bb1}}) \tag{B.8}$$

$$= \left(L^t - \mathscr{B}(T^t_{\mathrm{bb1}})\right)\alpha + \mathscr{B}(T_{\mathrm{bb1}}). \tag{B.9}$$

Thus the deviation ΔL is

$$\Delta L = L - L^t = L^t(\alpha - 1) - \mathscr{B}(T_{\mathrm{bb1}}). \tag{B.10}$$

This deviation is a combination of a scaling compared to the true calibrated measurements and an additive offset.

If one black-body measurement is replaced by a deep space measurement, the deviation simplifies to a simple scaling of the true calibrated measurements:

$$\Delta L_{\mathrm{bb,ds}} = L^t\left(\frac{\mathscr{B}(T_{\mathrm{bb}})}{\mathscr{B}(T^t_{\mathrm{bb}})} - 1\right) \tag{B.11}$$

as the emission of deep space can be assumed to be effectively zero.

B.3 Concept of the used Monte Carlo approach

A Monte Carlo approach (e.g Metropolis and Ulam, 1949; Press, 1968) is used to study the impact of black-body uncertainties on the GLORIA retrieval results. Therefore, many random temperature fluctuations of the blackbodies are generated and the effects of these fluctuations on the retrieved climate variables are calculated. Afterwards, statistical information on the perturbed retrieval results is derived. Only vertical temperature variations are taken into account, as the row averaged radiation is used for the standard GLORIA retrievals. Consequently, a random temperature deviation is created for each vertical pixel around the measured mean black-body temperature $\boldsymbol{T}_{\mathrm{bb}}$. These deviations $\Delta\boldsymbol{T}_{bb}$ are defined over the detector through the covariance matrix **COV** with standard deviation σ and correlation length c:

$$\mathbf{COV}(i,j) = \sigma^2 \cdot e^{-\frac{1}{2}\cdot\left(\frac{i-j}{c}\right)^2}, \tag{B.12}$$

with i and j denoting the 128 averaged rows of the detector. Examples for these temperature deviations $\Delta\boldsymbol{T}_{\mathrm{bb}}$ are shown in Figure B.1 for different correlation lengths. A correlation length of 0 means completely uncorrelated deviations and infinity completely correlated (i.e., constant) ones. Due to the optical set-up and the thermal conductivity of the blackbody surface, typical correlation lengths of the GLORIA blackbodies are expected to be in the range of 10 to 100 pixels. Temperature variations across the emitting surface have to be rather smooth because of the thermal conductivity of the material. Furthermore, the instrument is focused to infinity and the picture of the black-body backplane on the detector is not sharp. Therefore correlation lengths below 10 pixels are not expected.

For each pair of standard deviation and correlation length, 256 ran-

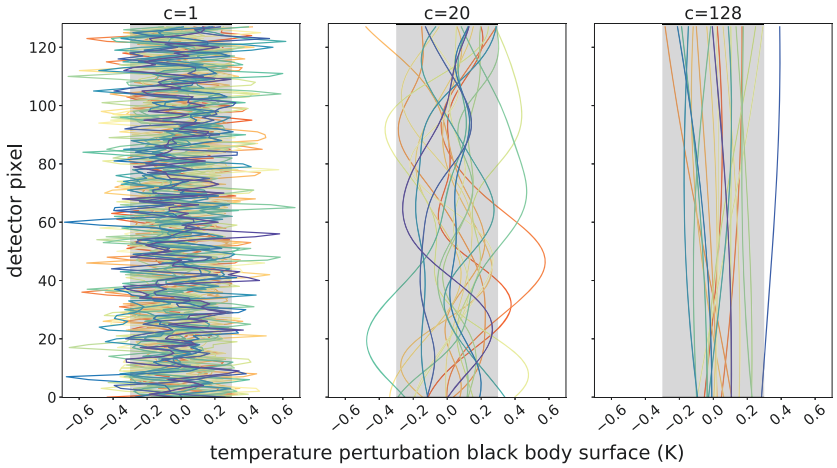

Figure B.1: Random temperature deviations for the 128 vertical detector pixels with different correlation lengths c. The temperature deviations in panel (a) have a correlation length of one vertical pixel, meaning that they are nearly uncorrelated. In contrast the temperature deviations in panel (c) are nearly fully correlated over the whole detector (correlation length of 128 pixels). In panel (b) a correlation length of 20 pixels is depicted. All variations have a standard deviation of $\sigma = 0.2$. The gray shade marks the 3σ area. Figure from Kleinert et al. (2018)

dom temperature distributions are generated. These black-body temperature deviations transform into radiation deviation distributions $\Delta \boldsymbol{L}$ according to Equation B.11. This study uses atmospheric profiles from a climatology (Remedios et al., 2007) in the mid-latitudes to simulate infrared spectra as they would be measured by GLORIA at 15 km flight altitude. The GLORIA Measurement Simulator uses vertical profiles of relevant trace species and of pressure and temperature from the climatology and combines them in a forward model with the GLORIA measurement geometry. This results in one infrared spectrum for each of the 128 vertical pixels. Typical noise values of the GLORIA instrument are added to these spectra. These synthetic measurements are transferred back into the geophysical quantities of temperature and trace gas volume mixing ratios according to the retrieval set-up described in Ungermann et al.

(2015) for the GLORIA dynamics mode. A gain matrix G is calculated in this retrieval process, which correlates measurement deviations ($\Delta \boldsymbol{L}$) with retrieval result uncertainties ($\Delta \boldsymbol{x}$). As the radiation errors caused by the black-body inhomogeneities are small compared to the simulated radiations, the retrieval can be linearised and the retrieval gain matrix $\mathbf{G}$ can be assumed to be constant for the small deviations $\Delta \boldsymbol{L}$ around the original radiation (Rodgers, 2000). Therefore, the influence of the black-body temperature deviations on the retrieval result of atmospheric trace gases and temperature can be calculated as follows:

$$\mathbf{G} \cdot \Delta \boldsymbol{L} = \Delta \boldsymbol{x}. \tag{B.13}$$

The retrieval uncertainty distribution is estimated through a fit of a Gaussian shaped probability distribution to the 256 $\Delta \boldsymbol{x}$ vectors of each pair of correlation length and standard deviation of the original $\Delta \boldsymbol{T}_{bb}$ distribution. This allows us to estimate a standard deviation and a correlation length of the retrieval uncertainty probability distribution.

B.4 Study results and discussion

The measurement uncertainty of GLORIA should ideally be small compared to the decadal trends. We therefore choose a target and a threshold value for the accuracy of 20 % and 40 % of the decadal trends, respectively. Table B.1 shows the decadal trends in temperature, ozone, and water vapour together with the resulting target and threshold values for these entities.

Table B.1: Long term trends in temperature, ozone, and water vapour in the UTLS region and the derived target and threshold values for GLORIA retrievals.

	temperature	ozone	water vapor
10 year trend	1 K	5%	0.5 ppmv
reference	Schmidt et al. (2010)	WMO (2014)	Solomon et al. (2010)
target (threshold)	0.08% (0.16%)	1% (2%)	2.5% (5%)

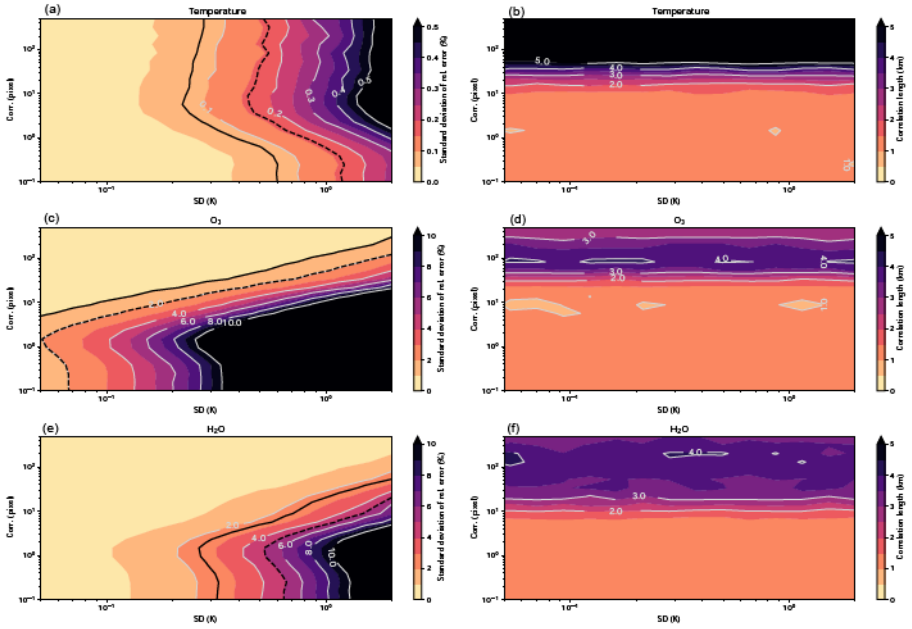

Figure B.2: Results of the Monte Carlo approach. Plotted are the standard deviations (left panels) and correlations lengths (right panels) of the retrieval error distributions. The x-axis shows the standard deviation of the original random variation of the black-body temperature, the y-axis the according correlation length. The top row represents the temperature retrieval, in the middle ozone is shown, and the bottom depicts water vapour. The black solid (dashed) line in the left plots indicates the error target (threshold) due to the long term trend of the respective atmospheric species. Figure from Kleinert et al. (2018)

As described before, a Monte Carlo approach is used to estimate the propagation of temperature non-uniformities of the black-body surface through the retrieval. Figure B.1 shows the results of this study. The standard deviations and correlation lengths of the retrieval errors are displayed for different standard deviations and correlation lengths of the random deviations of the black-body temperature. These retrieval errors are averaged over the altitude range $7-14$ km. As expected, the correlation length of the retrieval error increases with the correlation length of the input for all species (see right panels in Figure B.2). For all species shown, the correlation lengths of the retrieval errors are around 1 km to 1.5 km for black-body non-uniformities correlated over less than 50 pixels. For temperature deviations over larger areas, the correlation lengths in the retrieval errors grow accordingly. These more extended errors introduce a bias in the measurements but do not influence the general structures of the measured species. For some scientific uses, such as gravity wave research, this is more acceptable than errors with short correlation lengths.

The standard deviations of the results depend strongly on the retrieved species. For typical correlation lengths of the GLORIA black-body temperature deviations (10 to 100 pixels) the accepted threshold of 2 % error for the ozone retrieval is reached for standard deviations of 0.2 K to 2 K. Therefore, a required threshold of 200 mK and a target of 100 mK for the temperature standard deviation of the black body are defined through the ozone retrieval. These values can be relaxed for temperature deviations with longer correlation lengths, as can be seen in the plot in Fig. 5c. For the temperature retrieval the threshold of 0.16 % uncertainty is reached for all correlation lengths above two pixels at around 400 mK. The target uncertainty is reached already at 200 mK. For water vapour retrievals the threshold and target values are located at a standard deviation of 500 mK and 250 mK for correlation lengths of one pixel but can be relaxed for more correlated non-uniformities.

Thus, for the GLORIA instrument and the applied retrieval set-up, the ozone retrieval sets the threshold requirement of the standard deviation of the black-body uncertainties to 200 mK and the desired target to 100 mK.

List of figures

List of tables

List of abbreviations

AIRS	Atmospheric Infrared Sounder
ALIMA	Airborne Lidar for Studying the Middle Atmosphere
BAHAMAS	Basic HALO Measurement and Sensor System
DOAS	Differential Optical Absorption Spectroscopy
ECMWF	European Centre for Medium-Range Weather Forecasts
EGA	emissivity growth approximation
EOS	NASA's Earth Observing System
ERA5	European Center for Medium-Range Weather Forecast reanalysis data set
FAT	full angle tomography
FTS	Fourier Transform Spectrometer
FWHM	full width at half maximum
GCM	general circulation model
GLORIA	Gimballed Limb Observer for Radiance Imaging of the Atmosphere
GLSIM	GLORIA measurement simulator
GROGRAT	Gravity wave Regional Or Global RAy Tracer
GW-LCYCLE	gravity wave life cycle aircraft campaign
GWEX	gravity wave experiment
GWMF	vertical flux of horizontal pseudo-momentum of a gravity wave
HALO	High Altitude and Long Range Research Aircraft (DLR, 2018)
ILS	instrument line shape
JURASSIC2	Jülich Rapid Spectral Simulation Code V2
JUTIL	Jülich Tomographic Library

LAT	limited angle tomography
LOS	line of sight
MAARSY	Middle Atmosphere Alomar Radar System
MS-GWaves	Multiscale Dynamics of Gravity Waves
MSS	Mission Support System flight planning tool
NWP	numerical weather prediction
PGGS	scientific aircraft campaign including POLSTRACC, GWEX, GW-LCYCLE, and SALSA
POLSTRACC	polar stratosphere in a changing climate aircraft campaign
PSF	point spread function
S3D	three-dimensional sinusoidal fitting routine
SALSA	seasonality of air mass transport and origin in the lowermost stratosphere aircraft campaign
WACCM4	Whole Atmosphere Community Climate Model version 4
WALES	Water Vapour Lidar Experiment in Space
WMS	Open Geospatial Consortium Web Map Service

List of symbols

This thesis uses the following atmospheric quantities and constants. Regular cursive symbols (e.g. N) are used for real numbers and functions mapping into $\mathbb{R}$. Bold cursive symbols (e.g. $\boldsymbol{u}$) stand for vectors and vector-valued functions. Regular bold symbols (e.g. $\mathbf{A}$) refer to matrices. A subscription of x, y or z (e.g. $c_{g,z}$) describes the component of the vector in x, y or z direction, respectively. Symbols denoted by an apostrophe (e.g. T') are perturbations or fluctuations, a hat (e.g. $\hat{T}$) indicates the amplitude of these fluctuations, a bar the mean or background state (e.g. $\bar{T}$). Symbols with a subscripted 0 are in general time invariant (e.g. U_0). The subscription of *gb* stands for ground-based (e.g. $\boldsymbol{c}_{p,gb}$).

$\mathbf{A}$	averaging kernel matrix
$\boldsymbol{a}$	atmospheric state vector
$\boldsymbol{a}_a$	a priori atmospheric state vector
$\boldsymbol{a}_r$	retrieved atmospheric state vector
$\boldsymbol{a}_s$	simulated atmospheric state vector
$\mathscr{A}$	complex amplitude of wave motion
A, B	amplitudes of wave motions
$\mathscr{B}$	Planck function
c	speed of light
$\boldsymbol{c}_g$	group velocity
c_h	horizontal correlation length
c_p	specific heat of air
$\boldsymbol{c}_p$	phase velocity
c_z	vertical correlation length

CCl_4	tetrachloromethane
CH_4	methane
χ^2	cost function of sinusoidal fit
CO_2	carbon dioxide
$\boldsymbol{\epsilon}$	vector of measurement errors
$\boldsymbol{\epsilon}_s$	simulated measurement error
η	wave motion
f	Coriolis frequency
$\boldsymbol{F}$	forward model
$\mathbf{F}'$	Jacobian matrix of $\boldsymbol{F}$
$\boldsymbol{Fr}$	Froude number
g	standard gravity
$\mathbf{G}$	gain matrix
γ	temperature gradient
Γ	adiabatic temperature gradient
H_2O	water vapour
h_p	Planck constant
HNO_3	nitric acid
I	radiation intensity
$\mathfrak{J}$	radiative source function
J	cost function of retrieval
j	emission coefficient
$\boldsymbol{k}$	wave vector, $\boldsymbol{k} = (k, l, m)$
k_b	Boltzmann constant
κ	absorption coefficient
$\boldsymbol{k}_h$	horizontal wave vector, $\boldsymbol{k}_h = (k, l)$
λ_h	horizontal wavelength, $\lambda_h = \frac{2\pi}{\lvert\boldsymbol{k}_h\rvert}$
λ_z	vertical wavelength, $\lambda_z = \frac{2\pi}{m}$
N	buoyancy frequency
ν	wave number
O	observational filter
O_3	ozone
Ω	ground based frequency

ω	intrinsic frequency
ϕ	wave phase
Φ	elevation angle
φ	angle of wave to the vertical
ψ	angle of wave in the horizontal
R_0	Rossby number
ρ	density
S	retrieval sensitivity to gravity waves
s, s', s''	path in space
$\mathbf{S}_a$	a priori covariance matrix
$\mathbf{S}_a^{-1}$	a priori precision matrix, inverse of $\mathbf{S}_a$
$\mathbf{S}_\epsilon$	measurement error cov. matrix
$\mathbf{S}_\epsilon^{-1}$	measurement error precision matrix, inverse of $\mathbf{S}_\epsilon$
σ	standard deviation
σ_f	sinusoidal fit weighting function
T	temperature
t	time
$\mathbf{t}$	transmittance
$\boldsymbol{T}_c$	climatological temperature distribution
$\boldsymbol{T}_r$	retrieved temperature distribution
$\boldsymbol{T}_s$	simulated temperature distribution
τ	optical thickness
θ	latitude
Θ	azimuth angle
$\bar{\boldsymbol{u}}$	background wind
U_0	time invariant background wind in x-direction
u_h	horizontal wind magnitude
$U_{0,\perp}$	time invariant background wind perpendicular to the mountain ridge
$U_{0,\|\|}$	time invariant background wind parallel to the mountain ridge
$u_\perp$	wind perpendicular to the wave vector
$u_{\|\|}$	wind parallel to the wave vector

w	vertical wind
$w_{0,1}$	retrieval weighting functions
$w^i_{s,r}$	simulated or retrieved wave perturbation at point $\boldsymbol{x}_i$
$\boldsymbol{x}$	location in space, $\boldsymbol{x}$=(x, y, z)
ξ	vertical displacement
$\boldsymbol{y}$	measurement vector

Bibliography

M. J. Alexander and T. J. Dunkerton. A spectral parameterization of mean-flow forcing due to breaking gravity waves. *J. Atmos. Sci.*, 56: 4167–4182, 1999.

M. J. Alexander and D. A. Ortland. Equatorial waves in High Resolution Dynamics Limb Sounder (HIRDLS) data. *J. Geophys. Res.*, 115, 2010. ISSN 2169-897X. doi:10.1029/2010JD014782.

M. J. Alexander and L. Pfister. Gravity wave momentum flux in the lower stratosphere over convection. *Geophys. Res. Lett.*, 22(15):2029–2032, 1995. ISSN 0094-8276. doi:10.1029/95GL01984.

M. J. Alexander and K. H. Rosenlof. Gravity-wave forcing in the stratosphere: Observational constraints from the upper atmosphere research satellite and implications for parameterization in global models. *J. Geophys. Res.*, 108(D19):4597, 2003. doi:10.1029/2003JD003373.

M. J. Alexander, J. H. Beres, and L. Pfister. Tropical stratospheric gravity wave activity and relationships to clouds. *J. Geophys. Res.*, 105(D17): 22299–22309, 2000. doi:10.1029/2000JD900326.

M. J. Alexander, M. Geller, C. McLandress, S. Polavarapu, P. Preusse, F. Sassi, K. Sato, S. Eckermann, M. Ern, A. Hertzog, Y. Kawatani, M. Pulido, T. A. Shaw, M. Sigmond, R. Vincent, and S. Watanabe. Recent developments in gravity-wave effects in climate models and the global distribution of gravity-wave momentum flux from observations and models. *Quart. J. Roy. Meteorol. Soc.*, 136:1103–1124, 2010. ISSN 0035-9009. doi:10.1002/qj.637.

A. Amemiya and K. Sato. A new gravity wave parameterization including three-dimensional propagation. *Journal of the Meteorological Society of Japan. Ser. II*, advpub, 2016. doi:10.2151/jmsj.2016-013.

H. H. Aumann, M. T. Chahine, C. Gautier, M. D. Goldberg, E. Kalnay, L. M. McMillin, H. Revercomb, P. W. Rosenkranz, W. L. Smith, D. H. Staelin, L. L. Strow, and J. Susskind. AIRS/AMSU/HSB on the Aqua mission: Design, science objective, data products, and processing systems. In *IEEE T. Geosci. Remote. Sens.*, volume 41, pages 253–264, 2003. doi:10.1109/TGRS.2002.808356.

J. T. Bacmeister, P. A. Newman, B. L. Gary, and K. R. Chan. An algorithm for forecasting mountain wave-related turbulence in the stratosphere. *Weather and Forecasting*, 9(2):241–253, 1994. doi:10.1175/1520-0434(1994)009<0241:AAFFMW>2.0.CO;2.

G. Boccara, A. Hertzog, R. A. Vincent, and F. Vial. Estimation of gravity wave momentum flux and phase speeds from quasi-Lagrangian stratospheric balloon flights. Part I: Theory and simulations. *J. Atmos. Sci.*, 65(10):3042–3055, 2008. ISSN 0022-4928. doi:10.1175/2008JAS2709.1.

G. Boeloeni, B. Ribstein, J. Muraschko, C. Sgoff, J. Wei, and U. Achatz. The Interaction between Atmospheric Gravity Waves and Large-Scale Flows: An Efficient Description beyond the Nonacceleration Paradigm. *J. Atmos. Sci.*, 73(12):4833–4852, 2016. ISSN 0022-4928. doi:10.1175/JAS-D-16-0069.1.

K. Bossert, D. C. Fritts, P.-D. Pautet, B. P. Williams, M. J. Taylor, B. Kaifler, A. Doernbrack, I. M. Reid, D. J. Murphy, A. J. Spargo, and A. D. MacKinnon. Momentum flux estimates accompanying multiscale gravity waves over Mount Cook, New Zealand, on 13 July 2014 during the DEEPWAVE campaign. *J. Geophys. Res. Atmos.*, 120(18):9323–9337, 2015. ISSN 2169-897X. doi:10.1002/2015JD023197.

F. P. Bretherton. On the mean motion induced by internal grav-

ity waves. *Journal of Fluid Mechanics*, 36(4):785–803, 1969. doi:10.1017/S0022112069001984.

O. Buehler and M. E. McIntyre. Remote recoil: a new wave-mean interaction effect. *J. Fluid Mech.*, 492:207–230, 2003.

S. A. Buehler, P. Eriksson, T. Kuhn, A. von Engeln, and C. Verdes. ARTS, the atmospheric radiative transfer simulator. *J. Quant. Spectrosc. Radiat. Transfer*, 91:65–93, 2005.

O. Bühler. On shear-generated gravity waves that reach the mesosphere. part i: Wave generation. *J. Atmos. Sci.*, 56:3749–3773, 1999.

A. C. Bushell, N. Butchart, S. H. Derbyshire, D. R. Jackson, G. J. Shutts, S. B. Vosper, and S. Webster. Parameterized Gravity Wave Momentum Fluxes from Sources Related to Convection and Large-Scale Precipitation Processes in a Global Atmosphere Model. *J. Atmos. Sci.*, 72(11): 4349–4371, 2015. ISSN 0022-4928. doi:10.1175/JAS-D-15-0022.1.

N. Butchart. The brewer-dobson circulation. *Rev. Geophys.*, 52(2):157–184, 2014. ISSN 1944-9208. doi:10.1002/2013RG000448.

S. Butterworth. On the Theory of Filter Amplifiers. *Wireless Engineer*, 7, 1930.

B. Cao, C. J. Heale, Y. Guo, A. Z. Liu, and J. B. Snively. Observation and modeling of gravity wave propagation through reflection and critical layers above andes lidar observatory at cerro pachón, chile. *J. Geophys. Res. Atmos.*, 121(21):12,737–12,750, 2016. ISSN 2169-8996. doi:10.1002/2016JD025173. 2016JD025173.

M. T. Chahine, T. S. Pagano, H. H. Aumann, R. Atlas, C. Barnet, J. Blaisdell, L. Chen, M. Divakarla, E. J. Fetzer, M. Goldberg, C. Gautier, S. Granger, S. Hannon, F. W. Irion, R. Kakar, E. Kalnay, B. H. Lambrigtsen, S.-Y. Lee, J. Le Marshall, W. W. McMillan, L. McMillin, E. T. Olsen, H. Revercomb, P. Rosenkranz, W. L. Smith, D. Staelin, L. L. Strow,

J. Susskind, D. Tobin, W. Wolf, and L. Zhou. Improving weather forecasting and providing new data on greenhouse gases. *Bull. Amer. Meteor. Soc.*, 87(7):911+, 2006. ISSN 0003-0007. doi:10.1175/BAMS-87-7-911.

S. Chandrasekhar. *Radiative Transfer*. Dover, 1960.

T. L. Clark, T. Hauf, and J. P. Kuettner. Convectively forced internal gravity waves: Results from two-dimensional numerical experiments. *Quart. J. Roy. Meteorol. Soc.*, 112(474):899–925, 1986. doi:10.1002/qj.49711247402.

P. Cunningham and D. Keyser. Analytical and numerical modelling of jet streaks: Barotropic dynamics. *Quarterly Journal of the Royal Meteorological Society*, 126(570):3187–3217, 2000. doi:10.1002/qj.49712657010.

A. de la Camara and F. Lott. A parameterization of gravity waves emitted by fronts and jets. *Geophys. Res. Lett.*, 42(6):2071–2078, 2015. ISSN 0094-8276. doi:10.1002/2015GL063298.

E. M. Dewan, R. H. Picard, R. R. O'Neil, H. A. Gardiner, J. Gibson, J. D. Mill, E. Richards, M. Kendra, and W. O. Gallery. MSX satellite observations of thunderstorm-generated gravity waves in mid-wave infrared images of the upper stratosphere. *Geophys. Res. Lett.*, 25(7):939–942, 1998.

DLR. Halo website. `http://www.halo.dlr.de/aircraft/specifications.html`, 2018. Last access: 17 May 2018.

L. Eberly and B. R. Sutherland. Anelastic internal wave reflection and transmission in uniform retrograde shear. *Phys. Fluids*, 26(2), 2014. ISSN 1070-6631. doi:10.1063/1.4864104.

S. D. Eckermann and C. J. Marks. GROGRAT: a new model of the global propagation and dissipation of atmospheric gravity waves. *Adv. Space Res.*, 20:1253–1256, 1997.

S. D. Eckermann and R. A. Vincent. Falling sphere observations of anisotropic gravity wave motions in the upper stratosphere over australia. *Pure Appl. Geophys.*, 130:509–532, 1989.

M. Ern, P. Preusse, M. J. Alexander, and C. D. Warner. Absolute values of gravity wave momentum flux derived from satellite data. *J. Geophys. Res. Atmos.*, 109(D20), 2004. ISSN 2156-2202. doi:10.1029/2004JD004752.

M. Ern, P. Preusse, and C. D. Warner. A comparison between CRISTA satellite data and Warner and McIntyre gravity wave parameterization scheme: horizontal and vertical wavelength filtering of gravity wave momentum flux. *Adv. Space Res.*, 35:2017–2023, 2005. doi:10.1016/j.asr.2005.04.109.

M. Ern, P. Preusse, and C. D. Warner. Some experimental constraints for spectral parameters used in the Warner and McIntyre gravity wave parameterization scheme. *Atmos. Chem. Phys.*, 6(12):4361–4381, 2006. doi:10.5194/acp-6-4361-2006.

M. Ern, Q. T. Trinh, P. Preusse, J. C. Gille, M. G. Mlynczak, J. M. Russell III, and M. Riese. GRACILE: A comprehensive climatology of atmospheric gravity wave parameters based on satellite limb soundings. *Earth Syst. Sci. Dat.*, 2018:857–892, 2018. doi:10.5194/essd-10-857-2018.

M. Ern, L. Hoffmann, and P. Preusse. Directional gravity wave momentum fluxes in the stratosphere derived from high-resolution AIRS temperature data. *Geophys. Res. Lett.*, 44(1):475–485, 2017. ISSN 0094-8276. doi:10.1002/2016GL072007.

E. J. Fetzer and J. C. Gille. Gravity wave variance in LIMS temperatures. part I: Variability and comparison with background winds. *J. Atmos. Sci.*, 51(17):2461–2483, 1994. doi:10.1175/1520-0469(1994)051<2461:GWVILT>2.0.CO;2.

R. Fovell, D. Durran, and J. R. Holton. Numerical simulations of convectively generated stratospheric gravity waves. *J. Atmos. Sci.*, 49: 1427–1442, 1992.

F. Friedl-Vallon, T. Gulde, F. Hase, A. Kleinert, T. Kulessa, G. Maucher, T. Neubert, F. Olschewski, C. Piesch, P. Preusse, H. Rongen, C. Sartorius, H. Schneider, A. Schönfeld, V. Tan, N. Bayer, J. Blank, R. Dapp, A. Ebersoldt, H. Fischer, F. Graf, T. Guggenmoser, M. Höpfner, M. Kaufmann, E. Kretschmer, T. Latzko, H. Nordmeyer, H. Oelhaf, J. Orphal, M. Riese, G. Schardt, J. Schillings, M. K. Sha, O. Suminska-Ebersoldt, and J. Ungermann. Instrument concept of the imaging Fourier transform spectrometer GLORIA. *Atmos. Meas. Tech.*, 7(10):3565–3577, 2014. doi:10.5194/amt-7-3565-2014.

D. Fritts and M. Alexander. Gravity wave dynamics and effects in the middle atmosphere. *Rev. Geophys.*, 41(1), 2003. ISSN 8755-1209. doi:10.1029/2001RG000106.

D. C. Fritts and Z. Luo. Gravity wave excitation by geostrophic adjustment of the jet stream. part i: Two-dimensional forcing. *J. Atmos. Sci.*, 49(8):681–697, 1992. doi:10.1175/1520-0469(1992)049<0681:GWEBGA>2.0.CO;2.

D. C. Fritts and G. D. Nastrom. Sources of mesoscale variability of gravity waves. Part II: Frontal, convective and jet stream excitation. *J. Atmos. Sci.*, 49:111–127, 1992.

D. C. Fritts and P. K. Rastogi. Convective and dynamical instabilities due to gravity wave motions in the lower and middle atmosphere: theory and observations. *Radio Sci.*, 20:1247–1277, 1985.

D. C. Fritts, R. B. Smith, M. J. Taylor, J. D. Doyle, S. D. Eckermann, A. Doernbrack, M. Rapp, B. P. Williams, P. D. Pautet, K. Bossert, N. R. Criddle, C. A. Reynolds, P. A. Reinecke, M. Uddstrom, M. J. Revell, R. Turner, B. Kaifler, J. S. Wagner, T. Mixa, C. G. Kruse, A. D. Nugent, C. D. Watson, S. Gisinger, S. M. Smith, R. S. Lieberman, B. Laughman, J. J. Moore, W. O. Brown, J. A. Haggerty, A. Rockwell, G. J.

Stossmeister, S. F. Williams, G. Hernandez, D. J. Murphy, A. R. Klekociuk, I. M. Reid, and J. Ma. The deep propagating gravity wave experiment (DEEPWAVE): An airborne and ground-based exploration of gravity wave propagation and effects from their sources throughout the lower and middle atmosphere. *Bull. Amer. Meteor. Soc.*, 97(3): 425–453, 2016. ISSN 0003-0007. doi:10.1175/BAMS-D-14-00269.1.

R. R. Garcia, A. K. Smith, D. E. Kinnison, A. de la Camara, and D. J. Murphy. Modification of the gravity wave parameterization in the whole atmosphere community climate model: Motivation and results. *J. Atmos. Sci.*, 74(1):275–291, 2017. doi:10.1175/JAS-D-16-0104.1.

M. A. Geller, M. J. Alexander, P. T. Love, J. Bacmeister, M. Ern, A. Hertzog, E. Manzini, P. Preusse, K. Sato, A. A. Scaife, and T. Zhou. A comparison between gravity wave momentum fluxes in observations and climate models. *J. Clim.*, 26(17):6383–6405, 2013. ISSN 0894-8755. doi:10.1175/JCLI-D-12-00545.1.

A. J. Gerrard, T. J. Kane, S. D. Eckermann, and J. P. Thayer. Gravity waves and mesospheric clouds in the summer middle atmosphere: A comparison of lidar measurements and ray modeling of gravity waves over sonderstrom, greenland. *J. Geophys. Res.*, 109, 2004. doi:10.1029/2002JD002783.

A. Giez. Effective test and calibration of a trailing cone system on the atmospheric research aircraft HALO. Proceedings of the 56th Annual Symposium of the Society of Experimental Test Pilots, Anaheim, USA, 2012.

Git. version control system. `http://git-scm.com/`, 2018. last access: 10 August 2018.

L. L. Gordley and J. M. Russell. Rapid inversion of limb radiance data using an emissivity growth approximation. *Appl. Optics*, 20:807–813, 1981. doi:10.1364/AO.20.000807.

M. Griffiths and M. Reeder. Stratospheric inertia-gravity waves generated in a numerical model of frontogenesis .1. Model solutions. *Quart. J. Roy. Meteorol. Soc.*, 122(533, A):1153–1174, 1996. ISSN 0035-9009. doi:10.1002/qj.49712253307.

F. Guest, M. Reeder, C. Marks, and D. Karoly. Inertia-gravity waves observed in the lower stratosphere over macquarie island. *J. Atmos. Sci.*, 57(5):737–752, 2000.

J. Hadamard. Sur les problèmes aux dérivées partielles et leur signification physique. *Princeton University Bull.*, pages 49–52, 1902.

A. Hertzog, G. Boccara, R. A. Vincent, F. Vial, and P. Cocquerez. Estimation of gravity wave momentum flux and phase speeds from quasi-Lagrangian stratospheric balloon flights. part ii: Results from the vorcore campaign in antarctica. *J. Atmos. Sci.*, 65(10):3056–3070, 2008. doi:10.1175/2008JAS2710.1.

A. Hertzog, M. J. Alexander, and R. Plougonven. On the intermittency of gravity wave momentum flux in the stratosphere. *J. Atmos. Sci.*, 69(11):3433–3448, 2012. ISSN 0022-4928. doi:10.1175/JAS-D-12-09.1.

L. Hoffmann. Schnelle Spurengasretrieval für das Satellitenexperiment Envisat MIPAS. Technical Report JUEL-4207, Forschungszentrum Jülich, Jülich, Germany, 2006. ISSN 0944-2952.

L. Hoffmann and M. J. Alexander. Retrieval of stratospheric temperatures from Atmospheric Infrared Sounder radiance measurements for gravity wave studies. *J. Geophys. Res.*, 114:D07105, 2009. doi:10.1029/2008JD011241.

L. Hoffmann, M. Kaufmann, R. Spang, R. Müller, J. J. Remedios, D. P. Moore, C. M. Volk, T. von Clarmann, and M. Riese. Envisat MIPAS measurements of CFC-11: retrieval, validation, and climatology. *Atmos. Chem. Phys.*, 8:3671–3688, 2008. doi:10.1016/j.asr.2005.03.112.

L. Hoffmann, X. Xue, and M. J. Alexander. A global view of stratospheric gravity wave hotspots located with Atmospheric Infrared Sounder observations. *J. Geophys. Res. Atmos.*, 118(2):416–434, 2013. ISSN 2169-897X. doi:10.1029/2012JD018658.

J. R. Holton. The role of gravity wave induced drag and diffusion on the momentum budget of the mesosphere. *J. Atmos. Sci.*, 39(4):791–799, 1982.

J. R. Holton. The influence of gravity wave breaking on the general circulation of the middle atmosphere. *J. Atmos. Sci.*, 40(10):2497–2507, 1983. doi:10.1175/1520-0469(1983)040<2497:TIOGWB>2.0.CO;2.

J. R. Holton. *An Introduction to Dynamic Meteorology*. Academic Press Limited, 1992. 3rd edition.

IDL. Interactive Data Language (IDL). `http://www.harrisgeospatial.com/SoftwareTechnology/IDL.aspx`.

J. H. Jiang, D. L. Wu, and S. D. Eckermann. Upper Atmosphere Research Satellite (UARS) MLS observations of mountain waves over the Andes. *J. Geophys. Res.*, 107(D20)):8273, 2002. doi:10.1029/2002JD002091.

S. Kalisch, P. Preusse, M. Ern, S. D. Eckermann, and M. Riese. Differences in gravity wave drag between realistic oblique and assumed vertical propagation. *J. Geophys. Res. Atmos.*, 119:10,081–10,099, 2014. ISSN 2169-8996. doi:10.1002/2014JD021779.

S. Kalisch, H. Y. Chun, M. Ern, P. Preusse, Q. T. Trinh, S. D. Eckermann, and M. Riese. Comparison of simulated and observed convective gravity waves. *J. Geophys. Res. Atmos.*, 121(22):13474–13492, 2016. ISSN 2169-897X. doi:10.1002/2016JD025235.

M. Kaufmann, J. Blank, T. Guggenmoser, J. Ungermann, A. Engel, M. Ern, F. Friedl-Vallon, D. Gerber, J. U. Grooß, G. Guenther,

M. Höpfner, A. Kleinert, E. Kretschmer, T. Latzko, G. Maucher, T. Neubert, H. Nordmeyer, H. Oelhaf, F. Olschewski, J. Orphal, P. Preusse, H. Schlager, H. Schneider, D. Schuettemeyer, F. Stroh, O. Suminska-Ebersoldt, B. Vogel, C. M. Volk, W. Woiwode, and M. Riese. Retrieval of three-dimensional small-scale structures in upper-tropospheric/lower-stratospheric composition as measured by GLORIA. *Atmos. Meas. Tech.*, 8(1):81–95, 2015. doi:10.5194/amt-8-81-2015.

S. Kaufmann. personal communication, 2018.

J. Kidston, A. A. Scaife, S. C. Hardiman, D. M. Mitchell, N. Butchart, M. P. Baldwin, and L. J. Gray. Stratospheric influence on tropospheric jet streams, storm tracks and surface weather. *Nature Geosci.*, 8:433–440, 2015. doi:10.1038/ngeo2424.

A. Kleinert, F. Friedl-Vallon, T. Guggenmoser, M. Höpfner, T. Neubert, R. Ribalda, M. K. Sha, J. Ungermann, J. Blank, A. Ebersoldt, E. Kretschmer, T. Latzko, H. Oelhaf, F. Olschewski, and P. Preusse. Level 0 to 1 processing of the imaging fourier transform spectrometer GLORIA: generation of radiometrically and spectrally calibrated spectra. *Atmos. Meas. Tech.*, 7(12):4167–4184, 2014. doi:10.5194/amt-7-4167-2014.

A. Kleinert, I. Krisch, J. Ungermann, A. Adibekyan, B. Gutschwager, and C. Monte. Characterization of blackbody inhomogeneity and its effect on the retrieval results of the gloria instrument. *Atmospheric Measurement Techniques*, 11(7):3871–3882, 2018. doi:10.5194/amt-11-3871-2018.

L. Krasauskas, J. Ungermann, S. Ensmann, I. Krisch, E. Kretschmer, P. Preusse, and M. Riese. Tomographic airborne limb sounder retrievals on irregular grid with second order regularisation. *Atmospheric Measurement Techniques Discussions*, 2018:1–27, 2018. doi:10.5194/amt-2018-199.

I. Krisch, P. Preusse, J. Ungermann, A. Dörnbrack, S. D. Eckermann, M. Ern, F. Friedl-Vallon, M. Kaufmann, H. Oelhaf, M. Rapp, C. Strube, and M. Riese. First tomographic observations of gravity waves by the infrared limb imager gloria. *Atmos. Chem. Phys.*, 17(24):14937–14953, 2017. doi:10.5194/acp-17-14937-2017.

I. Krisch, J. Ungermann, P. Preusse, E. Kretschmer, and M. Riese. Limited angle tomography of mesoscale gravity waves by the infrared limb-sounder gloria. *Atmos. Meas. Tech.*, 11(7):4327–4344, 2018. doi:10.5194/amt-11-4327-2018.

I. Krisch, M. Ern, L. Hoffmann, P. Preusse, C. Strube, J. Ungermann, W. Woiwode, and M. Riese. Superposition of gravity waves with different propagation characteristics observed by airborne and spaceborne infrared sounders. *Atmospheric Chemistry and Physics Discussions*, 2020:1–31, 2020. doi:10.5194/acp-2020-327.

T. P. Lane, M. J. Reeder, and T. L. Clark. Numerical modeling of gravity wave generation by deep tropical convection. *J. Atmos. Sci.*, 58(10):1249–1274, 2001. doi:10.1175/1520-0469(2001)058<1249:NMOGWG>2.0.CO;2.

C. I. Lehmann, Y.-H. Kim, P. Preusse, H.-Y. Chun, M. Ern, and S.-Y. Kim. Consistency between fourier transform and small-volume few-wave decomposition for spectral and spatial variability of gravity waves above a typhoon. *Atmos. Meas. Tech.*, 5(7):1637–1651, 2012. doi:10.5194/amt-5-1637-2012.

Y. Lin and F. Zhang. Tracking gravity waves in baroclinic jet-front systems. *J. Atmos. Sci.*, 65:2402–2415, 2008. doi:10.1175/2007JAS2482.1.

X. Lu, C. Chen, W. Huang, J. A. Smith, X. Chu, T. Yuan, P.-D. Pautet, M. J. Taylor, G. Jie, and C. Y. Cullens. A coordinated study of 1 h mesoscale gravity waves propagating from logan to boulder with crrl na doppler lidars and temperature mapper. *J. Geo-*

phys. Res. Atmos., 120(19):10,006–10,021, 2015. ISSN 2169-8996. doi:10.1002/2015JD023604. 2015JD023604.

Z. Luo and D. C. Fritts. Gravity-wave excitation by geostrophic adjustment of the jet stream. part ii: Three-dimensional forcing. *J. Atmos. Sci.*, 50(1):104–115, 1993. doi:10.1175/1520-0469(1993)050<0104:GWEBGA>2.0.CO;2.

C. J. Marks and S. D. Eckermann. A three-dimensional nonhydrostatic ray-tracing model for gravity waves: Formulation and preliminary results for the middle atmosphere. *J. Atmos. Sci.*, 52(11):1959–1984, 1995. doi:10.1175/1520-0469(1995)052<1959:ATDNRT>2.0.CO;2.

D. R. Marsh, M. J. Mills, D. E. Kinnison, J.-F. Lamarque, N. Calvo, and L. M. Polvani. Climate change from 1850 to 2005 simulated in cesm1(waccm). *Journal of Climate*, 26(19):7372–7391, 2013. doi:10.1175/JCLI-D-12-00558.1.

C. McLandress. On the importance of gravity waves in the middle atmosphere and their parameterization in general circulation models. *J. Atm. Sol.-Terr. Phys.*, 60:1357–1383, 1998. doi:10.1016/S1364-6826(98)00061-3.

C. McLandress, M. J. Alexander, and D. L. Wu. Microwave Limb Sounder observations of gravity waves in the stratosphere: A climatology and interpretation. *J. Geophys. Res.*, 105(D9):11947–11967, 2000.

C. McLandress, T. G. Shepherd, S. Polavarapu, and S. R. Beagley. Is Missing Orographic Gravity Wave Drag near 60 degrees S the Cause of the Stratospheric Zonal Wind Biases in Chemistry Climate Models? *J. Atmos. Sci.*, 69(3):802–818, 2012. ISSN 0022-4928. doi:10.1175/JAS-D-11-0159.1.

A. S. Medvedev and N. M. Gavrilov. The nonlinear mechanism of gravity wave generation by meteorological motions in the atmosphere. *J. Atm. Sol.-Terr. Phys.*, 57:1221–1231, 1995.

N. Metropolis and S. Ulam. The monte carlo method. *Journal of the American Statistical Association*, 44(247):335–341, 1949. ISSN 01621459. doi:10.2307/2280232.

C. I. Meyer, M. Ern, L. Hoffmann, Q. T. Trinh, and M. J. Alexander. Intercomparison of AIRS and HIRDLS stratospheric gravity wave observations. *Atmos. Meas. Tech.*, 11(1):215–232, 2018. ISSN 1867-1381. doi:10.5194/amt-11-215-2018.

C. J. Nappo. *An Introduction to Atmospheric Gravity Waves*. Academic Press, second edition, 2012. ISBN 978-0-12-385223-6.

F. Natterer. *The mathematics of computerized tomography*. Society for Industrial and Applied Mathematics, Philadelphia, PA, USA, 2001. ISBN 0-89871-493-1.

F. Olschewski, A. Ebersoldt, F. Friedl-Vallon, B. Gutschwager, J. Hollandt, A. Kleinert, C. Monte, C. Piesch, P. Preusse, C. Rolf, P. Steffens, and R. Koppmann. The in-flight blackbody calibration system for the GLORIA interferometer on board an airborne research platform. *Atmos. Meas. Tech.*, 6(11):3067–3082, 2013. ISSN 1867-1381. doi:10.5194/amt-6-3067-2013.

D. O'Sullivan and T. J. Dunkerton. Generation of inertia-gravity waves in a simulated life cycle of baroclinic instability. *J. Atmos. Sci.*, 52(21):3695–3716, 1995. ISSN 0022-4928. doi:10.1175/1520-0469(1995)052<3695:GOIWIA>2.0.CO;2.

M. L. V. Pitteway and C. O. Hines. The viscous damping of atmospheric gravity waves. *Canadian Journal of Physics*, 41(12):1935–1948, 1963. doi:10.1139/p63-194.

R. Plougonven, A. Hertzog, and L. Guez. Gravity waves over Antarctica and the Southern Ocean: consistent momentum fluxes in mesoscale simulations and stratospheric balloon observations. *Quart. J. Roy. Meteorol. Soc.*, 139(670, A):101–118, 2013. ISSN 0035-9009. doi:10.1002/qj.1965.

A. Podglajen, A. Hertzog, R. Plougonven, and B. Legras. Lagrangian temperature and vertical velocity fluctuations due to gravity waves in the lower stratosphere. *Geophys. Res. Lett.*, 43:3543–3553, 2016. doi:10.1002/2016GL068148.

M. Pramitha, M. Venkat Ratnam, A. Taori, B. V. Krishna Murthy, D. Pallamraju, and S. Vijaya Bhaskar Rao. Evidence for tropospheric wind shear excitation of high-phase-speed gravity waves reaching the mesosphere using the ray-tracing technique. *Atmos. Chem. Phys.*, 15:2709–2721, 2015. doi:10.5194/acp-15-2709-2015.

F. Press. Earth models obtained by monte carlo inversion. *Journal of Geophysical Research*, 73(16):5223–5234, 1968. ISSN 2156-2202. doi:10.1029/JB073i016p05223.

P. Preusse, G. Eidmann, S. D. Eckermann, B. Schaeler, R. Spang, and D. Offermann. Indications of convectively generated gravity waves in CRISTA temperatures. *Adv. Space Res.*, 27(10):1653–1658, 2001.

P. Preusse, A. Dörnbrack, S. D. Eckermann, M. Riese, B. Schaeler, J. T. Bacmeister, D. Broutman, and K. U. Grossmann. Space-based measurements of stratospheric mountain waves by CRISTA, 1. sensitivity, analysis method, and a case study. *J. Geophys. Res.*, 107(D23)(8178), 2002. doi:10.1029/2001JD000699.

P. Preusse, S. D. Eckermann, M. Ern, J. Oberheide, R. H. Picard, R. G. Roble, M. Riese, J. M. Russell III, and M. G. Mlynczak. Global ray tracing simulations of the SABER gravity wave climatology. *J. Geophys. Res. Atmos.*, 114, 2009a. doi:10.1029/2008JD011214.

P. Preusse, S. Schroeder, L. Hoffmann, M. Ern, F. Friedl-Vallon, J. Ungermann, H. Oelhaf, H. Fischer, and M. Riese. New perspectives on gravity wave remote sensing by spaceborne infrared limb imaging. *Atmos. Meas. Tech.*, 2(1):299–311, 2009b. doi:10.5194/amt-2-299-2009.

P. Preusse, M. Ern, P. Bechtold, S. D. Eckermann, S. Kalisch, Q. T. Trinh, , and M. Riese. Characteristics of gravity waves resolved by ecmwf.

Atmos. Chem. Phys., 14(19):10483–10508, 2014. doi:10.5194/acp-14-10483-2014.

Python. Python software foundation. `http://www.python.org`, 2018. Python language reference, version 3.6, last access: 10 August 2018.

M. Rautenhaus, G. Bauer, and A. Dörnbrack. A web service based tool to plan atmospheric research flights. *Geosci. Model Dev.*, 5(1):55–71, 2012. doi:10.5194/gmd-5-55-2012.

M. Reeder and M. Griffiths. Stratospheric inertia-gravity waves generated in a numerical model of frontogenesis .2. Wave sources, generation mechanisms and momentum fluxes. *Quart. J. Roy. Meteorol. Soc.*, 122(533, A):1175–1195, 1996. ISSN 0035-9009. doi:10.1002/qj.49712253308.

J. J. Remedios, R. J. Leigh, A. M. Waterfall, D. P. Moore, H. Sembhi, I. Parkes, J. Greenhough, M. Chipperfield, and D. Hauglustaine. MIPAS reference atmospheres and comparisons to V4.61/V4.62 MIPAS level 2 geophysical data sets. *Atmos. Chem. Phys. Discuss.*, 7(4):9973–10017, 2007. doi:10.5194/acpd-7-9973-2007.

H. E. Revercomb, H. Buijs, H. B. Howell, D. D. LaPorte, W. L. Smith, and L. A. Sromovsky. Radiometric calibration of ir fourier transform spectrometers: solution to a problem with the high-resolution interferometer sounder. *Appl. Optics*, 27(15):3210–3218, 1988. doi:10.1364/AO.27.003210.

B. Ribstein and U. Achatz. The interaction between gravity waves and solar tides in a linear tidal model with a 4-d ray-tracing gravity-wave parameterization. *Journal of Geophysical Research: Space Physics*, 121(9):8936–8950, 2016. ISSN 2169-9402. doi:10.1002/2016JA022478. 2016JA022478.

J. H. Richter, F. Sassi, and R. R. Garcia. Toward a physically based gravity wave source parameterization in a general circulation model. *J. Atmos. Sci.*, 67:136–156, 2010.

M. Riese. *Das CRISTA-Meßsystem: Struktur und Anwendungen*. Dissertation, Universität Wuppertal, 1994.

M. Riese, P. Preusse, R. Spang, M. Ern, M. Jarisch, K.-U. Grossmann, and D. Offermann. Measurements of trace gases by the Cryogenic Infrared Spectrometers and Telescopes for the Atmosphere (CRISTA) experiment. *Adv. Space Res.*, 19:563–566, 1997. doi:10.1016/S0273-1177(97)00172-5.

M. Riese, R. Spang, P. Preusse, M. Ern, M. Jarisch, D. Offermann, and K. U. Grossmann. Cryogenic infrared spectrometers and telescopes for the atmosphere (CRISTA) data processing and atmospheric temperature and trace gas retrieval. *J. Geophys. Res.*, 104:349–367, 1999.

M. Riese, H. Oelhaf, P. Preusse, J. Blank, M. Ern, F. Friedl-Vallon, H. Fischer, T. Guggenmoser, M. Hoepfner, P. Hoor, M. Kaufmann, J. Orphal, F. Ploeger, R. Spang, O. Suminska-Ebersoldt, J. Ungermann, B. Vogel, and W. Woiwode. Gimballed Limb Observer for Radiance Imaging of the Atmosphere (GLORIA) scientific objectives. *Atmos. Meas. Tech.*, 7 (7):1915–1928, 2014. ISSN 1867-1381. doi:10.5194/amt-7-1915-2014.

C. D. Rodgers. *Inverse Methods for Atmospheric Sounding: Theory and Practice*, volume 2 of *Series on Atmospheric, Oceanic and Planetary Physics*. World Scientific, Singapore, 2000.

L. Rothman, I. Gordon, Y. Babikov, A. Barbe, D. C. Benner, P. Bernath, M. Birk, L. Bizzocchi, V. Boudon, L. Brown, A. Campargue, K. Chance, E. Cohen, L. Coudert, V. Devi, B. Drouin, A. Fayt, J.-M. Flaud, R. Gamache, J. Harrison, J.-M. Hartmann, C. Hill, J. Hodges, D. Jacquemart, A. Jolly, J. Lamouroux, R. L. Roy, G. Li, D. Long, O. Lyulin, C. Mackie, S. Massie, S. Mikhailenko, H. Müller, O. Naumenko, A. Nikitin, J. Orphal, V. Perevalov, A. Perrin, E. Polovtseva, C. Richard, M. Smith, E. Starikova, K. Sung, S. Tashkun, J. Tennyson, G. Toon, V. Tyuterev, and G. Wagner. The HITRAN2012 molecular spectroscopic database. *J. Quant. Spectrosc. Radiat. Transfer*, 130(0):

4 – 50, 2013. ISSN 0022-4073. doi:10.1016/j.jqsrt.2013.07.002. HITRAN2012 special issue.

M. L. Salby and R. R. Garcia. Transient response to localized episodic heating in the tropics. Part I: Excitation and short-time near-field behavior. *J. Atmos. Sci.*, 44(2):458–498, 1987.

I. Sandu, P. Bechtold, A. Beljaars, A. Bozzo, F. Pithan, T. G. Shepherd, and A. Zadra. Impacts of parameterized orographic drag on the northern hemisphere winter circulation. *J. Adv. Model. Earth Syst.*, 8(1):196–211, 2016. ISSN 1942-2466. doi:10.1002/2015MS000564.

K. Sato, H. Hashiguchi, and S. Fukao. Gravity waves and turbulence associated with cumulus convection observed with the UHF/VHF clear-air Doppler radars. *J. Geophys. Res.*, 100(D4):7111–7119, 1995.

K. Sato, S. Watanabe, Y. Kawatani, Y. Tomikawa, K. Miyazaki, and M. Takahashi. On the origins of mesospheric gravity waves. *Geophys. Res. Lett.*, 36, 2009. ISSN 0094-8276. doi:10.1029/2009GL039908.

A. Savitzky and M. J. E. Golay. Smoothing and differentiation of data by simplified least squares procedures. *Analytical Chemistry*, 36(8): 1627–1639, 1964. doi:10.1021/ac60214a047.

A. A. Scaife, A. Y. Karpechko, M. P. Baldwin, A. Brookshaw, A. H. Butler, R. Eade, M. Gordon, C. MacLachlan, N. Martin, N. Dunstone, and D. Smith. Seasonal winter forecasts and the stratosphere. *Atmospheric Science Letters*, 17(1):51–56, 2016. ISSN 1530-261X. doi:10.1002/asl.598.

T. Schmidt, J. P. Cammas, H. G. J. Smit, S. Heise, J. Wickert, and A. Haser. Observational characteristics of the tropopause inversion layer derived from CHAMP/GRACE radio occultations and MOZAIC aircraft data. *J. Geophys. Res.*, 115, 2010. ISSN 2169-897X. doi:10.1029/2010JD014284.

J. F. Scinocca and T. G. Shepherd. Nonlinear wave-activity conservation laws and hamiltonian structure for the two-dimensional anelastic equations. *Journal of the Atmospheric Sciences*, 49(1):5–28, 1992. doi:10.1175/1520-0469(1992)049<0005:NWACLA>2.0.CO;2.

R. D. Sharman, S. B. Trier, T. P. Lane, and J. D. Doyle. Sources and dynamics of turbulence in the upper troposphere and lower stratosphere: A review. *Geophysical Research Letters*, 39(12), 2012. doi:10.1029/2012GL051996.

T. G. Shepherd. Atmospheric circulation as a source of uncertainty in climate change projections. *Nature Geosci.*, 7(10):703–708, 2014. ISSN 1752-0894. doi:10.1038/NGEO2253.

M. Sigmond and J. F. Scinocca. The influence of the basic state on the northern hemisphere circulation response to climate change. *Journal of Climate*, 23(6):1434–1446, 2010. doi:10.1175/2009JCLI3167.1.

D. E. Siskind. Simulations of the winter stratopause and summer mesopause at varying spatial resolutions. *J. Geophys. Res. Atmos.*, 119 (2):461–470, 2014. ISSN 2169-897X. doi:10.1002/2013JD020985.

W. C. Skamarock. Evaluating mesoscale NWP models using kinetic energy spectra. *Mon. Weath. Rev.*, 132:3019–3032, 2004.

R. B. Smith, A. D. Nugent, C. G. Kruse, D. C. Fritts, J. D. Doyle, S. D. Eckermann, M. J. Taylor, A. Doernbrack, M. Uddstrom, W. Cooper, P. Romashkin, J. Jensen, and S. Beaton. Stratospheric Gravity Wave Fluxes and Scales during DEEPWAVE. *J. Atmos. Sci.*, 73(7):2851–2869, 2016. ISSN 0022-4928. doi:10.1175/JAS-D-15-0324.1.

C. Snyder, D. J. Muraki, R. Plougonven, and F. Zhang. Inertia-gravity waves generated within a dipole vortex. *Journal of the Atmospheric Sciences*, 64(12):4417–4431, 2007. doi:10.1175/2007JAS2351.1.

C. Snyder, R. Plougonven, and D. J. Muraki. Mechanisms for spontaneous gravity wave generation within a dipole vortex.

Journal of the Atmospheric Sciences, 66(11):3464–3478, 2009. doi:10.1175/2009JAS3147.1.

S. Solomon, K. H. Rosenlof, R. W. Portmann, J. S. Daniel, S. M. Davis, T. J. Sanford, and G.-K. Plattner. Contributions of stratospheric water vapor to decadal changes in the rate of global warming. *Science*, 327: 1219–1223, 2010. doi:10.1126/science.1182488.

I.-S. Song and H.-Y. Chun. A Lagrangian spectral parameterization of gravity wave drag induced by cumulus convection. *J. Atmos. Sci.*, 65: 1204–1224, 2008.

G. Stober, S. Sommer, M. Rapp, and R. Latteck. Investigation of gravity waves using horizontally resolved radial velocity measurements. *Atmos. Meas. Tech.*, 6(10):2893–2905, 2013. doi:10.5194/amt-6-2893-2013.

B. R. Sutherland. *Internal Gravity Waves*. Cambridge University Press, 2010.

A. Tarantola. *Inverse Problem Theory*. Society for Industrial and Applied Mathematics, Philadelphia, 2004.

A. N. Tikhonov and V. Y. Arsenin. *Solutions of ill-posed problems*. Winston, Washington D.C., USA, 1977.

Q. T. Trinh, S. Kalisch, P. Preusse, H.-Y. Chun, S. D. Eckermann, M. Ern, and M. Riese. A comprehensive observational filter for satellite infrared limb sounding of gravity waves. *Atmos. Meas. Tech.*, 8:1491–1517, 2015. doi:10.5194/amt-8-1491-2015.

Q. T. Trinh, S. Kalisch, P. Preusse, M. Ern, H.-Y. Chun, S. D. Eckermann, M.-J. Kang, and M. Riese. Tuning of a convective gravity wave source scheme based on hirdls observations. *Atmos. Chem. Phys.*, 16:7335–7356, 2016. doi:10.5194/acp-16-7335-2016.

J. Ungermann, L. Hoffmann, P. Preusse, M. Kaufmann, and M. Riese. Tomographic retrieval approach for mesoscale gravity wave observations by the PREMIER infrared limb-sounder. *Atmos. Meas. Tech.*, 3 (2):339–354, 2010a. doi:10.5194/amt-3-339-2010.

J. Ungermann, M. Kaufmann, L. Hoffmann, P. Preusse, H. Oelhaf, F. Friedl-Vallon, and M. Riese. Towards a 3-D tomographic retrieval for the air-borne limb-imager GLORIA. *Atmos. Meas. Tech.*, 3(6):1647–1665, 2010b. doi:10.5194/amt-3-1647-2010.

J. Ungermann, J. Blank, J. Lotz, K. Leppkes, L. Hoffmann, T. Guggenmoser, M. Kaufmann, P. Preusse, U. Naumann, and M. Riese. A 3-D tomographic retrieval approach with advection compensation for the air-borne limb-imager GLORIA. *Atmos. Meas. Tech.*, 4(11):2509–2529, 2011. doi:10.5194/amt-4-2509-2011.

J. Ungermann, C. Kalicinsky, F. Olschewski, P. Knieling, L. Hoffmann, J. Blank, W. Woiwode, H. Oelhaf, E. Hösen, C. M. Volk, A. Ulanovsky, F. Ravegnani, K. Weigel, F. Stroh, and M. Riese. CRISTA-NF measurements with unprecedented vertical resolution during the RECONCILE aircraft campaign. *Atmos. Meas. Tech.*, 5(5):1173–1191, 2012. doi:10.5194/amt-5-1173-2012.

J. Ungermann, J. Blank, M. Dick, A. Ebersoldt, F. Friedl-Vallon, A. Giez, T. Guggenmoser, M. Höpfner, T. Jurkat, M. Kaufmann, S. Kaufmann, A. Kleinert, M. Krämer, T. Latzko, H. Oelhaf, F. Olchewski, P. Preusse, C. Rolf, J. Schillings, O. Suminska-Ebersoldt, V. Tan, N. Thomas, C. Voigt, A. Zahn, M. Zöger, and M. Riese. Level 2 processing for the imaging fourier transform spectrometer gloria: derivation and validation of temperature and trace gas volume mixing ratios from calibrated dynamics mode spectra. *Atmos. Meas. Tech.*, 8(6):2473–2489, 2015. doi:10.5194/amt-8-2473-2015.

S. L. Vadas and D. C. Fritts. Gravity wave radiation and mean responses to local body forces in the atmosphere. *J. Atmos. Sci.*, 58(16):2249–2279, 2001. doi:10.1175/1520-0469(2001)058<2249:GWRAMR>2.0.CO;2.

S. L. Vadas, J. Zhao, X. Chu, and E. Becker. The excitation of secondary gravity waves from body forces: Theory and observation. *Journal of Geophysical Research: Atmospheres*, 0(ja), 2018. doi:10.1029/2017JD027970.

A. Viudez. The stationary frontal wave packet spontaneously generated in mesoscale dipoles. *Journal of Physical Oceanography*, 38(1):243–256, 2008. doi:10.1175/2006JPO3692.1.

T. von Clarmann, C. De Clercq, M. Ridolfi, M. Höpfner, and J.-C. Lambert. The horizontal resolution of MIPAS. *Atmos. Meas. Tech.*, 2:47–54, 2009. doi:10.5194/amt-2-47-2009.

J. Wagner, A. Doernbrack, M. Rapp, S. Gisinger, B. Ehard, M. Bramberger, B. Witschas, F. Chouza, S. Rahm, C. Mallaun, G. Baumgarten, and P. Hoor. Observed versus simulated mountain waves over scandinavia-improvement of vertical winds, energy and momentum fluxes by enhanced model resolution? *Atmos. Chem. Phys.*, 17(6): 4031–4052, 2017. ISSN 1680-7316. doi:10.5194/acp-17-4031-2017.

L. Wang and M. A. Geller. Morphology of gravity-wave energy as observed from 4 years (1998-2001) of high vertical resolution U.S. radiosonde data. *J. Geophys. Res.*, 108(D16), 2003. doi:10.1029/2002JD002786.

S. Wang and F. Zhang. Sensitivity of mesoscale gravity waves to the baroclinicity of jet-front systems. *Monthly Weather Review*, 135(2): 670–688, 2007. doi:10.1175/MWR3314.1.

S. Wang and F. Zhang. Source of gravity waves within a vortex-dipole jet revealed by a linear model. *Journal of the Atmospheric Sciences*, 67 (5):1438–1455, 2010. doi:10.1175/2010JAS3327.1.

S. Wang, F. Zhang, and C. C. Epifanio. Forced gravity wave response near the jet exit region in a linear model. *Quarterly Journal of the Royal Meteorological Society*, 136(652):1773–1787, 2010. doi:10.1002/qj.676.

K. Weigel, M. Riese, L. Hoffmann, S. Hoefer, C. Kalicinsky, P. Knieling, F. Olschewski, P. Preusse, F. Stroh, R. Spang, and C. M. Volk. CRISTA-NF measurements during the AMMA-SCOUT-O_3 aircraft campaign. *Atmos. Meas. Tech.*, 3(2):1437–1455, 2010. doi:10.5194/amt-3-1437-2010.

M. P. Weinreb and A. C. Neuendorffer. Method to apply homogeneous-path transmittance models to inhomogeneous atmospheres. *J. Atmos. Sci.*, 30:662–666, 1973. doi:10.1175/1520-0469(1973)030<0662:MTAHPT>2.0.CO;2.

WMO. Scientific assessment of ozone depletion: 2014, global ozone research and monitoring project - report no. 55. Geneva, Switzerland, 2014.

C. M. Wrasse, T. Nakamura, H. Takahashi, A. F. Medeiros, M. J. Taylor, D. Gobbi, C. M. Denardini, J. Fechine, R. A. Buriti, A. Salatun, Suratno, E. Achmad, and A. G. Admiranto. Mesospheric gravity waves observed near equatorial and low-middle latitude stations: wave characteristics and reverse ray tracing results. *Ann. Geophys.*, 24:3229–3240, 2006.

C. J. Wright, N. P. Hindley, L. Hoffmann, M. J. Alexander, and N. J. Mitchell. Exploring gravity wave characteristics in 3-d using a novel s-transform technique: Airs/aqua measurements over the southern andes and drake passage. *Atmos. Chem. Phys.*, 17(13):8553–8575, 2017. doi:10.5194/acp-17-8553-2017.

D. L. Wu and J. W. Waters. Gravity-wave-scale temperature fluctuations seen by the UARS MLS. *Geophys. Res. Lett.*, 23(23):3289–3292, 1996.

X. Xu, Y. Wang, M. Xue, and K. Zhu. Impacts of horizontal propagation of orographic gravity waves on the wave drag in the stratosphere and lower mesosphere. *J. Geophys. Res. Atmos.*, 2017. ISSN 2169-8996. doi:10.1002/2017JD027528. 2017JD027528.

S. D. Zhang, C. M. Huang, K. M. Huang, F. Yi, Y. H. Zhang, Y. Gong, and Q. Gan. Spatial and seasonal variability of medium- and high-

frequency gravity waves in the lower atmosphere revealed by us radiosonde data. *Ann. Geophys.*, 32(9):1129–1143, 2014. ISSN 0992-7689. doi:10.5194/angeo-32-1129-2014.

X. Zhu. A new theory of the saturated gravity wave spectrum for the middle atmosphere. *J. Atmos. Sci.*, 51(24):3615–3626, 1994. doi:10.1175/1520-0469(1994)051<3615:ANTOTS>2.0.CO;2.

X. Zhu and J. R. Holton. Mean fields induced by local gravity-wave forcing in the middle atmosphere. *J. Atmos. Sci.*, 44:620–630, 1987.

Danksagung

Als erstes möchte ich mich sehr herzlich bei meinem Doktorvater Prof. Martin Riese und meinen zwei Betreuern Peter Preuße und Jörn Ungermann bedanken, dass sie mir die Gelegenheit zu dieser Doktorarbeit gegeben haben. Danke dass ihr immer eine offene Tür für mich hattet und mir all die Jahre immer mit Rat und Tat zur Seite gestanden habt.

Ein riesen Dank geht auch an das GLORIA Team. Ohne euch hätte es diese Doktorarbeit in ihrer jetzigen Form nicht gegeben und vor allem hätten die letzten vier Jahre nur halb so viel Spaß gemacht. Besonders habe ich den starken Zusammenhalt innerhalb des Teams und das Engagement jedes einzelnen besonders zur Kampagnenzeit sehr zu schätzen gelernt.

Danke an Herman Oelhaf, Björn-Martin Sinnhuber und Wolfgang Woiwode vom KIT für die ausgezeichnet Organisation der Messkampagne und an Markus Rapp und Andreas Dörnbrack vom DLR für die anregenden wissenschaftlichen Diskussionen.

Das HITEC Doktorandenprogramm hat mit seiner Finanzierung diese Arbeit erst möglich gemacht und mir mit Professor Kaoru Sato als externe Mentorin eine herausragende Wissenschaftlerin zur Seite gestellt. Thank you very much Kaoru for your time and dedication during my visits in Tokio.

Vielen, vielen Dank an alle aktuellen und ehemaligen Mitarbeiter des IEK-7, die immer für ein nettes Gespräch zu haben waren, egal ob es um die Wissenschaft oder Gott und die Welt ging. Ihr seid echt eine tolle Truppe und ich werde die Kaffeepausen, Wanderausflüge und Skifreizeiten mit euch sehr vermissen!

Und nicht zu vergessen: meine Familie und David. Danke, dass ihr mich immer nach Kräften unterstützt habt und nie aufgehört habt an mich zu glauben.

Band / Volume 482
Studies of oxidation resistant tungsten alloys at temperatures of 1100K to 1475K
F. Klein (2019), 158 pp
ISBN: 978-3-95806-444-7

Band / Volume 483
Impact Assessment of Land-Use Change and Agricultural Treatments on Greenhouse Gas Emissions from Wetlands of Uganda and Tanzania
K. X. X. Wagner (2019), 144 pp
ISBN: 978-3-95806-447-8

Band / Volume 484
IEK-3 Report 2019
Tailor-Made Energy Conversion for Sustainable Fuels
D. Stolten, B. Emonts (Eds.) (2020), 162 pp
ISBN: 978-3-95806-451-5

Band / Volume 485
Multiskalare Modellierung integrierter Energie- und Elektrizitätssysteme
T. C. Pesch (2019), XXV, 384 pp
ISBN: 978-3-95806-452-2

Band / Volume 486
Quantitative Untersuchung des Laserablationsprozesses mittels Kombination von optischer Spektroskopie und Massenspektrometrie
J. Oelmann (2020), vii, 141 pp
ISBN: 978-3-95806-453-9

Band / Volume 487
Leistungssteigerung metallgestützter Festelektrolyt-Brennstoffzellen (MSCs) durch gezielte Optimierungen des Anoden/Elektrolytverbunds
C. Bischof (2020), X, 176 pp
ISBN: 978-3-95806-455-3

Band / Volume 488
Aluminiumoxiddispersionsverstärkte Haftvermittlermaterialien in Wärmedämmschichtsystemen
C. Vorkötter (2020), VIII, 99, XXXIII pp
ISBN: 978-3-95806-457-7

Band / Volume 489
The Balmer lines emission of fast hydrogen atoms at the plasma-solid interface in a low density plasma: challenges and applications
S. O. Dickheuer (2020), 117 pp
ISBN: 978-3-95806-458-4

Band / Volume 490
Micromechanical Characterization of Ceramic Solid Electrolytes for Electrochemical Storage Devices
J. F. Nonemacher (2020), xv, 131 pp
ISBN: 978-3-95806-461-4

Band / Volume 491
Nanoscale investigation of high temperature oxidation mechanisms of high-Cr ferritic steels
A. Vayyala (2020), xix, 105 pp
ISBN: 978-3-95806-467-6

Band / Volume 492
Electrolyte development for a SOFC operating at low temperature
J. Zhang (2020), vi, 121 pp
ISBN: 978-3-95806-471-3

Band / Volume 493
Modeling and Simulation of Polymer Electrolyte Fuel Cells
S. Zhang (2020), 4, xii, 214 pp
ISBN: 978-3-95806-472-0

Band / Volume 494
Ab initio perspective on hydrogenated amorphous silicon for thin-film and heterojunction photovoltaics
P. Czaja (2020), 107 pp
ISBN: 978-3-95806-474-4

Band / Volume 495
Measurements of Atmospheric OH and HO_2 Radicals by Laser-Induced Fluorescence on the HALO Aircraft during the OMO-ASIA 2015 Campaign
C. Künstler (2020), 156 pp
ISBN: 978-3-95806-477-5

Band / Volume 496
Tomographic observations of gravity waves with the infrared limb imager GLORIA
I. Krisch (2020), vii, 187 pp
ISBN: 978-3-95806-481-2

Energie & Umwelt / Energy & Environment
Band / Volume 496
ISBN 978-3-95806-481-2

Mitglied der Helmholtz-Gemeinschaft

JÜLICH
Forschungszentrum